BUBBLE FORMATION AND BUBBLE-WALL INTERACTION AT A SUBMERGED ORIFICE

XIAO ZONGYUAN

NATIONAL UNIVERSITY OF SINGAPORE

2004

BUBBLE FORMATION AND BUBBLE-WALL INTERACTION AT A SUBMERGED ORIFICE

XIAO ZONGYUAN
(*B. Eng., ZJU*)

A THESIS SUBMITTED
FOR THE DEGREE OF DOCTOR OF PHILOSOPHY
DEPARTMENT OF CHEMICAL AND BIOMOLECULAR ENGINEERING
NATIONAL UNIVERSITY OF SINGAPORE
2004

ACKNOWLEDGEMENTS

I would like to express my sincere gratitude to my supervisor, Prof. Reginald B. H. Tan, for his invaluable guidance and advice, remarkable encouragement, great patience and understanding, and continuous support throughout this project without whom the work will not be achieved.

My appreciation also goes to committee members: Prof. P. R. Krishnaswamy and Dr. M. Favelukis for their advice, interest and valuable time. Particular thanks go to Dr. Wang Chi-Hwa for providing some facilities, Mr. Ng Kim Poi for the help in constructing the experimental apparatus, colleagues, particularly Dr. Chen Weibin, Dr. Zhang Wenxing, Ms. Xie Shuyi and Ms. Zhang Yali for their supportive comments and cheerful assistance.

I am extremely grateful to my beloved family members for their love and support throughout the time of the PhD course. The thesis is dedicated to them.

Finally, I would also like to thank National University of Singapore for granting me research scholarship.

TABLE OF CONTENTS

SUMMARY

To increase the heat or mass transfer across an interface by increasing the interfacial area, gas dispersion through submerged orifices is an efficient and commonly used method in a wide range of process equipment. To date, numerous theoretical and experimental studies have been reported in the field of bubble formation at a submerged orifice and many models have been developed to clarify the effects of various factors on bubble formation. However, the effects of the boundaries around the bubble formation system were not taken into account in most of these studies. It has generally been assumed that the bubble column is very large compared with the orifice size and the wall effect could be neglected. In this study, the wall effect on bubble formation was investigated experimentally and theoretically.

Since the flow field around the bubble is assumed to be irrotational and the viscosity of the liquid is negligible, a fundamental non-spherical model was developed by means of the boundary integral method to predict the bubble formation process. This model was validated through the comparison of the theoretical predictions with the experimental results from the literature reported.

To study the wall effect experimentally, three sizes of bubble column with diameters, $I.D.\phi$ 30mm×470mm, $I.D.\phi$ 50mm×470mm and $I.D.\phi$ 100mm×470mm, were designed. High-speed video images and high sensitive dynamic pressure transducer were applied to visualize bubble formation process and record the instantaneous pressure fluctuation in the gas chamber respectively. Bubbling frequency was obtained from the time-pressure signals via Fast Fourier Transform (FFT). It was observed that there are three distinct bubbling regimes, single bubbling, pairing and multiple

bubbling, and as the ratio of the column diameter to orifice diameter decreases, the bubbling regimes generally transition from single bubbling to pairing and eventually multiple bubbling, with a corresponding decrease in bubbling frequency. Pairing and multiple bubbling are more likely to occur with large chamber volumes and high gas flow rates.

To study the wall effect theoretically, a specific system of images was introduced into the fundamental non-spherical model to satisfy the no-flux boundary condition on the impermeable column wall. Comparison of experimental results for bubbling frequency with the theoretical predictions shows that the agreement is good, i.e. the model successfully predicts the effect of the column wall on bubbling frequency. To thoroughly understand the underlying mechanism and take into account the bubble-bubble interaction as well as the bubble-wall interaction, a further spherical model was developed using potential flow theory. It was observed that this model can predict the bubble formation process very well and it also can predict the occurrence of pairing and multiple bubbling.

NOMENCLATURE

Symbol	**Description**	**Unit**
a	bubble radius	m
a_{sc}	radius of spherical-cap bubble	m
b	thickness of the plate	m
c_o	sound speed in the gas	m/s
C_D	drag coefficient	-
C_g	constant in Eq. (6.2)	-
d_c	diameter of the bubble column	m
d_o	diameter of the orifice	m
E_b	internal energy within the bubble	J
E_c	internal energy within the chamber	J
D_m	maximum horizontal diameter of the bubble	m
f	bubble frequency	s^{-1}
f'	fanning friction factor	-
Fr	Froude number	-
g	acceleration due to gravity	m/s^2
H	height of liquid above the orifice	m
k	orifice coefficient in Eqs. (3.69)	-
k_o	orifice coefficient in Eq. (6.2)	-
m	mass	kg
$\overline{m}$	added mass	kg
n	outward normal	-
N_c	capacitance number, $N_c = \dfrac{4g(\rho_l - \rho_g)V_c}{\pi d_o^2 \rho_g c_o^{\,2}}$	-
$N_c^{'}$	capacitance number, $N_c^{'} = \dfrac{4\rho_l g V_c}{\pi d_o^2 P_s}$	-
N_{Re}	Reynold number of detached rising bubble $(= 2a_{sc}U_T\rho_l / \mu_l)$	-
O_n	Orifice number	-
P_a	gas pressure inlet to the chamber	Pa

P_b	bubble pressure	Pa
P_c	chamber pressure	Pa
P_{cDET}	chamber pressure at bubble detachment	Pa
P_l	liquid pressure	Pa
$\overline{P}_l$	average liquid pressure at bubble boundary	Pa
P_{or}	liquid pressure at the orifice	Pa
P_{so}	static pressure at the orifice	Pa
P_{st}	hydrostatic pressure at coordinate (r,θ)	Pa
P_w	wake pressure	Pa
P_{wb}	wake pressure at the bubble surface	Pa
P_{wo}	wake pressure at the orifice	Pa
P_∞	system pressure above the bulk liquid	Pa
q	gas flow rate through the orifice	m^3/s
Q	gas flow rate into the chamber	m^3/s
ΔQ	heat added	J/s
r	radial coordinate	m
r_c	radius of the bubble column	m
r_o	radius of the orifice	m
R_1	principal radius of curvature on vertical plane	m
R_2	principal radius of curvature on horizontal plane	m
R_g	gas constant	J/(mol·K)
Re_o	orifice Reynolds number, $\mathrm{Re}_o = \dfrac{2\rho_g r_o u_o}{\mu_g}$ in Eq. (6.2)	-
s	tangential direction (in Chapter 3)	-
s	perpendicular distance between bubble center and orifice (in Chapter 6)	m
s_{bb}	mean distance between rising and growing bubble	m
s_{bo}	distance between rising bubble and orifice	m
t	time	s
t_f	bubble formation time	s
t_w	waiting time	s
T	time during waiting	s
u	velocity field of the liquid	m/s
u_o	instantaneous gas velocity through the orifice in Eq. (6.2)	m/s

U	bubble vertical rising velocity	m/s
U_i	initial normal of the bubble	m/s
U_T	terminal rising velocity of spherical-cap bubble	m/s
V_b	bubble volume	m^3
V_c	chamber volume	m^3
V_n	Volume number	-
ΔW	work done externally	J/s
We	Weber number	-
z	axial coordinate	m

Greek symbols

Symbol	**Description**	**Unit**
γ	adiabatic exponent	-
Γ	circulation about the vortex	-
θ	angular coordinate	rad
θ_c	contact angle in Eq. (3.84)	rad
θ'	angle in Eq. (6.11)	rad
κ	curvature of the bubble surface	m^{-1}
μ_g	gas viscosity	Kg/(m·s)
μ_l	liquid viscosity	Kg/(m·s)
ξ	parameter used to defined the bubble surface	-
ρ_b	density of vapor inside bubble	kg/m^3
ρ_g	gas density	kg/m^3
ρ_l	liquid density	kg/m^3
σ	surface tension	N/m
τ	dimensionless time	-
ϕ	velocity potential	m^2/s
ϕ_p	velocity potential for expanding bubble	m^2/s
ϕ_T	velocity potential for translating bubble	m^2/s
ψ	normal derivative of velocity potential	m/s

LIST OF FIGURES

LIST OF TABLES

Chapter 1 Introduction

1.1 Background

Operations involving mass or heat transfer across an interface are very common in the chemical industry. To obtain rapid transfer rate in equipment of finite size, a large interfacial area per unit volume is preferred in such operations. There are three common methods used to satisfy this requirement, which include film method, rupture of bulk fluid and gas dispersion through submerged orifices. Among them, gas dispersion through submerged orifices, which permits equipment of extremely simple design and leads to reasonably large interfacial areas, is the most efficient and most commonly used one in process equipment such as distillation columns, absorption towers, flotation cells, bubble columns, air-lift vessels, aerated stirred tanks, biological wastewater treatment systems and metallurgical smelters. Thus the formation of bubbles, the first stage in gas dispersion, becomes an important aspect to study the process of dispersion.

Bubbles are formed by the flow of gas through orifices submerged in a liquid. In the design or operation of gas-liquid contacting equipment, it is essential to clarify the factors affecting bubble formation and to understand the underlying mechanisms, so that the coalescence and breakdown of bubbles are not serious. Although practical applications usually involve the simultaneous participation of many bubbles, most experimental and theoretical studies of bubble formation have been concerned with a single bubble. The reason is that the multiple bubbles studies are very complicated, and it has been generally difficult to draw definite conclusions from such studies. Thence bubble formation at a single orifice, the simplest one, is usually studied by most of the researchers because it excludes mutual influence of bubbles formed in neighboring orifices. Although the effect of adjacent orifices is neglected, the study of bubble formation at a single orifice yields statistical information concerning the factors and also gives insight into the dynamics of the process. The understanding of the underlying mechanisms of this condition will contribute to studies on the mechanism with many orifices.

Over the past decades, numerous theoretical and experimental studies have been reported in the field of bubble formation. However, for most of the previous studies, there are some assumptions that the size of the bubble column is greatly larger than the orifice. Thus, the whole domain for bubble formation under consideration is seen as an infinite system and the wall effect of the bubble column could be neglected. This is true when the column diameter is very large compared with the orifice diameter. However, it is observed that the bubble behavior is modified as the column becomes smaller. Although much work has been done up to date on bubble formation, there is no comprehensive model which includes the effects of boundary factors, such as orifice plate and wall of the bubble column.

1.2 Objective of present study

The principal objectives of the present study were to:

1. Develop a fundamental non-spherical model to predict bubble formation at a submerged orifice with the boundary integral method.

2. Investigate the effect of the bubble column wall on bubble formation experimentally and theoretically. Based on the fundamental non-spherical model, the wall effect is investigated theoretically with an introduction of a specific image system.
3. Develop a spherical model using potential flow theory, which takes into account the bubble-bubble and bubble-wall interactions in bubble formation.

This study may lead to a better understanding of the underlying mechanisms of bubble formation in which the effects of the boundaries are considered. Also the contribution of the liquid circulation on the bubble formation is included in this study, which may be of practical importance to the design and operation of gas-liquid contacting process equipment.

1.3 Organization

To understand the underlying mechanism of bubble formation, it is necessary to review previous works studied by other researchers in this field. In Chapter 2, a detailed review of the theoretical and experimental research into bubble formation under various conditions will be presented. In addition, previous studies on bubble wake and wall effect on bubble formation will be discussed.

Chapter 3 gives an introduction of the boundary integral method and develops a theoretical model for bubble formation at a single orifice with this method. In addition, a model for the wall effect on bubble formation is developed using this method with an introduction of a specific image system.

Experimental work of wall effect on bubble formation will be described in Chapter 4, in which the experimental apparatus, measurement techniques, and experimental conditions and procedures will be introduced. Results and discussion of modeling of bubble formation and wall effect on bubble formation will be described in Chapter 5.

To obtain a comprehensive understanding about the bubble-bubble interaction as well as the bubble-wall interaction in bubble formation, a further spherical model is developed using potential flow theory in Chapter 6. The results and the comparison of the theoretical predictions and the experimental results will be also addressed.

Conclusions and recommendations arising from this study are summarized in Chapter 7.

Chapter 2 Literature review

2.1 Introduction

Bubble formation at a single submerged orifice has been investigated experimentally and theoretically in the past decades. Although practical applications may involve bubble formation at multiple orifices and a single orifice is rarely used in the gas-liquid contacting equipment in industry, an understanding of the fundamental process of bubble formation at a single orifice is a necessary prior to the investigation of equipment with multiple orifices.

This chapter first reviews the bubbling regimes at a submerged orifice in Section 2.2. Three main bubbling regimes, static, dynamic and jetting, are observed in order of increasing gas flow rate.

The performance of bubble formation is affected by many factors which include equipment variables, operating conditions and properties of the gas and liquid phases. It is very important to understand the effects of each factor so that devices, such as sieve tray columns, could be reliably and efficiently designed and controlled. The detailed discussion of these factors will be presented in Section 2.3.

Many theoretical models have been developed to describe bubble formation. These models will be discussed in Section 2.4. Literature pertinent to the bubble wake and the wall effect on bubble formation are presented in Sections 2.5 and 2.6 respectively. Finally, a brief summary is presented in Section 2.7.

2.2 Bubbling regimes

On the basis of experimental results, most researchers agree that there are three clearly defined regimes of bubbling. Beginning with small gas flow rate, these are static, dynamic and jetting regimes. The transition between each regime is not precise and depends on liquid physical properties, orifice size and chamber volume.

2.2.1 Static regime

The static regime occurs under the condition where only bubble buoyancy and surface tension play significant roles and there is equality between these two forces throughout the bubble formation. The gas flow rate is normally very low (< 1 cm^3/s) (Van Krevelen and Hoftijzer, 1950) and bubble remains a constant value at the detachment. The bubble volume is determined by orifice diameter and surface tension but is independent of gas flow rate as follows:

$$V_b = \frac{2\pi r_o \sigma}{(\rho_l - \rho_g)g} \tag{2.1}$$

where ρ_l and ρ_g are the liquid and gas densities respectively, g is the acceleration due to gravity, σ is the surface tension and r_o is the orifice radius. This regime is also called the "constant volume regime" which occurs when a dimensionless Reynolds number N_{Re} ($N_{\mathrm{Re}} = \frac{4\rho_g Q}{\pi d_o \mu_g}$) is less than 100, where Q is the volumetric gas flow rate into the gas chamber, d_o is the orifice diameter and μ_g is the gas viscosity.

2.2.2 Dynamic regime

The dynamic regime is also called the “slowly increasing volume region” by some investigators. In this regime, the gas flow rate is much higher and both bubble volume and frequency increase with the increase of gas flow rate ($N_{\mathrm{Re}} > 100$).

A more detailed discussion of bubble patterns in this regime has been reported by McCann and Prince (1971). Bubbling patterns were categorized into six modes as follows:

I. Single bubbling: Bubbles grows successively and discretely and there is no significant interaction between any two bubbles. It takes place when chamber volumes are small and gas flow rates are low.

II. Pairing: It occurs at low and moderate gas flow rates in the case of very large chamber volumes. The detachment of the bubble can cause an intermediate formation of an elongated gas tube due to the remaining pressure difference between chamber pressure and orifice pressure at the moment of the detachment. The gas tube then quickly elongates and joins with the bubble, connecting it momentarily with the orifice. After this tube breaks rapidly at the orifice, it moves into the preceding bubble.

III. Double bubbling: It occurs only at high gas flow rate or low chamber volumes. The second bubble is sucked into the preceding one due to a wake force caused by it and then two bubbles merger together and rise as one. The phenomenon is similar with pairing except that the second bubble cannot be regarded as a tube since its size is almost the same as the preceding bubble.

IV. Double pairing: Similar in behavior to double bubbling except that each is a pair.

V. Single bubbling with delayed release: The bubbling pattern is very similar to pairing except that there is no clear separation between the first bubble and the small gas tube.

VI. Double bubbling with delayed release: The bubbling behavior is very similar to single bubbling with delayed release except that there is also double bubbling as a following sequence behind each single delayed release behavior.

In particular, McCann and Prince (1971) compared the phenomena of pairing and double bubbling, as shown in Table 2.1.

Table 2.1 Comparison between pairing and double bubbling

Pairing	Double bubbling
Large chamber volumes	Small chamber volumes
Bubbling with a “tail”	Two distinct bubbles
No weeping between the bubble and the formation of its “tail”	Weeping may occur between the two bubbles

Fig. 2.1 shows the state diagram of McCann and Prince (1971) for a 4.7 mm orifice in an air-water system. The conditions were summarized under which each of these six categories was observed to occur.

2.2.3 Jetting regime

With an increase of the gas flow rate, the bubbling regime loses its stability. Bubbling is characterized by the onset of rapid sequential formation of bursts. This regime is called the "jetting regime". The phenomenon of jetting normally occurs at higher Reynolds number ($N_{\mathrm{Re}} > 2000$) (McNallan and King (1982)).

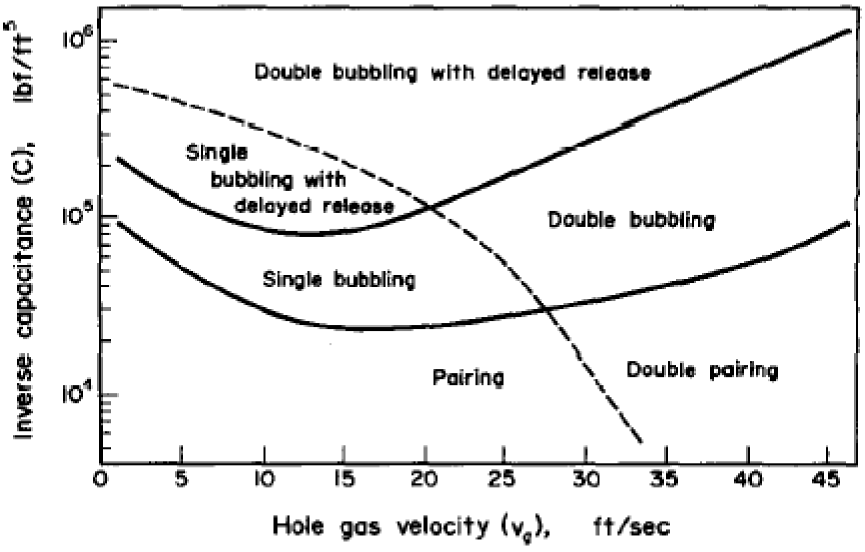

Fig. 2.1 Bubble state diagram of McCann and Prince (1971) for a 4.7 mm orifice in an air-water system

2.3 Physical factors affecting bubble formation

Many factors have been investigated having influence on bubble formation at a single submerged orifice. In general, these factors are related to the physical construction of the bubbling system as well as the gas and liquid properties. These factors may be classified according to Kumar and Kuloor (1970), McCann and Prince (1971), and Tsuge and Hibino (1983) as: equipment variables (e.g., orifice diameter, chamber volume, etc.), system variables (e.g., liquid properties, gas properties, etc.), and operating variables (e.g., gas flow rate, static system pressure, liquid depth, bulk liquid motion, etc.).

2.3.1 Orifice diameter

Orifice diameter effects depend on bubbling regimes as well as bubble formation conditions. In the static regime, the volume of the bubble is proportional to the orifice diameter as expected from Equation (2.1). In the dynamic regime, orifice diameter is unimportant for a constant flow condition ($V_c \rightarrow 0$), but at a constant pressure condition ($V_c \rightarrow \infty$) and intermediate condition, the flow through the orifice is proportional to the cross sectional area, making the orifice diameter a very important factor. Additionally, a larger orifice diameter also gives rise to a larger line tension force at the gas-liquid-solid interface, increasing resistance to bubble detachment and therefore resulting in a larger bubble volume (Mittoni, 1997). In the turbulent regime, bubble volume is independent of orifice diameter and depends on the stochastic breakup of the gas jet.

2.3.2 Chamber volume

Gas chamber volume has a significant effect on bubble formation. In terms of the chamber volume, bubble formation can be categorized into constant flow, constant pressure, and intermediate conditions. The two limits of chamber volume ($V_c \rightarrow 0$ and $V_c \rightarrow \infty$) define the special cases of constant flow and constant pressure conditions, respectively.

Constant flow condition occurs in small gas chamber volume systems, corresponding to large orifice pressure drop due to either high gas flow rate or large orifice resistance. The changes in the gas chamber or bubble pressure have a relatively small effect on the pressure drop. The gas flow rate tends toward a constant value.

The occurrence of constant pressure arises for a large chamber volume and fixed chamber pressure (Kupferberg and Jameson, 1969; Park et al., 1977). Under such a condition, the pressure fluctuation due to the bubble formation and detachment is small. Therefore the chamber pressure remains virtually constant.

A dimensionless capacitance number, N_c, first proposed by Hughes et al. (1955), is generally applied to describe chamber volume effects as follows:

$$N_c = \frac{4g(\rho_l - \rho_g)V_c}{\pi d_o^2 \rho_g {c_o}^2} \tag{2.2}$$

where V_c is the gas chamber volume and c_o is the velocity of sound in the gas. Hughes et al. postulated that $N_c = 0.85$ is the critical value to describe the gas chamber effect. When $N_c < 0.85$ the bubble volume is found to be nearly independent of chamber volume.

Tadaki and Maeda (1963) also proposed a dimensionless capacity number, $N_c^{'}$, for constant volume bubbling as:

$$N_c^{'} = \frac{4\rho_l g V_c}{\pi d_o^2 P_s} \tag{2.3}$$

where P_s is the static pressure at the liquid surface. If $\rho_l \gg \rho_g$ and $P_c = P_s$, $N_c{'}$ is equal to is γN_c, where γ is the specific heat ratio of gas (Tsuge and Hibino, 1983).

Tadaki and Maeda (1963) found that bubble volumes were scaled by a factor of N_c' for $N_c' > 1.0$ to an upper limit where the volumes became constant at $N_c' = 9.0$.

2.3.3 Liquid properties

Liquid physical properties which affect bubble formation include viscosity, density and surface tension.

It is generally accepted that viscosity affects the bubble volume insignificantly at lower gas flow rates and lower liquid viscosities; while at large gas flow rates and high viscosities, the viscosity effects on bubble volume become significant due to the high drag force retarding upward acceleration of the bubble. Miyahara et al. (1983) investigated the effects of liquid viscosities on bubble formation both experimentally and numerically. The orifice diameters ranged from 1.0 and 3.0 mm and liquid viscosities ranged from 0.001 to $0.147\, kg/m \cdot s$. The two-stage bubble formation model developed in the investigation was in agreement with experimental observations. The results illustrated that larger viscosities caused larger bubble volumes because it decreased bubble rise velocity and allowed more gas to enter the bubble before detachment. Terasaka and Tsuge (1990) improved the non-spherical model proposed by Pinczewski (1981) by including a viscosity term in the motion of the bubble and modifying the equivalent radius definition. Agreement with experimental data from their own study as well as other researchers was close for liquid viscosities between 0.001 and $1.1\, kg/m \cdot s$ under atmospheric conditions.

Besides viscosity, liquid density is also a factor affecting bubble formation. In general, higher liquid density causes higher bubble buoyancy which forces the bubble to detach with a smaller volume if surface tension remains constant. Davidson and Schüler (1960a) concluded that liquid density had insignificant effects on the bubble volume at high gas flow rates because the relative increase of the liquid inertia retarded the increase of the buoyancy. Meanwhile, a higher liquid density could increase the pressure gradient during bubble formation, resulting in increased gas flow rates into the bubble. McCann and Prince (1969) also suggested that the pressure at the orifice which depended on the liquid density determined the gas flow into the bubble. These evidences of the weak dependence on density might be due to the low chamber volumes used by many researchers, thereby restricting their studies to constant gas flow conditions.

Surface tension is one of the most important factors determining the bubble size at vanishingly small flow rates, however, it assumes much less importance at higher flow rates. The significance of surface tension also decreases with the increase of the bubble diameter. Al-Hayes and Winterton (1981) described the growth of air bubbles in water, water with surfactants, and ethylene glycol on various surfaces exhibiting different contact angles. They concluded that for the surface active agents used there was little evidence that they produced a skin around the bubble that significantly impeded the mass transfer.

2.3.4 Gas properties

It is generally accepted that gas density, pressure and heat capacity can influence bubble formation. While molecular weight of gas is considered to have a weak negative impact on the bubble volume in the gas-liquid contacting system.

Davidson and Schüler (1960a) found that bubble volume decreased 1.8% when changing the gas from air to carbon dioxide for a gas flow rate of 17 ml/s under constant flow condition, owing to the difference of the gas momentum caused by different gas densities.

LaNauze and Harris (1974) showed experimentally that gas density had a significant impact on the gas momentum and the capacity of the gas chamber by increasing the pressure in the gas phase of carbon dioxide up to 2.0 MPa. The experimental results showed to be in good agreement with the mathematical model proposed by LaNauze and Harris (1974).

Tsuge and Hibino (1983) stated that the specific heat ratio of gas, γ, also affected bubble volume depending on the dimensionless capacitance number $N_c^{'}$. When $N_c^{'}$ was small, bubble volumes were affected mainly by the specific heat ratio of the gas, but when $N_c^{'}$ was large, they were affected strongly by gas density.

Wilkinson and Van Dierendonck (1994) found that an increase of gas density for large chamber volumes can lead to smaller bubble at formation due to an increase in gas momentum, an increase in pressure drop at the orifice and an increased rate of bubble necking.

The viscosity of the gas is generally expected to have insignificant effects on bubble formation, but it has an appreciable effect in impeding the gas flow into the bubble. Fountain (1988) stated that the weak influence of gas viscosity determined pressure drop and supply conditions of the gas delivery system, and the effect was significant only when injecting through long thin tuyeres.

2.3.5 Gas flow rate

Gas flow rate has a significant effect on bubble volume as well as bubble frequency. There exists a general agreement on the pattern of bubble volume variation when the flow rate is increased. In the static regime, as the flow rate is gradually increased from zero, the bubble volume which could be obtained with Equation (2.1) remains fairly independent of the flow rate, whereas the frequency increases. In the dynamics regime, with the increase of the flow rate, at first both the bubble volume and the frequency increase, but later on a stage is reached where the frequency remains essentially constant whereas the bubble volume continues to increase. Though these regions are observed for all the systems studied, the conditions under which one region ends and the other begin are not clear. Finally, with the increase of the gas flow rate, the bubble formation process loses its stability and is characterized as jetting regime.

2.3.6 Static system pressure

LaNauze and Harris (1974) investigated the effect of elevated system pressure on submerged gas injection. They found that the bubble size decreased significantly with the increase of the system pressure, especially at high gas flow rate. The relationship between bubble volume and gas flow rate became non-linear at higher system pressures. LaNauze and Harris (1974) also found that higher pressures affected the coalescence behavior between successive bubbles for a given gas flow rate. The increased gas momentum due to the higher system pressure led to a smaller bubble volume and hence reduced the time delay between individual bubbles.

Wilkinson and Dierendonck (1990) stated that the influence of both pressure and gas molecular weight on bubble formation had same cause. The effect of pressure on the bubble size could be explained by the decrease in bubble stability with increasing gas density.

Tsuge et al. (1992) studied the effect of system pressure under the conditions of gas chamber volume 12.8 cm^3, orifice diameter 1.18 mm, and gas chamber volume 368 cm^3, orifice diameter 1.48 mm, respectively. They found that bubble volume decreased with the increase of system pressure both experimentally and theoretically.

2.3.7 Liquid depth

Liquid depth is chosen as one of the variables in the studies of bubble formation. It is generally agreed that this variable does not influence the bubble volume at the tip. This fact has been verified when the liquid depth was greater than approximately two bubble diameters (Davidson and Amick, 1956; Hayes et al., 1959).

However, Khurana and Kumar (1969) indicated that only under constant flow and constant pressure conditions, bubble volumes were not significantly influenced by the liquid depth. While for the intermediate condition, bubble volumes were observed to decrease exponentially with the increase of the liquid depth from 15 cm to 128 cm for orifice diameter 3 mm. Iliadis et al. (2000) investigated the influence of the liquid depth on bubble formation for various orifice diameter and gas chamber volume in the single bubbling region. They found that the bubble size increased with the increase of the liquid depth in the range of 10 to 150 cm with the conditions of orifice diameters from 1.15 to 4.35 mm and chamber volume from 150 to 7000 cm^3.

2.3.8 Bulk liquid motion

There are two types of bulk liquid motion, namely erratic liquid oscillation and forced liquid bulk flow. The former is induced by bubble formation and upward rising motion and it is very difficult to account for rigorously. The later is evoked by means of external force exerted on the liquid body and most of the investigations about the effect of liquid flow on bubble formation have been focused on it.

Bubble formation in co-flowing or counter-flowing liquid under constant gas flow conditions has been investigated both experimentally and theoretically (Sada et al., 1978; Takahashi et al., 1980; Fawkner et al., 1990 and Chen and Tan, 2002). All the investigations reported that the bubble volume decreased with increasing superficial liquid velocity.

Bubble formation with cross-flowing liquid is another case usually met in many industrial gas-liquid operations. The liquid motion results in a drag force on the growing bubble, thereby causing earlier bubble detachment and producing smaller bubbles when compared with formation under stagnant or quiescent liquid conditions. Another advantage of cross-flowing liquid is that the detached bubbles tend to be swept away from the region of the orifice, thereby reducing the likelihood of coalescence. Theoretical models for bubble formation with cross-flowing liquid have been developed by Tsuge et al. (1981), Wace et al. (1987), Marshall et al. (1993), Kim et al. (1994), Tan et al. (2000) and Zhang and Tan (2003).

2.4 Mathematic modeling

Most theoretical studies of bubble formation have been concentrated on the single bubble formation in a quiescent liquid. The extensive theoretical study on this subject gives a fundamental understanding of the bubble formation process, growth and detachment size and detachment time throughout a wide range of conditions of gas flow rate, chamber volume, orifice size, gas and liquid properties as well as system pressure. Some reviews on this area include the articles by Kumar and Kuloor (1970), Tsuge (1986), Tan and Harris (1986), and the monographs by Clift et al. (1978), Sadhal et al. (1997).

In general, the existing models for bubble formation in a quiescent liquid can be classified into two broad categories, i.e., spherical models and non-spherical models.

2.4.1 Spherical models

Based on the analytical solution of force balance equations or equations of motion, many spherical models have been developed (Davidson and Schüler, 1960a, b; Khurana and Kumar, 1969; LaNauze and Harris, 1972; and Tsuge and Hibino, 1983). According to the definition of the bubble formation stages, these models could be classified into one-stage model, two-stage model and three-stage model.

2.4.1.1 One-stage models

Davidson and Schüler (1960a, b) proposed a series of one-stage models to describe bubble formation in both viscous and inviscid liquids for the two main bubbling regimes, i.e., constant flow and constant pressure regimes. The schematic diagram of the idealized one-stage model of Davidson and Schüler (1960a) is shown in Figure 2.2. It was assumed that the bubble detached when the vertical distance between the center of the bubble and the point of gas supply, s, was equivalent to the final bubble radius, a. Thus there was no distinction between the expansion and detachment stage. It was assumed that the velocity of the bubble center was determined by a force balance between the buoyancy force and the viscous drag while neglecting the inertia term. Although the predicted results agreed well with the experimental data, the models were limited to be used for very small gas flow rates.

Swope (1971) applied Newton's second law to slow bubble formation in viscous liquids with pressure fluctuation in the gas chamber. The gas flow rate into the bubble was determined by multiplying the average gas flow rate into the chamber with the ratio of the bubbling time to the sum of bubbling and non-bubbling times.

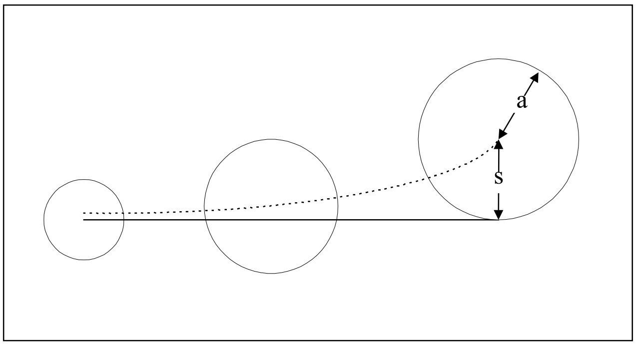

Fig. 2.2 One-stage model in quiescent liquid by Davidson and Schüler (1960a)

With a modification of Davidson and Schüler's (1960a, b) model, LaNauze and Harris (1972) developed a one-stage model for bubble formation in the constant pressure regime. The proposed bubble formation sequence is illustrated in Figure 2.3. Initially, the bubble center is at a point source of gas, the center of the upper face of the orifice. Its upward motion is determined by a balance between the forces acting on the bubble and the inertia of the liquid surrounding it. Later, LaNauze and Harris (1974) extended their earlier model to allow for the rate of change of gas momentum issuing through the orifice and variable gas chamber pressure. They studied the effects of gas momentum on the bubble formation at elevated pressure.

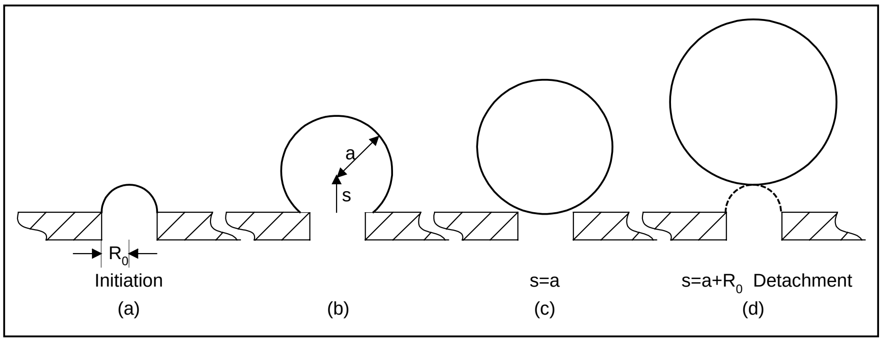

Fig. 2.3 One-stage model in quiescent liquid by LaNauze and Harris (1972)

2.4.1.2 Two-stage models

Following the development of one-stage models, two-stage models, which took the bubble necking into account, were proposed by Ramakrishnan et al. (1969), Satyanarayan et al. (1969), Khurana and Kumar (1969), Ruff (1972), and Takahashi and Miyahara (1976,1979). The idealized two-stage bubble formation model by Ramakrishnan et al. (1969) is shown in Figure 2.4.

In the model, bubble formation was assumed to consist of two stages: expansion stage and detachment stage. During the first stage, expansion stage, the spherical bubble expands while its base remains attached to the orifice. This stage is assumed to end when all the forces acting on the bubble are just balanced, so that the bubble begins to rise. In the second stage, detachment stage, the bubble continues to grow while lifting up from the plate, but is still connected to the orifice by a neck. This stage terminates when the neck breaks off and the bubble detaches. It is assumed that the bubble detaches when the length of the neck reaches an empirical value. This is similar to the detachment criterion of Davidson and Schüler (1960a, b).

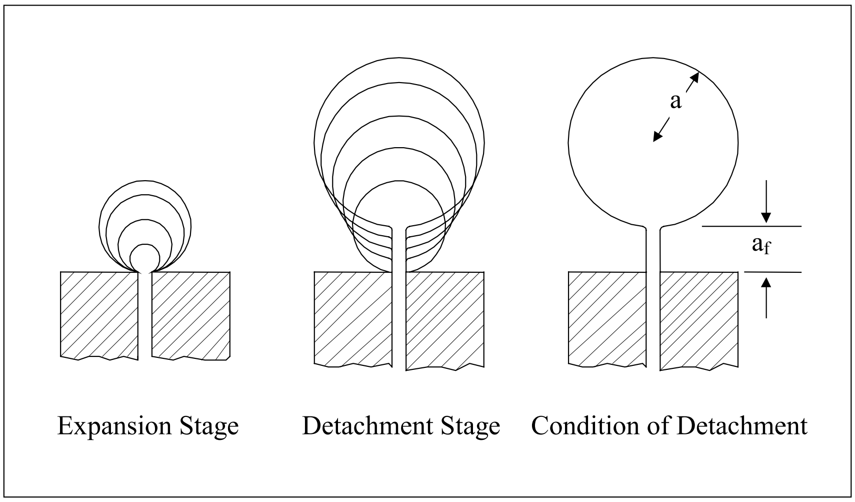

Fig. 2.4 Two-stage model in quiescent liquid by Ramakrishnan et al. (1969)

The two-stage model for bubble formation at a plate orifice submerged in an inviscid liquid at high gas flow rates was proposed by Wraith (1971). In the model, the surrounding liquid was assumed to be inviscid and of infinite extent. The gas was incompressible and its density was neglected. Surface tension was neglected in the model. Figure 2.5 shows the two successive stages schematically during bubble growth. At the beginning of bubble expansion from a point source, the gas bubble surface was assumed to be a hemisphere, with its radius equal to the orifice radius. The bubble became spherical about the center of mass of a hemispherical envelope at the end of the first stage. In the second stage, the force balance equation for a spherical bubble growing at the orifice was assumed to be given by the Davidson and Schüler's (1960a, b) model, and neglecting the viscous force.

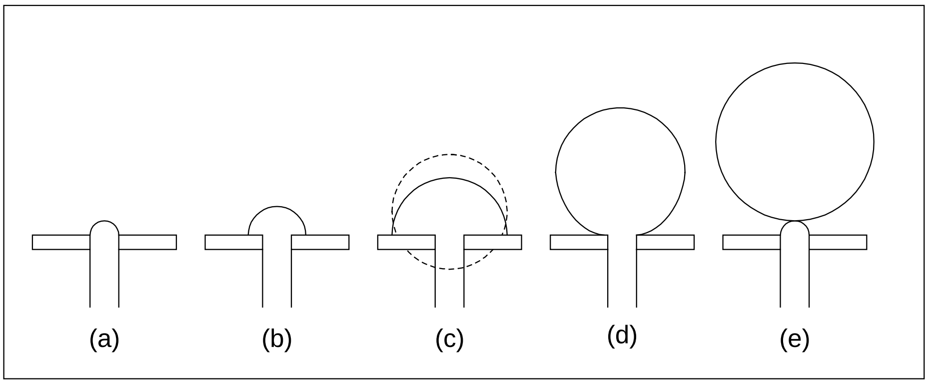

Fig. 2.5 Two-stage model in a quiescent liquid by Wraith (1971)

2.4.1.3 Three-stage models

Although the results predicted by the previous models agreed reasonably well with some experimental observations, there was criticism that the models were only applicable in a certain range of experimental conditions. With potential flow theory, three-stage models were developed by several authors (Kupferberg and Jameson, 1969; McCann and Prince, 1969; Tsuge and Hibino, 1983).

The idealized three-stage bubble formation model proposed by Kupferberg and Jameson (1969) is illustrated in Figure 2.6. The three stages are the growth stage, elongation stage and waiting stage. The first two stages were similar to the two-stage model of Ramakrishnan et al. (1969). In the waiting stage, it was assumed that there was no outflow of gas from the chamber after the detachment of a bubble. Hence the pressure in the chamber increased and the next bubble began to form. During a part of waiting stage, weeping through the orifice might occur. Potential flow theory was employed in the model to calculate bubble and liquid motion.

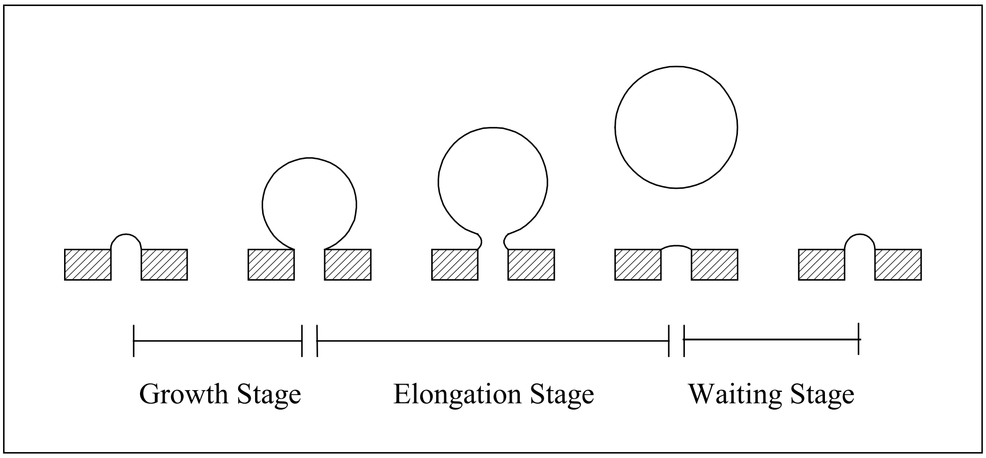

Fig. 2.6 Three-stage model in a quiescent liquid by Kupferberg and Jameson (1969)

Independently with Kupferberg and Jameson (1969), McCann and Prince (1969) derived a potential flow theory to describe the gas flow from the gas chamber into an expanding, rising spherical bubble forming at the orifice, by taking into account the wake behind preceding bubble.

Tsuge and Hibino (1983) proposed another three-stage model with modified potential flow theory. For the ideal liquid, Kupferberg and Jameson (1969) and McCann and Prince (1969) derived the functional form of potential velocity ϕ from the potential flow theory, but for a real liquid it was difficult to derive theoretically the concrete form of potential velocity ϕ. Hence Tsuge and Hibino (1983) proposed that ϕ was expressed as the product of the inertial term for the ideal liquid and a factor which was a function of dimensionless liquid property.

2.4.2 Non-spherical models

The spherical models just described in the Section 2.4.1 have assumed the spherical shape of the bubble and have been forced to use an empirical or semi-empirical criterion to determine the instant of the detachment. Non-spherical models enable continuous computation of instantaneous shape of the bubble during its formation using the equations of motion for the liquid and the thermodynamic relationships for the gas in the bubble and the gas chamber, there is no need for the empirical detachment criteria because the instant of detachment comes naturally at the time when the neck, which develops during formation, attains zero width. In addition, the bubble becomes increasingly non-spherical at higher gas flow rates and higher system pressures and it is not good to describe the bubble as spherical. To overcome these limitations, non-spherical models for bubble formation were developed by a number of researchers.

2.4.2.1 Non-spherical model by Marmur and Rubin

Marmur and Rubin (1976) proposed a non-spherical model which showed a significant forward leap over the previous spherical models. Their model assumed an inviscid liquid, with liquid inertia calculated through the “added mass” concept of inviscid flow theory. The growing bubble was a volume of revolution around the vertical axis. The gas-liquid interface was divided into a number of small elements and the position of each element at any time instant was determined by the time-dependent force balance. Each element was acted upon by the pressure difference between the gas and the liquid and by the surface tension force. For a static interface these forces were in equilibrium, but in dynamic formation the resultant of these forces was equal to the rate of change in the liquid momentum, assuming that the gas momentum was negligible. In order to avoid the extremely complicated solution of the Navier-Stokes equations for the motion of the liquid, the momentum of the liquid was determined by using the “added mass” concept and the velocity of the interface. The effect of the chamber volume on bubble formation was analyzed by applying thermodynamic equations for the gas in the bubble and the chamber below the orifice plate. A finite difference procedure was subsequently used to solve the equations of motion for each element.

In contrast with previous spherical models, this model was able to predict the instantaneous shape of the bubble during its formation. The bubble shapes predicted agreed well with video images taken by researchers such as Kupferberg and Jameson (1969).

Although the results predicted by this model were in good agreement with experimental data, there were several shortcomings. Contributions due to gas momentum and liquid circulation around the bubble were neglected in this model. It had been shown that gas momentum had a significant effect on bubble growth at high system pressures (LaNauze and Harris, 1974). Hence this model was limited to low gas flow rates and atmospheric conditions. In addition, an empirical added mass coefficient of 0.85 was used to provide a good fit to the data. This was in contrast to the widely accepted value of 11/16, which was based on the hydrodynamics of a sphere moving perpendicularly to the wall in an inviscid fluid (Milne-Thomson, 1968).

2.4.2.2 Non-spherical model by Pinczewski

The model proposed by Pinczewski (1981) extended the description of bubble formation by including the effect of gas momentum. The contribution of gas momentum was introduced by assuming a pressure distribution due to spherical vortex motion of the gas within the bubble. An initial “expansion” stage was described by the modified Rayleigh equation of motion for a spherically expanding bubble:

$$P_b - P_l = \rho_l \left(R\frac{d^2R}{dt^2} + \frac{3}{2}\left(\frac{dR}{dt}\right)^2 \right) + \frac{2\sigma}{R} + \frac{4\mu}{R}\frac{dR}{dt} - \frac{1}{2}\rho_g V_h^2 \cos^2\theta \qquad (2.4)$$

where the four terms on the RHS of Equation (2.4) represented the inertia, surface tension, viscous forces, and the pressure distribution due to gas motion, respectively. The equation was assumed to be equally valid for any point on a non-spherical surface where R became the equivalent radius of the surface as defined in the following equation:

$$\frac{2}{R} = \frac{1}{R_1} + \frac{1}{R_2} \tag{2.5}$$

and R_1 and R_2 were the principal radii of curvature.

A static buoyancy force was used to determine the instant of "lift-off" and the commencement of a stage when "expansion" and "vertical translation" occurred simultaneously.

Although this model was able to provide a more general description of bubble formation, which would be applicable to a wider range of gas flow rates and system pressures, there were several inadequacies. The spherical equation of motion and spherical gas stream function were applied to model bubble formation. In addition, the two-stage approach to bubble formation used in the model contained fundamental theoretical weaknesses.

Terasaka and Tsuge (1990) adopted Pinczewski's approach and proposed a modified theoretical model for bubble formation in viscous liquids. The schematic diagram of the non-spherical model by Terasaka and Tsuge (1990) is shown in Figure 2.7. In their model, the equivalent radius R was only used for surface tension, and R_2, the distance from the bubble's symmetrical axis to the element i throughout the point O, was used for inertial and viscous forces as the characteristic radius. The expansion of the gas-liquid interface was written by the following Rayleigh Equation:

$$P_b - P_l = \rho_l \left(R_2 \frac{d^2 R_2}{dt^2} + \frac{3}{2}\left(\frac{dR_2}{dt}\right)^2 \right) + \frac{2\sigma}{R} + \frac{4\mu}{R_2}\frac{dR_2}{dt} \tag{2.6}$$

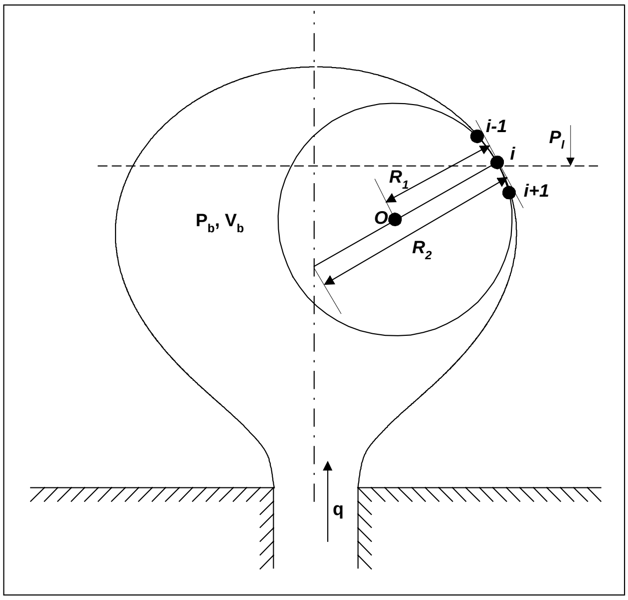

Fig. 2.7 Non-spherical model in quiescent liquid by Terasaka and Tsuge (1990)

By revising Pinczewski's model, the equation of vertical translation was described by inertial, buoyancy, and viscous drag forces and gas momentum rate through an orifice as follows:

$$\frac{d}{dt}\left(\overline{m}\frac{dz}{dt}\right) = \left(\rho_l - \rho_b\right)V_b g - \frac{1}{8}C_D \rho_l \left(\frac{dz}{dt}\right)^2 \pi D_m^2 + \frac{\rho_b q^2}{\pi R_o^2} \tag{2.7}$$

where $\overline{m}$ was the added mass, C_D was the drag coefficient, D_m was the maximum horizontal diameter of the bubble and q is the gas flow rate through the orifice.

The bubble surface expanded and the bubble rose according to Equations (2.6) and (2.7). A finite difference procedure was used to solve the equations numerically. Their non-spherical model still contained the same inadequacies as presented in the original model by Pinczewski.

Li et al. (2002) developed a non-spherical bubble formation model by revising that of Pinczewski (1981), which was used in Newtonian fluids, to take into account the fluid rheological properties. In their model, the influence of in-line interactions between bubbles due to the fluid memory effects of the viscoelastic characteristics was taken into account. Their model was able to compute the instantaneous growing shape of the bubble during its formation and determine the final size of detachment as well as the frequency of bubble formation. However, their model also contained the same disadvantage as presented in the original model by Pinczewski, in that the equivalent radius was used in two spherical equations of motion: the radial expansion and vertical ascension of the bubble interface.

2.4.2.3 Non-spherical model by Zughbi et al.

Zughbi et al. (1983) were one of the earliest researchers attempting the modeling of bubble formation by the rigorous numerical solution of liquid field around the bubble. A fundamental analysis of the motion of the liquid surrounding the bubble and its influence on bubble growth were presented. The model was based on a modified Marker and Cell method in which the liquid region bounded by the bubble surface, the orifice plate, the vessel walls and the free liquid surface was divided into a number of cells. The unsteady, incompressible and axisymmetric Navier-Stoke equations describing the liquid flow field around the growing bubble were solved for each cell using a staggered finite difference method. Massless marker particles, which moved with the local velocity of the liquid, were distributed along the bubble surface.

The model prediction was in agreement with the experimental data of Kupferberg and Jameson (1969). Besides having the obvious advantages associated with non-spherical models, the model was able to predict the effects of solid walls and free liquid surface on bubble formation. This was an improvement over previous non-spherical models.

However, one shortcoming of this model was its high degree of numerical complexity. In addition, the model did not take into account the effect of gas momentum. Therefore, the model was more suitable for low gas flow rates and atmospheric pressure conditions.

2.4.2.4 Non-spherical model by Hooper

Independently from Zughbi et al. (1983), Hooper (1986) proposed another model based on the solution of the liquid flow field around the bubble surface. The boundary element method was adopted in the model. The surrounding liquid was assumed to be inviscid and the flow was irrotational. Therefore, the velocity potential ϕ could be introduced and it satisfied Laplace's Equation, i.e.

$$\nabla^2\phi = 0 \tag{2.8}$$

The derivative of ϕ normal to the bubble surface was obtained with the boundary element method and the tangential velocity of the bubble surface could be obtained with the cubic spline method along the bubble surface. Whence the velocities in the radial and axial direction could be calculated and together with thermodynamic equations for the gas, the instantaneous shape of the bubble during its formation could be predicted.

The model presented a comprehensive analysis of the role of the surrounding liquid in the detachment process of the bubble and was able to compute the bubble shapes and streamline patterns of the liquid at various stages of bubble growth. It was found that the expanding and rising bubble caused unsteady stagnation point flow to occur in the liquid. Thus an inward flowing region of liquid existed which caused the bubble to neck.

However, in Hooper’s model, the surface tension term was neglected in order to avoid numerical instability during bubble formation.

2.4.2.5 Non-spherical model by Tan and Harris

An improved non-spherical model for bubble formation was developed by Tan and Harris (1986). The model was based on the interfacial element method, which ascribed a virtual mass to each surface element of the bubble, and did not require an arbitrary detachment criterion, nor did it use a static “lift-off’ criterion to distinguish between separate stages of bubble growth. The effect of gas momentum and liquid motion were taken into account in their model so that their model was applicable in bubbling systems under high system pressure and high gas flow rates. The model predictions agreed very well with the experimental data of Kupferberg and Jameson (1969), LaNauze and Harris (1972) and Tsuge and Hibino (1978). Several other workers have adopted the model proposed by Tan and Harris (1986) to extend its applicability (Liow and Gray, 1988; Wilkinson and van Dierendonck, 1994).

2.5 Bubble wake and rise velocity after detachment

The term "wake" is applied, in a broad sense, to the entire region of non-zero vorticity downstream of a body placed in an otherwise uniform fluid flow (Fan and Tsuchiya, 1990). Liquid wake pressure behind a rising bubble plays a significant role in determining bubble interaction (Tsuchiya et al., 1996; Chen et al., 1999; Colella et al., 1999; Li et al., 1999). The effect of a rising bubble on subsequent ones depends on the bubble size and the separation distance, as indicated by Marmur and Rubin (1976): when the bubble is small and the time interval between consecutive bubbles drops to almost zero, the ascending bubble tends to delay the detachment of the forming bubble; when the bubble which has been formed is large, it tends to detach the forming bubble earlier, due to the rotational motion which is induced by it in the liquid. Compared to other factors, bubble wake effects have received relatively less attention.

2.5.1 Wake pressure

For gas bubbles formed in low viscosity liquid media (such as water), potential flow theory is often employed to analyze the distinct pressure field behind the bubble when the liquid flow is assumed as irrotational motion.

Jameson and Kupferberg (1967) discussed the wake pressure behind a spherical bubble and cylindrical bubble accelerating from rest. For a spherical bubble, the expression for wake pressure is

$$\frac{\Delta P}{\rho_L g a} = \frac{3}{\tilde{s}^2} - \frac{4}{\tilde{s}^3} - \frac{2}{\tilde{s}^5} + \frac{2}{\tilde{s}^6} \tag{2.9}$$

where ΔP is the pressure change at the rest point (orifice, $s = 0$), namely the wake pressure; a is the bubble radius and the dimensionless distance $\tilde{s} = s / a$.

For a cylindrical bubble, the expression is

$$\frac{\Delta P}{\rho_L g a} = \frac{1}{\tilde{s}} - \frac{2}{\tilde{s}^2} - \frac{1}{\tilde{s}^3} + \frac{1}{\tilde{s}^4} \tag{2.10}$$

Equations (2.9) and (2.10) are plotted in Fig. 2.8. It seems that initially the pressure behind the bubble is less than the ambient, but after it has moved a short distance, ΔP becomes positive. This indicates that the point from which the bubble departs (the rest point) is acted upon by a short pressure decrement and then by a much longer excess, compared with the pressure at a distance from the bubble. The maximum pressure excess occurs at $\tilde{s} = 2.15$ for a sphere. The authors pointed out two main sources of error for ΔP. Firstly, viscosity begins to be important as U increases so the bubble tends to stop accelerating. Secondly, the bubble will deform from the spherical shape, so that the assumed form of velocity potential function will be in error.

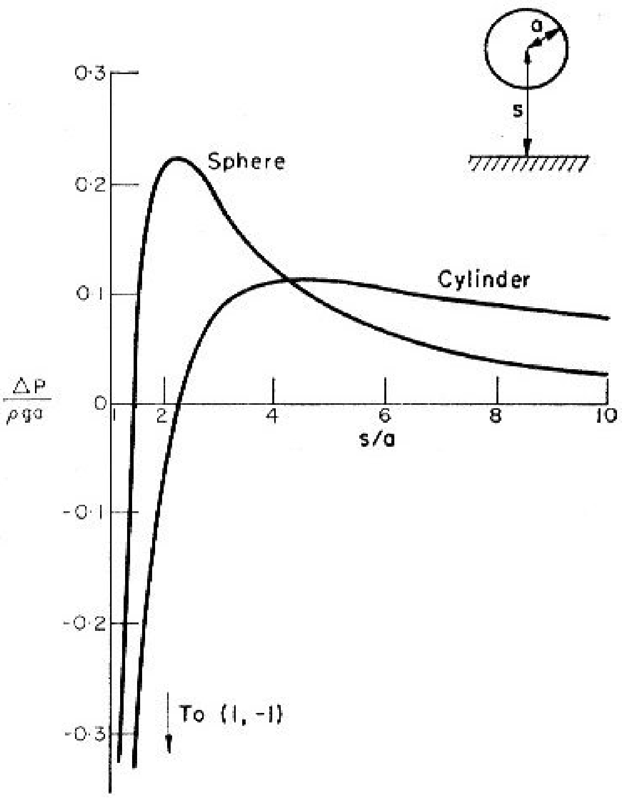

Fig. 2.8 Pressure at the rest point behind a sphere or cylinder accelerating from rest (adapted from Jameson and Kupferberg, 1967)

Using potential flow theory, McCann and Prince (1969) analyzed the wake pressure behind the rising bubble, which was determined using Bernoulli's expression in combination with the velocity potential of a rising expanding bubble. The wake pressure expression is:

$$P_w = \frac{\rho_L a_{DET}^3 U_D^2}{s_D^3}(1 - \frac{a_{DET}^3}{2s_D^3}) - \frac{\rho_L \dot{U}_D a_{DET}^3}{2s_D^2} \tag{2.11}$$

where

$$s_D = s_{DET} + U_{DET}T + gT^2$$

$$U_D = U_{DET} + 2gT$$

The subscript $_{DET}$ refers to conditions on detachment and the time T has its origin at detachment. It was pointed out that this pressure correction to the bubble motion is small at low flow rates, where the distance between successive bubbles is large. As the flow increases, the spacing between bubbles reduces and the effect becomes more marked. Under these circumstances double bubbling is possible. Calculations indicate that P_w can cause up to 20 per cent increase in bubble volume (McCann, 1969).

Wraith and Kakutani (1974) established the pressure field for an idealized growing spherical gas bubble rising in an inviscid liquid from a horizontal plate-orifice and from a free standing nozzle on the basis of potential flow. The pressure curve is similar to that obtained by Jameson and Kupferberg (1967). The authors argued that the maximum pressure behind the bubble was responsible for the collapse of the neck linking the bubble and the gas source.

Nilmani (1982) considered liquid viscosity as well as the distortion of the detached bubble and came up with an improved approach to predict bubble wake effect. Direct solution of the continuity and momentum equations is obtained by the finite difference method. He compared his numerical simulation results with Jameson and Kupferberg's (1967) potential flow prediction for a two-dimensional bubble (cylindrical bubble) and a three-dimensional bubble (spherical bubble). The results are shown in Fig. 2.9 and Fig. 2.10. Although the curve is directly obtained from solution of the transport equations, the trend and magnitude is nevertheless similar to the prediction of potential flow theory.

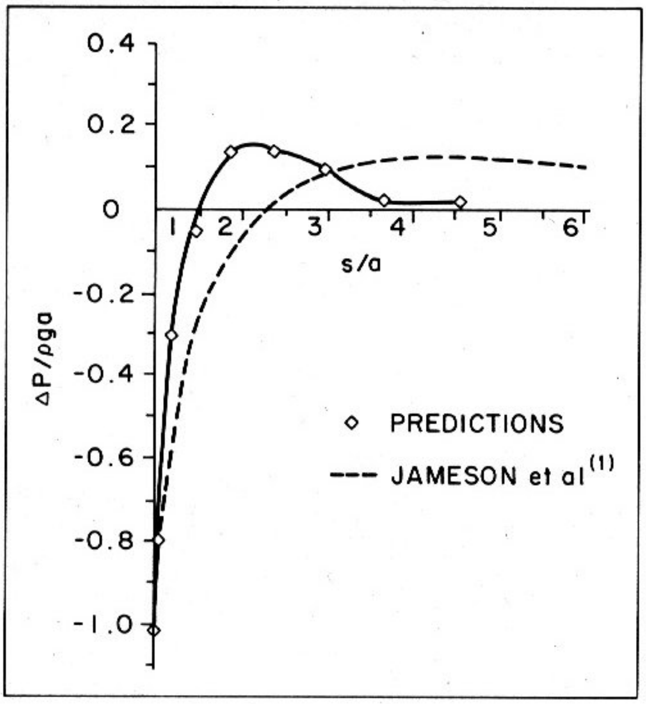

Fig. 2.9 Pressure at the orifice left behind by a 2-D air bubble in water accelerating from rest (adapted from Nilmani, 1982)

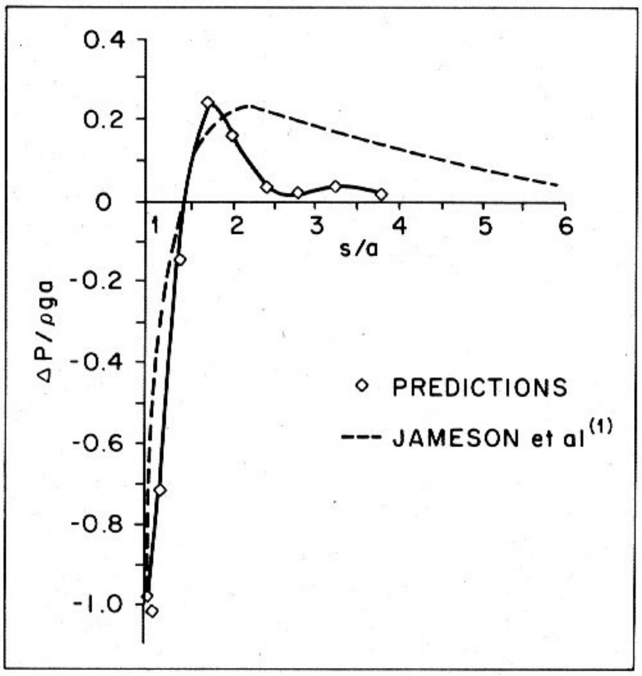

Fig. 2.10 Pressure at the orifice left behind by a 3-D air bubble in water accelerating from rest (adapted from Nilmani, 1982)

Due to the inherent inability of potential flow theory to model the vorticity behind bubbles as experimentally observed, the above approaches are flawed.

Fan and Tsuchiya (1990) discussed the pressure distributions around rising bubbles based on some experimental findings and presented a simple theoretical description of the pressure field for an idealized vortical flow. Fig. 2.11 shows the isobaric representation of the pressure field around a bubble of $d_e = 51$ mm ($\mathrm{Re}_e = 2.67 \times 10^4$) obtained by Lazarek and Littman (1974) as a cross-plot of the measured pressure-time relations along the longitudinal axes at various lateral displacements.

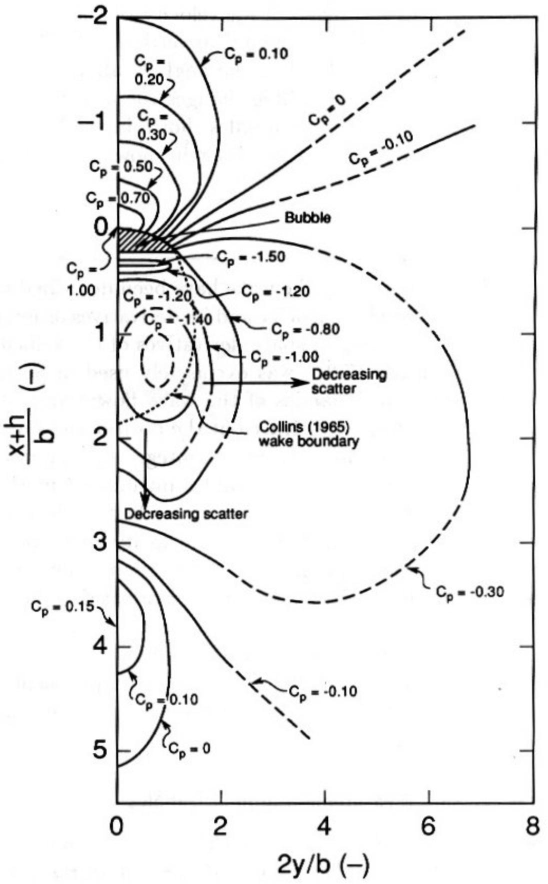

Fig. 2.11 Isobaric representation of the pressure field around a circular-cap bubble (adapted from Fan and Tsuchiya, 1990)

After some simplifying assumptions, Fan and Tsuchiya (1990) gave the pressure distribution within and around the vortex core as follows:

$$\frac{p_1}{p_{st}} = 1 - \frac{\rho_L}{p_{st}}(\frac{\Gamma}{2\pi r_v})^2[1 - \frac{1}{2}(\frac{r}{r_v})^2] \tag{2.12}$$

$$\frac{p_2}{p_{st}} = 1 - \frac{1}{2}\frac{\rho_L}{p_{st}}(\frac{\Gamma}{2\pi r_v})^2(\frac{r_v}{r})^2 \tag{2.13}$$

where p_1 and p_2 denote the dynamic pressure inside and outside the vortex core respectively, r_v is the radius of the core, Γ is the circulation about the vortex along the boundary. The wake pressure exhibits a parabola-like profile which has a minimum at the vortex center.

There is clearly a conflict between the wake pressure profile measured experimentally and that predicted by potential flow theory, despite its popularity. An alternative approach is necessary in order to effectively model the actual wake pressure effects on bubble formation at a submerged orifice.

2.5.2 Rise velocity

2.5.2.1 Initial acceleration

The initial motion of a bubble rising from a flat surface is important in the determination of wake pressure (Jameson and Kupferberg, 1967). McCann and Prince (1969) used $\dot{U}_D = 2g$ to calculate the wake pressure. Walters and Davidson (1962, 1963) gave a potential flow analysis of the initial motion of the two-dimensional and three-dimensional bubbles. They verified that a two-dimensional bubble had an initial acceleration of g, while a three-dimensional bubble had an initial acceleration of $2g$. However, whether the value of upward acceleration is applicable throughout the entire rising process is questionable, since in practice, the terminal rise velocity of the bubble is attained shortly after released.

2.5.2.2 Terminal rise velocity

In a stationary fluid of infinite extent, a bubble moving freely under the influence of gravity exhibits a specific rate of ascent when the terminal condition is attained. Under this condition, the contribution of the periodic variation in the instantaneous velocity due to bubble oscillation to the terminal velocity, U_b, is usually either sufficiently small or nullified by taking the average (Fan and Tsuchiya, 1990). All forces acting on the bubble, viz., the drag, gravitational and buoyant forces, are in equilibrium at the terminal condition. The drag force can be presented by the drag coefficient C_D. When the body is a gas bubble of negligible density, C_D is commonly defined based on an equivalent projected area, $\pi d_e^{\ 2}/4$, as given by $C_D = 4\pi d_e / 3U_b^2$ (Harmathy, 1960). In view of this definition, the behaviour of the terminal rise of the bubble is often described in terms of C_D.

It can be assumed that interfacial tension forces are ignored and flow is considered only in the neighbourhood of the nose, where the external fluid is assumed to flow as an inviscid fluid over a complete sphere or spherical of which the fluid particle forms the cap. The surface pressure distribution in the continuous fluid may then be calculated using Bernoulli's theorem. For a spherical cap, this gives (Clift, el al.,1978):

$$P_s - P_o = ga\rho(1-\cos\theta) - (9/8)\rho U_b^2 \sin^2\theta \tag{2.14}$$

where P_o is the pressure at the nose ($\theta = 0$).

The pressure distribution at the surface in the dispersed phase is assumed to be the hydrostatic pressure distribution. This will apply if $\mathrm{Re}_b = \rho_g d_e U_b / \mu_g$ is sufficiently large, e.g., of order 100 or greater, so that there is a thin interior boundary layer across which the pressure distribution is determined by the slow moving interior fluid. For a spherical cap, the pressure distribution is then

$$P_s - P_o = ga\rho_g(1-\cos\theta) \tag{2.15}$$

Equating the two expressions for ($P_s - P_o$) and solving for the terminal velocity gives

$$U_b{}^2 = \frac{8ga\Delta\rho}{9\rho}\left(\frac{1-\cos\theta}{\sin^2\theta}\right) \tag{2.16}$$

This equation cannot be satisfied over the entire spherical-cap surface, but if it is satisfied for $\theta \to 0$ to terms of order θ^2, the terminal velocity reduces to

$$U_b = \frac{2}{3}\sqrt{ga\Delta\rho/\rho} \tag{2.17}$$

which is the celebrated Davies and Taylor Equation (1950).

Collins (1966) obtained a second approximation to the velocity of a large bubble using a perturbation analysis to balance the pressure along the interface. The result, in generalized form, is

$$U_b = 0.652\sqrt{g\bar{a}\Delta\rho/\rho} \tag{2.18}$$

where $\bar{a}$ is the average radius of curvature over the surface from $\theta = 0$ to $\theta = 37.5^o$.

2.6 Bubble formation with wall effect

As discussed above, bubble formation at a submerged orifice has been investigated experimentally and theoretically in the past decades. However, nearly all of the previous studies upon bubble formation have not taken into account the dimensions of the bubble column. It has generally been assumed that the bubble column diameter was very large compared with the orifice size and that the wall effect could be neglected.

Collins (1967) carried out a study of the influence of containing walls on the velocity of spherical-cap bubbles. The work was extended by Bhaga and Weber (1981) who also investigated the influence of wall proximity on wake size, external flow fields, bubble shape, and skirt behaviour. Coutanceau and Thizon (1981) investigated the wall effect on the bubble behaviour in highly viscous liquids experimentally and theoretically. Krishna et al. (1999) also investigated the effect of the column diameter on the rise velocity of a single spherical cap bubble by introducing a scale correction factor which is a function of the ratio of the bubble diameter to the column diameter. Generally, decreasing the diameter ratio d_c / d, where d_c is column diameter and d is bubble diameter, it was found to cause bubble elongation, a decrease in terminal velocity, a marked reduction in the wake volume and the rate of fluid circulation within the wake, and a delay in the onset and waviness of skirts.

Ruzicka et al. (2001) investigated the effect of bubble column dimensions on flow regime transition. Bubble columns of three different diameters ($d_c = 0.14, 0.29, 0.40\,\mathrm{m}$) were employed in the experiment. Their study showed that decreasing column size had an adverse effect on the homogeneous regime stability and promoted flow regime transition.

2.7 Summary

Bubble formation at a submerged orifice has been extensively studied in recent decades. As discussed above, the model can be classified into two categories, i.e., spherical and non-spherical models. However, the focus of previous investigation is on those factors, such as orifice diameter, chamber volume, liquid and gas properties, gas flow rate, system pressure, liquid depth and liquid motion, and clearly there is no much studies taking into account of the wall effect. As we know, wall effect is also a factor influencing bubbling formation. Therefore, taking into account of the wall effect is necessary for further study of bubble formation.

Hooper (1986) developed a non-spherical model with the boundary integral method. Boundary integral method was very important for solving boundary values problem in PDEs. In nature, only the boundary conditions around a domain were considered, and the dimension of the potential problem was reduced by one with the formulation, which simplified the calculation. However, the model developed by Hooper (1986) was incomplete because the surface tension effect was not taken into account and there were many mathematical inconsistencies in his model. Therefore, an improved model with the boundary integral model is developed in this study.

Little work was done on bubble formation with the consideration of bubble-bubble interaction. Zhang and Tan (2000) investigated the wake effect on bubble formation quite successfully. Based on model developed by Zhang and Tan (2000), this study attempts to model bubbling regimes with the consideration of bubble-bubble interaction.

Chapter 3 Improved modeling of bubble formation with the boundary integral method

In this chapter an improved model, based on the one proposed by Hooper (1986), is developed with the inclusion of the boundary integral method and the effect of the surface tension. The boundary integral method is introduced in Section 3.1. Then, the theory and the theoretical modeling of bubble formation at a single submerged orifice are described in Section 3.2 and 3.3, respectively. The improvements over Hooper's (1986) model are presented in Section 3.4. In Section 3.5, this model is further developed in modeling the wall effect on bubble formation by the introduction of a specific system of images.

3.1 Boundary integral method

3.1.1 Introduction

Engineers and physical scientists are nowadays well conversed with methods such as finite differences or finite elements. These techniques discretize the domain of the problem under consideration into a number of elements or cells. The governing equations of the problem are then approximated over the region by functions which fully or partially satisfy the boundary conditions. These methods, together with other techniques that are applied on the domain, will be called domain methods.

The boundary integral method was initially applied to solve elastostatics problems.

Later, the method was extended to a wider area, including potential problems. The Boundary integral method is based on Green's formula that enables us to reformulate the potential problem as the solution of a Fredholm integral equation. The integral equation involves the potential and its normal derivative on the boundary of the region. This formulation has the effect of reducing the dimension of the problem by one, which has the advantage of rendering the technique computationally efficient, yet rigorous. For axisymmetric potential problems, two-dimensional integrals are reduced further to one-dimensional integrals by integrating through the polar angle. In this case the Green's functions involve complete elliptic integrals.

An early application of the integral technique to axisymmetric potential problems was by Hess and Smith (1966); their formulation was developed using a source density distribution on the body surface (indirect formulation) and using a linear surface, constant source distribution. Later, Hess (1975) improved the solution by using a curved surface and a source density variation over the surface. More recent application of this method in potential problems can be found in Blake et al. (1986, 1987), Bonnet (1995) and Power (1995).

3.1.2 Formulation

For any sufficiently smooth function, ϕ, which satisfies Laplace's equation in a domain, Ω, having piecewise smooth surface, *S*, Green's integral formula can be written as (Brebbia, 1978; Jaswon and Symm, 1977):

$$c(p)\phi(p)+\int_{s}\phi(q)\frac{\partial}{\partial n}G(p,q)dS=\int_{s}\frac{\partial}{\partial n}(\phi(q))G(p,q)dS \qquad (3.1)$$

where $p \in \Omega + S, q \in S$, $\frac{\partial}{\partial n}$ is the normal derivative outward from *S*, $G(p,q)$ is Green's function

$$G(p,q) = \frac{1}{|p-q|} \tag{3.2}$$

and

$$c(p) = \begin{cases} 4\pi, & if \quad p \in \Omega \\ 2\pi, & if \quad p \in S \end{cases} \tag{3.3}$$

Choosing *p* on *S* yields an equation for either ϕ or $\frac{\partial \phi}{\partial n}$ on *S* if the other is specified. Once both are known on *S*, Equation (3.1) can be used to generate ϕ at any point $p \in \Omega$. In axisymmetric problems, ϕ and $\frac{\partial \phi}{\partial n}$ are independent of rotational angle and integration over this variable can be performed analytically, which is discussed below.

3.1.3 Axisymmetric form of the integrate

Using cylindrical coordinates with $p = (r_0, 0, z_0)$ and $q = (r, \theta, z)$ respectively, we have

$$\frac{1}{|p-q|} = \frac{1}{\left[(r\cos\theta - r_0)^2 + (r\sin\theta)^2 + (z-z_0)^2\right]^{\frac{1}{2}}}$$

$$=\frac{1}{\left[(r+r_0)^2+(z-z_0)^2-4rr_0\cos^2\frac{\theta}{2}\right]^{\frac{1}{2}}} \tag{3.4}$$

If the surface, *S*, is parameterized by the variable, ξ,

$$\int_S \frac{1}{|p-q|}dS=\int_0^1 d\xi r(\xi)\left[(\frac{dr}{d\xi})^2+(\frac{dz}{d\xi})^2\right]^{\frac{1}{2}}\int_0^{2\pi}\frac{d\theta}{\left[(r(\xi)+r_0)^2+(z(\xi)-z_0)^2-4r(\xi)r_0\cos^2\frac{\theta}{2}\right]^{\frac{1}{2}}}$$

$$=\int_0^1\frac{d\xi r(\xi)\left[(\frac{dr}{d\xi})^2+(\frac{dz}{d\xi})^2\right]^{\frac{1}{2}}}{\left[(r(\xi)+r_0)^2+(z(\xi)-z_0)^2\right]^{\frac{1}{2}}}\int_0^{2\pi}\frac{d\theta}{\left[1-\frac{4r(\xi)r_0\cos^2\frac{\theta}{2}}{(r(\xi)+r_0)^2+(z(\xi)-z_0)^2}\right]^{\frac{1}{2}}} \tag{3.5}$$

With $k^2(\xi)=\frac{4r(\xi)r_0}{(r(\xi)+r_0)^2+(z(\xi)-z_0)^2}$, the θ integral becomes

$$\int_0^{2\pi}\frac{d\theta}{(1-k^2\cos^2\frac{\theta}{2})^{\frac{1}{2}}}=4\int_0^{\frac{\pi}{2}}\frac{d\alpha}{(1-k^2\cos^2\alpha)^{\frac{1}{2}}}$$

$$=4\int_0^{\frac{\pi}{2}}\frac{d\alpha}{(1-k^2\sin^2\alpha)^{\frac{1}{2}}}=4K(k) \tag{3.6}$$

where $K(k)$ is the complete elliptic integral of the first kind. Hence, we have

$$\int_S\frac{1}{|p-q|}dS=\int_0^1 d\xi\frac{4r(\xi)\left[(\frac{dr}{d\xi})^2+(\frac{dz}{d\xi})^2\right]^{\frac{1}{2}}K(k)}{\left[(r(\xi)+r_0)^2+(z(\xi)-z_0)^2\right]^{\frac{1}{2}}} \tag{3.7}$$

The unit normal $\hat{\underline{n}}$ can be expressed as

$$\hat{\underline{n}} = \frac{1}{\left[(\frac{dr}{d\xi})^2 + (\frac{dz}{d\xi})^2\right]^{\frac{1}{2}}}(\frac{dz}{d\xi}\cos\theta, \frac{dz}{d\xi}\sin\theta, -\frac{dr}{d\xi}) \tag{3.8}$$

We can write

$$\nabla\frac{1}{|p-q|} = \frac{-(r(\xi)\cos\theta - r_0, r(\xi)\sin\theta, z(\xi)-z_0)}{\left[(r(\xi)+r_0)^2 - 4r(\xi)r_0\cos^2\frac{\theta}{2} + (z(\xi)-z_0)^2\right]^{\frac{3}{2}}} \tag{3.9}$$

$$\int_S \frac{\partial}{\partial n}(\frac{1}{|p-q|})dS = -\left\{\begin{array}{l} \int_0^1 d\xi r(\xi)\left[r(\xi)\frac{dz}{d\xi} - (z(\xi)-z_0)\frac{dr}{d\xi})\right] \\ \int_0^{2\pi}\frac{d\theta}{\left[(r(\xi)+r_0)^2 - 4r(\xi)r_0\cos^2\frac{\theta}{2} + (z(\xi)-z_0)^2\right]^{\frac{3}{2}}} \\ -\int_0^1 d\xi r(\xi)\frac{dz}{d\xi}\int_0^{2\pi}\frac{r_0\cos\theta d\theta}{\left[(r(\xi)+r_0)^2 - 4r(\xi)r_0\cos^2\frac{\theta}{2} + (z(\xi)-z_0)^2\right]^{\frac{3}{2}}} \end{array}\right\} \tag{3.10}$$

Making the same substitution $k^2(\xi) = \frac{4r(\xi)r_0}{(r(\xi)+r_0)^2 + (z(\xi)-z_0)^2}$, we find

$$\int_S \frac{\partial}{\partial n}\left(\frac{1}{|p-q|}\right)dS = -\left\{\begin{matrix} \displaystyle\int_0^1 \frac{d\xi r(\xi)\left[r(\xi)\frac{dz}{d\xi}-(z(\xi)-z_0)\frac{dr}{d\xi})\right]}{\left[(r(\xi)+r_0)^2+(z(\xi)-z_0)^2\right]^{\frac{3}{2}}} \\ \displaystyle\int_0^{2\pi}\frac{d\theta}{\left(1-k^2\cos^2\frac{\theta}{2}\right)^{\frac{3}{2}}} - \int_0^1 d\xi r(\xi)\frac{dz}{d\xi}\frac{r_0}{\left[(r(\xi)+r_0)^2+(z(\xi)-z_0)^2\right]^{\frac{3}{2}}} \\ \displaystyle\int_0^{2\pi}\frac{\cos\theta d\theta}{\left(1-k^2\cos^2\frac{\theta}{2}\right)^{\frac{3}{2}}} \end{matrix}\right\} \tag{3.11}$$

We can write the first θ integral in Equation (3.11) as

$$\int_0^{2\pi}\frac{d\theta}{(1-k^2\cos^2\frac{\theta}{2})^{\frac{3}{2}}} = 4\int_0^{\frac{\pi}{2}}\frac{d\alpha}{(1-k^2\cos^2\alpha)^{\frac{3}{2}}}$$

$$= 4\int_0^{\frac{\pi}{2}}\frac{d\alpha}{(1-k^2\sin^2\alpha)^{\frac{3}{2}}} = 4\Pi(k,k) \tag{3.12}$$

and the second θ integral in Equation (3.11) as

$$\int_0^{2\pi}\frac{\cos\theta d\theta}{\left[1-k^2\cos^2\frac{\theta}{2}\right]^{\frac{3}{2}}} = 4\int_0^{\frac{\pi}{2}}\frac{(2\cos^2\eta-1)d\eta}{\left[1-k^2\cos^2\eta\right]^{\frac{3}{2}}}$$

$$= \frac{8}{k^2}\int_0^{\frac{\pi}{2}}\frac{(k^2\cos^2\eta-1)d\eta}{\left(1-k^2\cos^2\eta\right)^{\frac{3}{2}}} + \left(\frac{8}{k^2}-4\right)\int_0^{\frac{\pi}{2}}\frac{d\eta}{\left(1-k^2\cos^2\eta\right)^{\frac{3}{2}}}$$

$$=(\frac{8}{k^2}-4)\int_0^{\frac{\pi}{2}}\frac{d\eta}{\left(1-k^2\sin^2\eta\right)^{\frac{3}{2}}}-\frac{8}{k^2}\int_0^{\frac{\pi}{2}}\frac{d\eta}{\left(1-k^2\sin^2\frac{\eta}{2}\right)^{\frac{1}{2}}}$$

$$=(\frac{8}{k^2}-4)\Pi(k,k)-\frac{8}{k^2}K(k) \tag{3.13}$$

where $\Pi(k,k)$ is the complete elliptic integral of the third kind, which can be written in terms of the complete elliptic integral of the second kind, $E(k)$, as

$$\Pi(k,k)=\frac{E(k)}{1-k^2} \tag{3.14}$$

where $E(k)=\int_0^{\frac{\pi}{2}}(1-k^2\sin^2\alpha)^{\frac{1}{2}}d\alpha$.

Hence,

$$\int_S\frac{\partial}{\partial n}(\frac{1}{|p-q|})dS=-4\int_0^1\frac{d\xi r(\xi)}{\left[(r(\xi)+r_0)^2+(z(\xi)-z_0)^2\right]^{\frac{3}{2}}}$$

$$\left\{\left[\frac{dz}{d\xi}(r(\xi)+r_0)-\frac{dr}{d\xi}(z(\xi)-z_0)-\frac{2}{k^2(\xi)}\frac{dz}{d\xi}r_0\right]\frac{E(k)}{1-k^2(\xi)}+\frac{2}{k^2(\xi)}\frac{dz}{d\xi}r_0K(k)\right\} \tag{3.15}$$

Approximations for $K(k)$ and $E(k)$ are of the form

$$K(k)=P(x)-Q(x)\ln(x) \tag{3.16}$$

$$E(k)=R(x)-S(x)\ln(x) \tag{3.17}$$

where $x=1-k^2$

P, Q, R and *S* are tabulated polynomials that can be found in Abramowitz and Stegun (1965).

3.1.4 Approximations of the surface shape, potential and its normal derivative

To proceed with the computation, we need to choose a representation for the surface, and also for the potential and its normal derivative on the surface. To some extent, these choices can be independent, but as the movement of the surface is computed using the potential and its normal derivative, the two should be considered together. In the description that follows, a plane section through the axis of symmetry of the surface is taken, and the potential and its normal derivative will be called functions.

3.1.4.1 Linear surface-constant functions. (L-C)

The surface is replaced by a set of N linear segments S_j, with the potential and its normal derivative constant on each segment. The boundary integral equation is replaced by its collocation form using the midpoint of each linear segment:

$$2\pi\phi_i + \sum_{j=1}^{N} \phi_j \int_{S_j} \frac{\partial}{\partial n}\left(\frac{1}{|p_i - q_j|}\right) dS = \sum_{j=1}^{N} \frac{\partial}{\partial n}(\phi_j) \int_{S_j} \frac{1}{|p_i - q_j|} dS \qquad (i = 1, \cdots, N) \tag{3.18}$$

where p_i is the i$^{\text{th}}$ point chosen as collocation point, and q_j is any point on the segment S_j.

If we denote $\frac{\partial \phi}{\partial n}$ by ψ, we can write Equation (3.18) in matrix form as

$$2\pi\phi_i + \sum_{j=1}^{N} \hat{H}_{ij}\phi_j = \sum_{j=1}^{N} G_{ij}\psi_j \tag{3.19}$$

Defining $H_{ij} = \hat{H}_{ij} + 2\pi\delta_{ij}$, Equation (3.19) may be written as

$$H\Phi = G\Psi \tag{3.20}$$

3.1.4.2 Linear surface-linear functions. (L-L)

ϕ_j and ψ_j are assumed to be single valued at the end points of the linear segments which approximate the surface. If the segment is parameterized by ξ in the range (0,1), we can define

$$\left.\begin{array}{l} M_1(\xi) = 1 - \xi \\ M_2(\xi) = \xi \end{array}\right\} \tag{3.21}$$

and use the isoparametric approximations for both the surface and the functions. On segment S_j we have

$$\left.\begin{array}{l} r(\xi) = r_{j-1}M_1(\xi) + r_j M_2(\xi) \\ z(\xi) = z_{j-1}M_1(\xi) + z_j M_2(\xi) \\ \phi(\xi) = \phi_{j-1}M_1(\xi) + \phi_j M_2(\xi) \\ \psi(\xi) = \psi_{j-1}M_1(\xi) + \psi_j M_2(\xi) \end{array}\right\} \tag{3.22}$$

The collocation points are moved to the end points of each segment, yielding $N+1$ equations in the $N+1$ unknowns. The integrals on each segment can be written

$$\int_{S_j} dS \frac{\partial \phi}{\partial n} \frac{1}{|p_i - q_j|} = b_{1ij}\psi_{j-1} + b_{2ij}\psi_j \tag{3.23}$$

where

$$b_{kij} = S_j \int_0^1 d\xi M_k(\xi) \int_0^{2\pi} d\theta \frac{1}{|p_i - q(\xi,\theta)|} \tag{3.24}$$

and

$$\int_{S_j} dS\phi \frac{\partial}{\partial n}\frac{1}{|p_i - q_j|} = a_{1ij}\phi_{j-1} + a_{2ij}\phi_j \tag{3.25}$$

where

$$a_{kij} = S_j \int_0^1 d\xi M_k(\xi) \int_0^{2\pi} d\theta \frac{\partial}{\partial n}\left(\frac{1}{|p_i - q(\xi,\theta)|}\right) \tag{3.26}$$

3.1.4.3 Quadratic surface – quadratic functions. (Q-Q)

If the segment is parameterized by ξ in the range (0,1) we can define

$$\left.\begin{aligned} M_1(\xi) &= (\xi-1)(2\xi-1) \\ M_2(\xi) &= 4\xi(1-\xi) \\ M_3(\xi) &= \xi(2\xi-1) \end{aligned}\right\} \tag{3.27}$$

and use the isoparametric approximation for both the surface and the functions. On segment S_j we have

$$\left.\begin{aligned} r(\xi) &= r_{j-1}M_1(\xi) + r_j M_2(\xi) + r_{j+1}M_3(\xi) \\ z(\xi) &= z_{j-1}M_1(\xi) + z_j M_2(\xi) + z_{j+1}M_3(\xi) \\ \phi(\xi) &= \phi_{j-1}M_1(\xi) + \phi_j M_2(\xi) + \phi_{j+1}M_3(\xi) \\ \psi(\xi) &= \psi_{j-1}M_1(\xi) + \psi_j M_2(\xi) + \psi_{j+1}M_3(\xi) \end{aligned}\right\} \tag{3.28}$$

The collocation points are the endpoints and the midpoint, yielding $2N+1$ equations in the $2N+1$ unknowns. The integral on each segment can be written

$$\int_{S_j} dS \frac{\partial \phi}{\partial n}\frac{1}{|p_i - q_j|} = b_{1ij}\psi_{j-1} + b_{2ij}\psi_j + b_{3ij}\psi_{j+1} \tag{3.29}$$

where

$$b_{kij} = S_j \int_0^1 d\xi M_k(\xi) \int_0^{2\pi} d\theta \frac{1}{|p_i - q(\xi,\theta)|} \tag{3.30}$$

and

$$\int_{S_j} dS\phi \frac{\partial}{\partial n} \frac{1}{|p_i - q_j|} = a_{1ij}\phi_{j-1} + a_{2ij}\phi_j + a_{3ij}\phi_{j+1} \tag{3.31}$$

where

$$a_{kij} = S_j \int_0^1 d\xi M_k(\xi) \int_0^{2\pi} d\theta \frac{\partial}{\partial n} \left(\frac{1}{|p_i - q(\xi,\theta)|}\right) \tag{3.32}$$

3.1.5 Numerical integration

The evaluation of the elements of the matrices H and G are performed numerically. Normally Gauss Legendre Quadrature is adequate unless the collocation point p_i is within the segment S_j or is one of its endpoints, in which case the integrand is singular and must be treated specially. To remove the singularity, the singular integrals are separated into two terms by subtracting the logarithmic term. The quadrature scheme incorporating the logarithm is used to complete the integration.

Recalling $k^2(\xi) = \dfrac{4r(\xi)r_0}{(r(\xi)+r_0)^2 + (z(\xi)-z_0)^2}$, x may be written as

$$x = 1 - k^2(\xi) = \frac{(r(\xi)-r_0)^2 + (z(\xi)-z_0)^2}{(r(\xi)+r_0)^2 + (z(\xi)-z_0)^2} \tag{3.33}$$

The singularity occurs when for example $(r_o, z_o) = (r(\frac{1}{2}), z(\frac{1}{2}))$. In the vicinity of this point

$$r(\xi) = r_0 + (\xi - \frac{1}{2})\frac{dr}{d\xi} + \frac{1}{2}(\xi - \frac{1}{2})^2 \frac{d^2 r}{d\xi^2} + \cdots\cdots \tag{3.34}$$

$$z(\xi) = z_0 + (\xi - \frac{1}{2})\frac{dz}{d\xi} + \frac{1}{2}(\xi - \frac{1}{2})^2 \frac{d^2 z}{d\xi^2} + \cdots\cdots \tag{3.35}$$

Hence

$$x = 1 - k^2(\xi) \approx \frac{(\xi - \frac{1}{2})^2}{4r_0^2}[(\frac{dr}{d\xi})^2 + (\frac{dz}{d\xi})^2] \tag{3.36}$$

so that essentially $K(k)$ behaves like

$$K(k) \approx P(x) - Q(x)\ln(A(\xi - \frac{1}{2})^2) \tag{3.37}$$

This information is sufficient to allow us to deal with the singularity.

3.1.5.1 Singularity at ξ=0

This singularity occurs when p is the point $(r_o, z_o) = (r(0), z(0))$. If we write Equations (3.7) and (3.15) as

$$\int_S \frac{1}{|p-q|}dS = \int_0^1 \frac{4r(\xi)J(\xi)K(k)}{D(\xi)}d\xi \tag{3.38}$$

and

$$\int_S \frac{\partial}{\partial n}(\frac{1}{|p-q|})dS = -\int_0^1 \frac{4r(\xi)}{D^3(\xi)}$$

$$\left\{\left[\frac{dz}{d\xi}(r(\xi)+r_0)-\frac{dr}{d\xi}(z(\xi)-z_0)-\frac{2}{k^2(\xi)}\frac{dz}{d\xi}r_0\right]\frac{E(k)}{1-k^2(\xi)}+\frac{2}{k^2(\xi)}\frac{dz}{d\xi}r_0K(k)\right\}d\xi \tag{3.39}$$

where

$$J(\xi)=\left[(\frac{dr}{d\xi})^2+(\frac{dz}{d\xi})^2\right]^{\frac{1}{2}} \tag{3.40}$$

and

$$D(\xi)=\left[(r(\xi)+r_0)^2+(z(\xi)-z_0)^2\right]^{\frac{1}{2}} \tag{3.41}$$

By writing

$$\ln(x)=\ln(\frac{x}{\xi^2})+2\ln(\xi) \tag{3.42}$$

and using Equations (3.16) and (3.17), we separate out the logarithmic singularity as follows:

$$\int_S\frac{1}{|p-q|}dS=4\left\{\int_0^1\frac{r(\xi)}{D(\xi)}\left[P(x(\xi))-Q(x(\xi))\ln(\frac{x(\xi)}{\xi^2})\right]J(\xi)d\xi\right.$$

$$\left.+2\int_0^1\frac{r(\xi)}{D(\xi)}Q(x(\xi))\ln(\frac{1}{\xi})J(\xi)d\xi\right\} \tag{3.43}$$

$$\int_S\frac{\partial}{\partial n}(\frac{1}{|p-q|})dS=-\int_0^1\frac{4r(\xi)}{D(\xi)^3}\left\{\frac{R(x(\xi))-S(x(\xi))\ln(\frac{x}{\xi^2})}{1-k^2(\xi)}\left[\frac{dz}{d\xi}(r(\xi)+r_0)-\frac{dr}{d\xi}(z(\xi)-z_0)\right.\right.$$

$$-\frac{2}{k^2(\xi)}\frac{dz}{d\xi}r_0\Bigg]+\frac{2}{k^2(\xi)}\frac{dz}{d\xi}r_0\left[P(x(\xi))-Q(x(\xi))\ln(\frac{x}{\xi^2})\right]\Bigg\}d\xi$$

$$-8\int_0^1\frac{r(\xi)}{D(\xi)^3}\left\{\frac{S(x(\xi))}{1-k^2(\xi)}\left[\frac{dz}{d\xi}(r(\xi)+r_0)-\frac{dr}{d\xi}(z(\xi)-z_0)-\frac{2}{k^2(\xi)}\frac{dz}{d\xi}r_0\right]\right.$$

$$\left.+\frac{2}{k^2(\xi)}\frac{dz}{d\xi}r_0Q(x(\xi))\right\}\ln(\frac{1}{\xi})d\xi \qquad (3.44)$$

3.1.5.2 Singularity at $\xi=\frac{1}{2}$

This is the case when p is the point $(r_o,z_o)=(r(\frac{1}{2}),z(\frac{1}{2}))$. By writing

$$\ln(x)=\ln(\frac{x}{\left(2\xi-1\right)^2})+2\ln(2\xi-1) \qquad (3.45)$$

we obtain

$$\int_S\frac{1}{|p-q|}dS=4\left\{\int_0^1\frac{r(\xi)}{D(\xi)}\left[P(x(\xi))-Q(x(\xi))\ln(\frac{x(\xi)}{\left(2\xi-1\right)^2})\right]J(\xi)d\xi\right.$$

$$\left.-2\int_0^1\frac{r(\xi)}{D(\xi)}Q(x(\xi))J(\xi)\ln|2\xi-1|\,d\xi\right\} \qquad (3.46)$$

The second integral in Equation (3.46) can be split as follows

$$\int_0^1\frac{r(\xi)}{D(\xi)}Q(x(\xi))\ln|2\xi-1|\,J(\xi)d\xi=\int_0^{\frac{1}{2}}\frac{r(\xi)}{D(\xi)}Q(x(\xi))\ln\left(1-2\xi\right)J(\xi)d\xi$$

$$+\int_{\frac{1}{2}}^1\frac{r(\xi)}{D(\xi)}Q(x(\xi))\ln\left(2\xi-1\right)J(\xi)d\xi \qquad (3.47)$$

Substituting $\eta = 1-2\xi$ in the first integral in Equation (3.47) and $\eta = 2\xi - 1$ in the second integral, we obtain

$$\int_S \frac{1}{|p-q|}dS = 4\left\{\int_0^1 \frac{r(\xi)J(\xi)}{D(\xi)}\left[P(x(\xi)) - Q(x(\xi))\ln(\frac{x(\xi)}{\left(2\xi-1\right)^2})\right]d\xi\right.$$

$$\left.+\int_0^1\left[\frac{r(\frac{1-\eta}{2})Q(x(\frac{1-\eta}{2}))J(\frac{1-\eta}{2})}{D(\frac{1-\eta}{2})} + \frac{r(\frac{1+\eta}{2})Q(x(\frac{1+\eta}{2}))J(\frac{1+\eta}{2})}{D(\frac{1+\eta}{2})}\right]\ln\left(\frac{1}{\eta}\right)d\eta\right.$$

(3.48)

Using a similar technique, we obtain

$$\int_S \frac{\partial}{\partial n}(\frac{1}{|p-q|})dS = -\int_0^1 \frac{4r(\xi)}{D^3(\xi)}\left\{\frac{R(x(\xi)) - S(x(\xi))\ln(\frac{x(\xi)}{\left(2\xi-1\right)^2})}{1-k^2(\xi)}\right.$$

$$\left[\frac{dz}{d\xi}(r(\xi)+r_0) - \frac{dr}{d\xi}(z(\xi)-z_0) - \frac{2}{k^2(\xi)}\frac{dz}{d\xi}r_0\right]$$

$$\left.+\frac{2}{k^2(\xi)}\frac{dz}{d\xi}r_0\left[P(x(\xi)) - Q(x(\xi))\ln(\frac{x(\xi)}{\left(2\xi-1\right)^2})\right]\Bigg]\right\}d\xi$$

$$-\int_0^1 \frac{4r(\frac{1-\eta}{2})}{D^3(\frac{1-\eta}{2})}\left\{\frac{S(x(\frac{1-\eta}{2}))}{1-k^2(\frac{1-\eta}{2})}\left[\frac{dz}{d\xi}\left[r(\frac{1-\eta}{2}) + r_0 - \frac{2r_0}{k^2(\frac{1-\eta}{2})}\right]\right.\right.$$

$$\left.\left.-\frac{dr}{d\xi}(z(\frac{1-\eta}{2}) - z_0)\right] + \frac{2r_0}{k^2(\frac{1-\eta}{2})}\frac{dz}{d\xi}Q(x(\frac{1-\eta}{2}))\right\}\ln(\frac{1}{\eta})d\eta$$

$$-\int_0^1 \frac{4r(\frac{1+\eta}{2})}{D^3(\frac{1+\eta}{2})}\left\{\frac{S(x(\frac{1+\eta}{2}))}{1-k^2(\frac{1+\eta}{2})}\left[\frac{dz}{d\xi}\left[r(\frac{1+\eta}{2})+r_0-\frac{2r_0}{k^2(\frac{1+\eta}{2})}\right]\right.\right.$$

$$\left.\left.-\frac{dr}{d\xi}(z(\frac{1+\eta}{2})-z_0)\right]+\frac{2r_0}{k^2(\frac{1+\eta}{2})}\frac{dz}{d\xi}Q(x(\frac{1+\eta}{2}))\right\}\ln(\frac{1}{\eta})d\eta \qquad (3.49)$$

3.1.5.3 Singularity at ξ=1

This is the case when p is the point $(r_o, z_o) = (r(1), z(1))$. By writing

$$\ln(x) = \ln(\frac{x}{(1-\xi)^2}) + 2\ln(1-\xi) \qquad (3.50)$$

we obtain

$$\int_S \frac{1}{|p-q|}dS = 4\left\{\int_0^1 \frac{r(\xi)}{D(\xi)}\left[P(x(\xi)) - Q(x(\xi))\ln(\frac{x(\xi)}{1-\xi^2})\right]J(\xi)d\xi\right.$$

$$\left.+2\int_0^1 \frac{r(1-\eta)}{D(1-\eta)}Q(x(1-\eta))J(1-\eta)\ln(\frac{1}{\eta})d\eta\right\} \qquad (3.51)$$

and

$$\int_S \frac{\partial}{\partial n}(\frac{1}{|p-q|})dS = -\int_0^1 \frac{4r(\xi)}{D(\xi)^3}\left\{\frac{R(x(\xi)) - S(x(\xi))\ln(\frac{x}{(1-\xi)^2})}{1-k^2(\xi)}\left[\frac{dz}{d\xi}(r(\xi)+r_0) - \frac{dr}{d\xi}(z(\xi)-z_0)\right.\right.$$

$$\left.\left.-\frac{2}{k^2(\xi)}\frac{dz}{d\xi}r_0\right] + \frac{2}{k^2(\xi)}\frac{dz}{d\xi}r_0\left[P(x(\xi)) - Q(x(\xi))\ln(\frac{x}{(1-\xi)^2})\right]\right\}d\xi$$

$$-8\int_0^1 \frac{r(1+\eta)}{D(1+\eta)^3}\left\{\frac{S(x(1+\eta))}{1-k^2(1+\eta)}\left[\frac{dz}{d\xi}(r(\xi)+r_0)-\frac{dr}{d\xi}(z(\xi)-z_0)\right.\right.$$

$$\left.\left.-\frac{2}{k^2(1+\eta)}\frac{dz}{d\xi}r_0\right]+\frac{2}{k^2(1+\eta)}\frac{dz}{d\xi}r_0Q(x(1+\eta))\right\}\ln(\frac{1}{\eta})d\eta \tag{3.52}$$

The first integrals in Equations (3.43), (3.44), (3.48), (3.49), (3.51) and (3.52) do not contain singularity, and can be integrated by standard Gauss Legendre Quadrature shown in Appendix A.1. The other integrals contain an explicit singularity of log type, which can be integrated using the quadrature scheme shown in Appendix A.2 tabulated by Stroud and Secrest (1966) for the integral $\int_0^1 f(x)\ln(\frac{1}{x})dx$.

3.1.5.4 Point on the axis of symmetry

When the point p is on the axis of symmetry, that is $(r_o, z_o)=(0, z_0)$, the integrations can be simplified as follows:

$$\int_S \frac{1}{|p-q|}dS=\int_0^{2\pi}d\theta\int_0^1\frac{r(\xi)J(\xi)d\xi}{\left[r^2(\xi)+\left(z(\xi)-z_0\right)^2\right]^{\frac{1}{2}}}$$

$$=2\pi\int_0^1\frac{r(\xi)J(\xi)d\xi}{\left[r^2(\xi)+\left(z(\xi)-z_0\right)^2\right]^{\frac{1}{2}}} \tag{3.53}$$

and

$$\int_S \frac{\partial}{\partial n}(\frac{1}{|p-q|})dS=-2\pi\int_0^1\frac{r(\xi)(\frac{dz}{d\xi}(r(\xi)+r_0)-\frac{dr}{d\xi}(z(\xi)-z_0))}{\left[r^2(\xi)+(z(\xi)-z_0)^2\right]^{\frac{3}{2}}}d\xi \tag{3.54}$$

3.1.6 Diagonal element of the matrix *H*

After evaluating the integrals and assembling, we find the following system of equations:

$$H\phi = G\psi \tag{3.55}$$

where the diagonal elements of the matrix, *H*, include the $c(p)$ coefficients. An additional device proved helpful in increasing the numerical accuracy of the computation is to replace the diagonal elements of the matrix *H* by

$$H_{ii} = 4\pi - \sum_{j \neq i} H_{ij} \tag{3.56}$$

This property may be deduced from the fact that for the interior problem, the matrix Equation (2.55) with ϕ constant at all points on the boundary (the Dirichlet problem) should yield $\psi(=\frac{\partial\phi}{\partial n})$ zero at all points, while ψ specified at all points on the boundary (the Neumann problem) yields a solution for ϕ which contains an arbitrary additive constant. Thus for the interior problem,

$$H_{ii} = -\sum_{j \neq i} H_{ij} \tag{3.57}$$

and consideration of the definition of *H* leads immediately to Equation (2.56) for the exterior problem.

3.2 Theory of bubble formation

3.2.1 Physical system and basic assumptions

The system under consideration is shown in Fig. 3.1. Gas is pumped into a chamber at a constant flow rate, Q, and bubbles out through a small orifice with radius, r_o, into a bath of liquid.

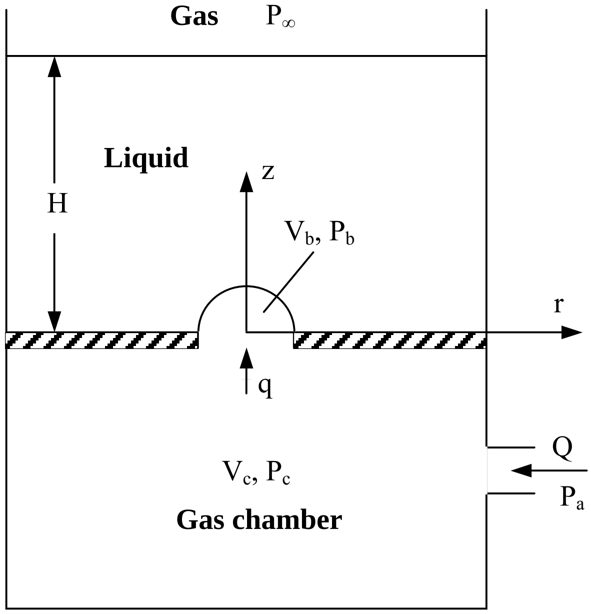

Fig. 3.1 Schematic diagram of physical system

The following basic assumptions are made:

(i). The bubble remains symmetrical about its vertical axis during the growth and is a volume of revolution around its vertical axis.

(ii). The depth of the liquid over the plate is high enough compared with the bubble diameter.

(iii). The influence of the gas and liquid viscosities are negligible.

(iv). The growth of the bubble is not affected by the presence of other bubbles.

(v). The gas is ideal and the process is adiabatic.

(vi). There is no energy exchange or mass transfer across the gas-liquid interface.

3.2.2 Equations of motion for the liquid

The viscosity of the liquid is assumed negligible and the flow is assumed to be irrotational. Therefore, a velocity potential exists, $u = \nabla\phi$, with Laplace's Equation:

$$\nabla^2\phi = 0 \tag{3.58}$$

Then, Bernoulli equation is applied between the liquid side of the bubble surface and a point in the liquid, which is chosen at a large distance from the orifice on the plane $z = 0$,

$$\frac{\partial\phi}{\partial t} + \frac{1}{2}|u|^2 + \frac{P_l}{\rho_l} + gz = \frac{P_o}{\rho_l} \tag{3.59}$$

where $P_o = P_\infty + \rho_l gH$ is the hydrostatic pressure at the orifice, P_∞ is the system pressure and H is the total height of liquid above the orifice.

It is convenient to express the dynamic boundary condition in terms of a material derivative by employing the identity

$$\frac{D\phi}{Dt} = \frac{\partial\phi}{\partial t} + |u|^2$$

Thus $\frac{D\phi}{Dt} = \frac{1}{2}|u|^2 - gz + \frac{P_o - P_l}{\rho_l}$ (3.60)

The liquid phase pressure at any point on the bubble surface, P_l, is related to the pressure within the bubble, P_b, by

$$P_l = P_b - \sigma\kappa \tag{3.61}$$

where σ is the surface tension coefficient and κ is the local curvature of the bubble surface.

3.2.3 Thermodynamic equations for the gas flow

Conservation of mass on the chamber yields

$$V_c \frac{d\rho_c}{dt} = \rho_a Q - \rho_c q \tag{3.62}$$

where ρ_a and ρ_c are the gas densities at supply and chamber conditions respectively.

From the first law of thermodynamics applied to the bubble, it follows that

$$\frac{d}{dt}(E_b) = -P_b \frac{dV_b}{dt} + \Delta Q + \Delta W \tag{3.63}$$

where E_b is the internal energy of the gas in the bubble.

Assuming the gas satisfies the ideal gas law,

$$E_b = \frac{P_b V_b}{\gamma - 1}$$

where γ is the adiabatic exponent. ΔQ is the heat added, and assuming adiabatic behavior within the bubble and chamber, it follows that

$$\Delta Q = \frac{P_c q}{\gamma - 1}$$

ΔW is the work done externally and is given by

$$\Delta W = P_c q$$

Substituting these equations into Equation (3.63) it follows that

$$V_b \frac{dP_b}{dt} + \gamma P_b \frac{dV_b}{dt} = \gamma P_c q \tag{3.64}$$

Similarly for the chamber alone, we derive

$$V_c \frac{dP_c}{dt} = \gamma P_a Q - \gamma P_c q \tag{3.65}$$

The volumetric flow through the orifice, q is, as follows:

$$q = \frac{\rho_b}{\rho_c} \frac{dV_b}{dt} \tag{3.66}$$

Substituting Equation (3.66) into Equation (3.65) and integrating the resultant equation, it follows

$$P_c(t) - P_c(0) = \frac{\gamma P_a}{V_c} Qt - \frac{\gamma P_c \rho_b}{\rho_c V_c}(V_b(t) - V_b(0)) \tag{3.67}$$

Assuming the density is constant $\rho_b = \rho_c$ and $P_a = P_c$, the above equation becomes

$$P_c(t) = P_c(0) + \frac{{c_0}^2 \rho_c}{V_c}[Qt - V_b(t) + V_b(0)] \tag{3.68}$$

where ${c_0}^2 = \gamma R_g T_c$, c_0 is the speed of sound, and is assumed to be constant.

3.2.4 Orifice equation

The orifice equation that relates the volumetric flow through the orifice, q, to the pressure difference across the orifice is as follows:

$$q = \frac{dV_b}{dt} = k(\pi {r_0}^2)\sqrt{\frac{P_c - P_b}{\rho_c}} \tag{3.69}$$

where k is the orifice coefficient.

Equation (3.69) becomes

$$P_b = P_c - \frac{\rho_c}{k^2(\pi r_o)^2}(\frac{dV_b}{dt})^2 \tag{3.70}$$

From Equation (3.68) and Equation (3.70), we obtain

$$P_b(t) = P_c(0) + \frac{{c_o}^2 \rho_c}{V_c}[Qt - V_b(t) + V_b(0)] - \frac{\rho_c}{k^2(\pi {r_o}^2)^2}(\frac{dV_b}{dt})^2 \tag{3.71}$$

3.2.5 Curvature of bubble surface

In the absence of liquid cross-flow across the orifice, the bubble can be assumed to be axisymmetric, and we use a number of two-dimensional (r; z) elements to represent it. According to the Young-Laplace Equation, the local curvature of a certain point on the surface is defined as

$$\kappa = \frac{1}{R_1} + \frac{1}{R_2} \tag{3.72}$$

where R_1 and R_2 are principal radii of curvature, on vertical and horizontal planes, respectively. From analytical geometry, the principal radii of curvature may be represented by the following equations (Gray, 1998):

$$\frac{1}{R_1} = \frac{z''}{\left(1+z'^2\right)^{3/2}} \quad \text{and} \quad \frac{1}{R_2} = \frac{z'}{r\left(1+z'^2\right)^{1/2}} \tag{3.73}$$

where r and z represent horizontal and vertical positions on the profile, and z' and z'' denote the first and second derivatives with respect to r which can be obtained through curve fitting written in the form $z = z(r)$ along the bubble surface.

3.2.6 Volumetric growth rate of bubble

With the values of the normal velocity, $\frac{\partial \phi}{\partial n}$, which are discussed in section 3.3.2.1, at a number of points on bubble surface, S_b, the bubble volumetric growth rate can be obtained by the integral

$$\frac{dV_b}{dt} = 2\pi \int_{S_b} \frac{\partial \phi}{\partial n} r ds \tag{3.74}$$

3.3 Numerical solution strategy

3.3.1 Initial conditions

We assume that initially the bubble surface is a hemisphere of radius equal to the orifice radius. Gas is pumped into the system at a volumetric flow rate, Q, and the initial normal velocity of the bubble is taken to be

$$U_i = \frac{Q}{2\pi {r_o}^2} \tag{3.75}$$

where r_o is the radius of the orifice.

Thus the initial value of ϕ is taken to be:

$\phi = -\frac{Q}{2\pi r_o}$ at the bubble surface when t=0

$\phi = 0$ at $z \to \infty$ when t=0

Initially, if we assume $q = Q$, it follows that

$$P_b(0) = P_c(0) - \frac{Q^2 \rho_c}{k^2 (\pi {r_o}^2)^2} \tag{3.76}$$

From Equations (3.71) and (3.76), we obtain

$$P_b(t) = P_b(0) + \frac{{c_o}^2 \rho_c}{V_c}[Qt - V_b(t) + V_b(0)] + \frac{\rho_c}{k^2 (\pi {r_o}^2)^2}[Q^2 - (\frac{dV_b}{dt})^2] \tag{3.77}$$

The initial value of the bubble pressure, *P_b*, is assumed to be the sum of the hydrostatic pressure at the orifice and the pressure due to surface tension,

$$P_b(0) = P_o + \frac{2\sigma}{r_o} \tag{3.78}$$

With Equations (3.61), (3.77) and (3.78), Equation (3.60) can be rewritten as:

$$\frac{D\phi_i}{Dt} = \frac{1}{2}|u_i|^2 - gz_i + \frac{\sigma}{\rho_l}(\kappa - \frac{2}{r_o}) - \frac{c_o{}^2\rho_c}{V_c\rho_l}[Qt - V_b(t) + V_b(0)] + \frac{\rho_c}{k^2(\pi r_o{}^2)^2\rho_l}[(\frac{dV_b}{dt})^2 - Q^2]$$

(3.79)

3.3.2 Normal velocity with boundary integral method

How to calculate $\frac{\partial\phi}{\partial n}$ at the bubble surface is crucial, and the detail of the boundary integral method used to get $\frac{\partial\phi}{\partial n}$ is discussed in Section 3.1.

As the bubble is assumed to be axisymmetric, a cylindrical coordinate system is used. Two-dimensional integrals are reduced further to one dimension by integrating through the polar angle.

In order to solve the problem of the two-dimensional bubble computationally, firstly the surface is represented by n points which divide the surface into $(n-1)$ elements, each being the frustum of a cone. Then an isoparametric linear approximation is used for the surface shape, potential and its normal derivative. Thus on each segment, $S_j\,(j = 1,\cdots,n-1)$, we have

$$\begin{aligned}
r(\xi) &= r_j(1-\xi) + r_{j+1}\xi \\
z(\xi) &= z_j(1-\xi) + z_{j+1}\xi \\
\phi(\xi) &= \phi_j(1-\xi) + \phi_{j+1}\xi \\
\frac{\partial\phi}{\partial n}(\xi) &= \frac{\partial\phi_j}{\partial n}(1-\xi) + \frac{\partial\phi_{j+1}}{\partial n}\xi
\end{aligned} \qquad (3.80)$$

where the parameter ξ is in the range (0, 1).

Collocation points are chosen to be these n points on the surface, yielding n equations with the following form:

$$2\pi\phi_i + \sum_{j=1}^{n-1}\int_{S_j}[(1-\xi)\phi_j + \xi\phi_{j+1}]\frac{\partial}{\partial n}G(p_i,q_j)dS = \sum_{j=1}^{n-1}\int_{S_j}[(1-\xi)\frac{\partial\phi_j}{\partial n} + \xi\frac{\partial\phi_{j+1}}{\partial n}]G(p_i,q_j)ds$$

$$(i=1,\cdots,n) \tag{3.81}$$

where p_i is the i^{th} point chosen as collocation point with cylindrical coordinates $p_i=(r_i,z_i,0)$ and q_j is any point on the segment S_j with cylindrical coordinates $q_j=(r(\xi),z(\xi),\theta)$.

After assembly, the set of equations has the following matrix structure:

$$A\phi = B\frac{\partial\phi}{\partial n} \tag{3.82}$$

where A and B are $n\times n$ matrices with the following values of items a_{ij} and b_{ij}:

$$a_{ij} = 2\pi\delta_{ij} + \int_{S_j}(1-\xi)\frac{\partial}{\partial n}G(p_i,q_j)ds + \int_{S_{j-1}}\xi\frac{\partial}{\partial n}G(p_i,q_{j-1})ds$$

$$b_{ij} = \int_{S_j}(1-\xi)G(p_i,q_j)ds + \int_{S_{j-1}}\xi G(p_i,q_{j-1})ds \tag{3.83}$$

ϕ and $\frac{\partial\phi}{\partial n}$ are vectors as follows

$$\phi = [\phi_1,\phi_2,\cdots\cdots,\phi_n]^T$$

$$\frac{\partial\phi}{\partial n} = [\frac{\partial\phi_1}{\partial n},\frac{\partial\phi_2}{\partial n},\cdots\cdots,\frac{\partial\phi_n}{\partial n}]^T$$

With the values of ϕ known at each of the collocation points, the matrix Equation

(3.82) is solved by standard Gaussian Elimination to yield the normal velocities $\frac{\partial \phi}{\partial n}$ at these collocation points.

3.3.3 System of images

A key boundary condition that needs to be specified is the zero-normal-velocity condition on the rigid boundary,

$$\frac{\partial \phi}{\partial n} = 0 \quad \text{on} \quad z = 0$$

To satisfy this case of a rigid boundary, an image system is introduced as shown in Fig. 3.2. Whence Green's function in Equation (3.81) is replaced by

$$G(p,q) = \frac{1}{|p-q|} + \frac{1}{|p-q'|} \tag{3.84}$$

where q' is the image of q in the z = 0 plane.

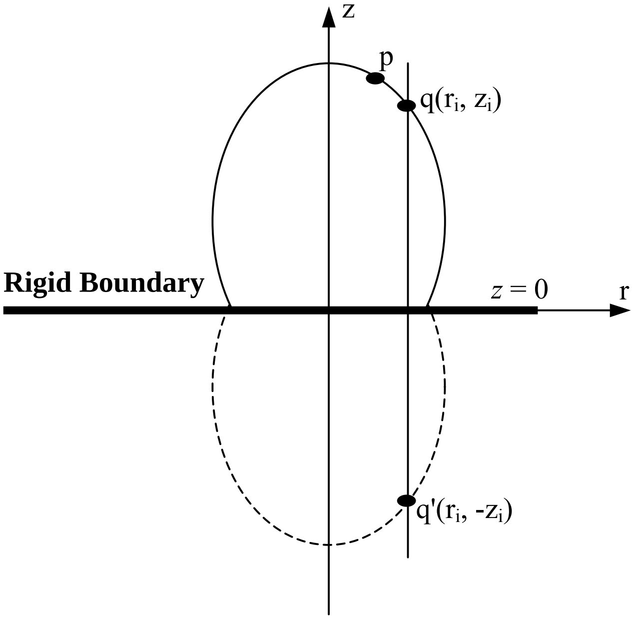

Fig. 3.2. System of images

3.3.4 Tangential velocity with cubic spline interpolation

To complete the specification of the surface velocity at a given point, the tangential component must be approximated from the given values of the velocity potential $\phi(p_i)$ where $p_i \in S_b$. We choose the point at the top of the bubble on the axis of symmetry as the beginning point and arc length as the parametric variable of the velocity potential. Then, cubic spline interpolation is used to construct an approximating function $\phi = \phi(s)$ which is used to compute the derivative, ϕ, with respect to *s*.

Two boundary conditions are needed in the calculation. $\frac{\partial \phi}{\partial s} = 0$ at the top of the bubble because of axisymmetry. For the end point, *C*, it belongs not only to the bubble surface, but also to the rigid boundary of the plate. Since the interface cannot completely detach from the plate and there is no flow through the plate, *C* can only move along the plate so that the boundary condition $\frac{\partial \phi}{\partial n} = 0$ on $z = 0$, with *n* the normal to the plate, must apply to it. But since it also belongs to the bubble surface, for consistency, the component of the velocity tangential and normal to the bubble surface at *C* must also add up to a zero velocity in the direction normal to plate, so that (Fig. 3.3)

$$\frac{\partial \phi}{\partial s}|_c \sin\theta_c - \frac{\partial \phi}{\partial n}|_c \cos\theta_c = 0 \qquad (3.85)$$

where θ_c can be identified as the dynamic three-phase contact angle (Liow and Gray, 1988).

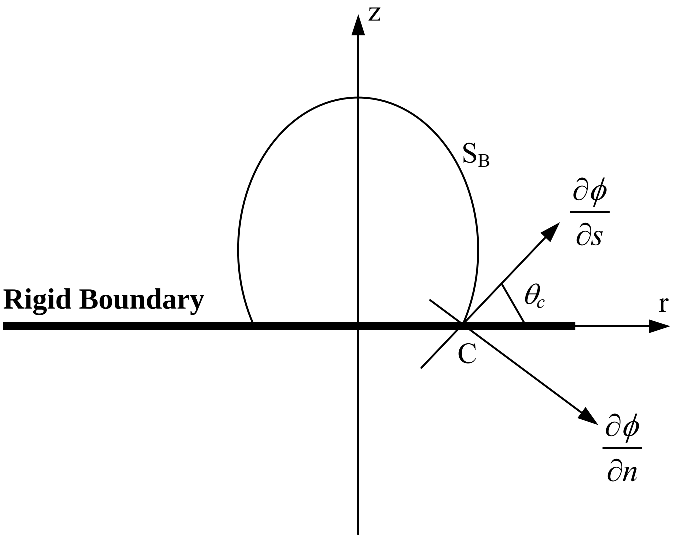

Fig. 3.3. Illustration of the end point with contact angle

3.3.5 Non-dimensionalisation

We use the initial velocity, U_i, as a reference velocity and the orifice radius, r_o, as the reference length. Time is rendered dimensionless with respect to the fundamental timescale, r_o / U_i. Thus, the initial condition is that the bubble is a hemisphere with unit dimensionless radius and unit dimensionless velocity.

With respect to velocity potential, the initial conditions become

$\hat{\phi} = -1$ at bubble surface when t=0

$\hat{\phi} = 0$ at $z \to \infty$ when t=0

In developing the numerical solution of these equations, it is convenient to scale all terms to obtain dimensionless equations. We choose the Froude number, *Fr*, Weber number, *We*, Volume number, *Vn*, and Orifice number, *On*, to represent the physical and geometrical scales in our bubbling system, where:

$$Fr = \frac{U_i^2}{g r_o}$$

$$We = \frac{\rho_l U_i^2 r_o}{\sigma}$$

$$Vn = \frac{\rho_c c_o^2 r_o^3}{\rho_l V_c U_i^2}$$

$$On = \frac{\rho_c}{\rho_l \pi^2 k^2}$$

Thus Equation (3.79) becomes

$$\frac{D\hat{\phi}_i}{D\tau} = \frac{1}{2}\left|\hat{u}_i\right|^2 - \frac{1}{Fr}\hat{z}_i + \frac{1}{We}(\hat{\kappa} - 2) - Vn\left[\hat{Q}\tau - \hat{V}_b(\tau) + \hat{V}_b(0)\right] + O_n\left[\left(\frac{d\hat{V}_b}{d\tau}\right)^2 - \hat{Q}^2\right]$$

(3.86)

where τ is the dimensionless unit of time and ^ denotes a dimensionless variable.

The non-dimensionalisation is also applied to other calculations.

3.3.6 Time stepping and computational procedure

To update the position of the bubble and the velocity potential at its surface through time, an iterative trapezium rule, Euler's Method, is used

$$\hat{r}_i(\tau + \Delta\tau) = \hat{r}_i(\tau) + \hat{u}_{i,r}(\tau)\Delta\tau$$

$$\hat{z}_i(\tau + \Delta\tau) = \hat{z}_i(\tau) + \hat{u}_{i,z}(\tau)\Delta\tau$$

$$\hat{\phi}_i(\tau+\Delta\tau)=\hat{\phi}_i(\tau)+\frac{D\hat{\phi}_i(\tau)}{D\tau}\Delta\tau \tag{3.87}$$

where $\hat{u}_{i,r}$ and $\hat{u}_{i,z}$ are radial velocity and axial velocity at i^{th} point of the bubble surface respectively.

When one of the radial distances of the points (except the top point) on the bubble surface becomes zero, the detachment of the bubble happens and the computational procedure is ended.

The procedure is summarized in the following steps:

(i) Initialize all variables.

(ii) Increment time by Δt.

(iii) The field Equation (3.58) is solved using the Boundary Integral Method. Using the Green's formula approach the normal velocity is found directly by solving Equation (3.82) numerically. The tangential velocity is solved by cubic spline interpolation.

(iv) Use the velocities found in (iii) to update the position of the surfaces.

(v) Use the dynamic condition, Equation (3.86), to update the surface potentials.

(vi) Go back to (ii) and repeat until detachment happens.

3.4 Improvements over Hooper's (1986) model

The proposed model is generally based on Hooper's (1986) approach to modeling bubble formation using the boundary integral method. However, we have made several significant improvements and developments in our model.

Firstly, the selection of dimensionless numbers representing the physical and dimensional parameters allows the natural and *a priori* formulation of the dimensionless equation of potential flow (Equation 3.86), instead of relying on the questionable iterative method to define length and time scales proposed by Hooper (1986).

Secondly, Hooper (1986) does not explicitly account for the curvature of the bubble surface in relating P_l to P_b. Instead, it was merely stated that due to numerical instabilities, the surface tension number was always set to zero, thereby ignoring the effect of σ altogether and rendering P_l equal to P_b in all the solutions.

Thirdly, the use of a realistic boundary condition (Equation 3.85) at the point where the bubble surface meets the orifice plate allows us to relate the bubble shape to the dynamic three-phase (i.e. gas-liquid-solid) contact angle, θ_c, instead of the arbitrary shape criterion introduced in Hooper's (1986) work.

3.5 Modeling the wall effect on bubble formation

As discussed in Section 2.6, the effect of the bubble column wall on bubble formation has rarely been taken into account by most of the researchers. It has generally been assumed that the bubble column was very large compared with the orifice size and that the wall effect could be neglected. This assumption is generally valid when the container diameter is very large with respect to the bubble diameter. However, as the column to orifice diameter ratio is reduced, the bubble behavior is modified: the influence of liquid circulation becomes relatively greater and the bubble shape becomes longer and, in a limiting case, resembles slugs in vertical pipelines. With the consideration of the wall effect, the boundary integral model discussed above is further developed by the introduction of a system of images.

3.5.1 System of images

To satisfy the no-flux boundary condition on the impermeable column wall where the normal velocity is zero, a specific image system is introduced to account for the wall effect as shown in Fig. 3.4. For this formulation, Green's function in Equation (3.84) is further modified as:

$$G(p,q)=\frac{1}{|p-q|}+\frac{1}{|p-q'|}+\frac{1}{|p-q''|}+\frac{1}{|p-q'''|}+\frac{1}{|p-q''''|}+\frac{1}{|p-q'''''|} \tag{3.88}$$

where q', q'', q''', q'''' and q''''' are the images of q as shown in Fig. 3.4.

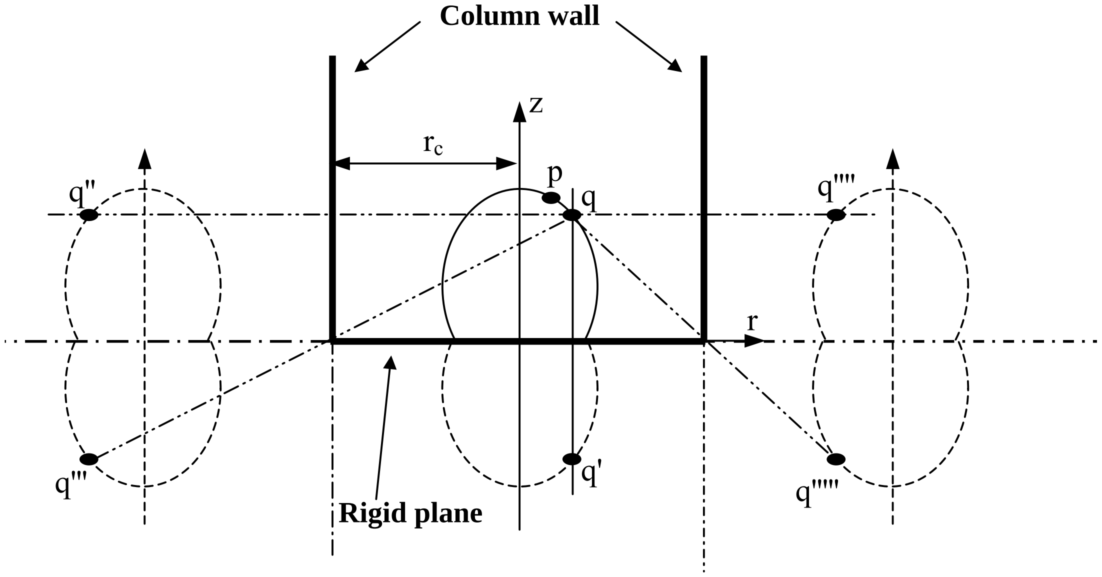

Fig. 3.4 Specific image system.

3.5.2 Bubbling frequency

One cycle of bubble formation consists of formation and waiting processes. Thus the bubble formation period of one cycle is equal to the sum of t_f and t_w, and the frequency of bubble formation, f, which corresponds to the number of bubbles formed per unit time, is the inverse number of the period as follows:

$$f = \frac{1}{t_f + t_w} \tag{3.89}$$

The formation time, t_f, can be calculated with the model and the waiting time, t_w, can be calculated from the fact that after bubble detachment, the pressure in the chamber will accumulate due to the continuous input of gas but no outflow of gas from the chamber. The chamber pressure expression during the waiting time is derived from Equation (3.65) under the condition $q = 0$:

$$\frac{dP_c}{dt} = \frac{\gamma}{V_c} P_c Q \tag{3.90}$$

and t_f can be obtained from above equation.

Fig. 3.5 shows a typical chamber pressure fluctuation during one bubble formation cycle.

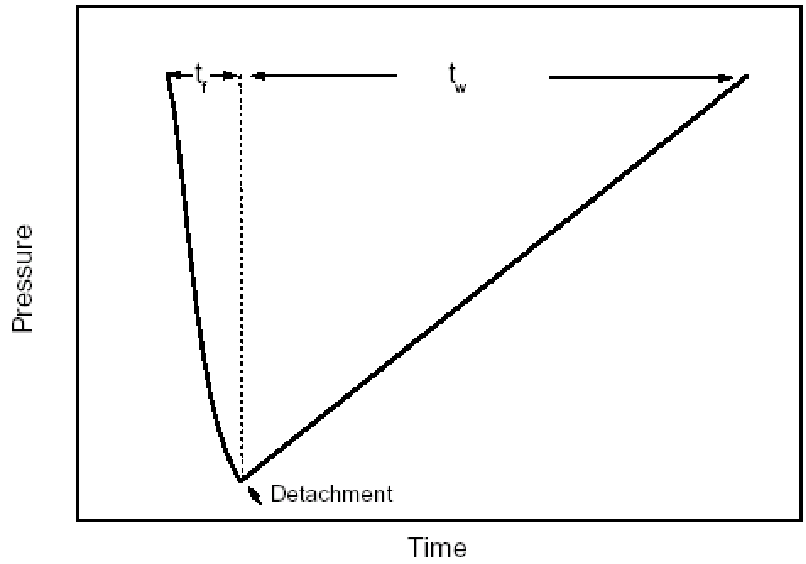

Fig. 3.5 Typical gas chamber pressure vs. time for a bubble formation period

Chapter 4 Experimental

This chapter gives detailed descriptions of the experimental setup and the procedures used for the investigation of the wall effect on bubble formation at a submerged orifice. Section 4.1 illustrates the apparatus used in the study, which includes bubble column, gas chamber, plate insert and gas supply system. Measurement techniques, consisting of dynamic pressure transducer and high-speed video camera, are introduced in Section 4.2. Finally, the experimental conditions and procedures are summarized in Section 4.3.

4.1 Experimental apparatus

Fig. 4.1 shows a schematic diagram of the experimental apparatus. It consisted of a cylinder as the bubble column, a plate insert and a cylinder as the gas chamber. Purified air from the compressed gas cylinder was introduced into the gas chamber. Air flow rate was controlled by means of three gas flow meters with various ranges. A high-speed video camera was used to visually observe bubble formation and a pressure transducer was used to record pressure fluctuations in the gas chamber.

4.1.1 Bubble columns and gas chamber

The bubble column, designed conveniently for visual and photographical observations, was located above the plate insert and gas chamber. The cylindrical bubble column was made of 5 mm thickness Plexiglas®. To investigate the effect of column wall on bubble formation, three sizes of column, $I.D.\phi$ 30mm×470mm, $I.D.\phi$ 50mm×470mm and *I.D.*ϕ 100mm×470mm, were used. The column was open to atmosphere at the top and from which water was introduced into the column so that various liquid depths, *H*, could be achieved. A drain valve was designed near the bottom of the column to remove the liquid.

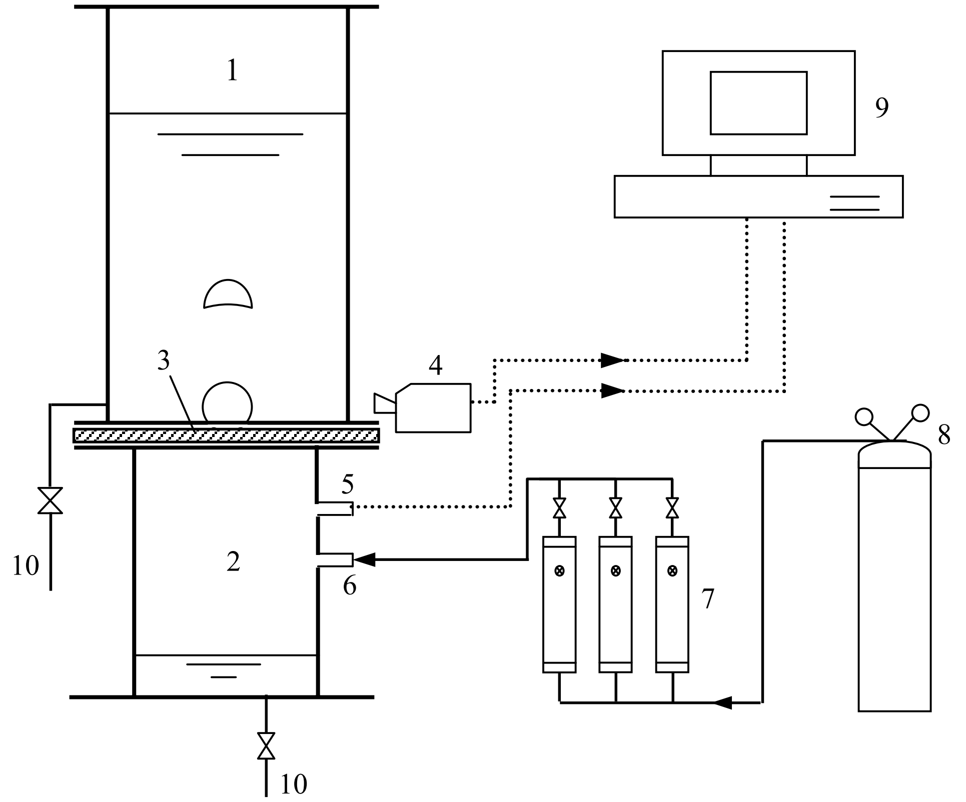

Fig. 4.1 Experimental setup (1.Bubble column, 2.Gas chamber, 3.Plate insert, 4.High-speed camera, 5.Pressure transducer, 6.Gas inlet, 7.Gas flow meters, 8.Gas cylinder, 9.Read-out computer, 10.Drain)

The gas chamber, also made of 5 mm thickness Plexiglas®, was located right below the plate insert. Two cylindrical gas chambers with different dimensions, *I.D.*ϕ 60mm×300mm and *I.D.*ϕ 100mm×300mm, were utilized during the experiment in order to achieve different gas chamber volumes. The volume of the gas chamber could be varied from 260 cm^3 to 2000 cm^3 by filling it partially with water without water entering the transducer or gas injection lines. The pressure transducer port and gas inlet port were located at the upper part of the gas chamber at an angle of 90 degrees to each other. A drain valve was designed at the bottom of the gas chamber to remove the liquid.

4.1.2 Plate insert

An interchangeable plate insert allowed various sizes of orifice to be investigated. It comprised an orifice plug and a base flange as shown in Fig. 4.2 and Fig. 4.3 respectively, both of which were made of Perspex.

The orifice plug consisted of two parts, base and raised section. The base of the orifice plug, with diameter 81 mm and height 12 mm, had a central opening with diameter 28 mm. The raised section, with diameter 30 mm and height 21 mm, was hollow with thickness 1mm for the around and top sides and had an orifice in the center of the topside. The size of the orifice plug remained constant throughout the experiment, however the orifice varied in diameter, 1.6 mm, 2.0 mm and 2.4 mm respectively. With the design, the point of injection occurred in a relatively quiescent region so that the influence of bulk liquid circulation effects on bubble formation could be reduced. Moreover, the raised section enabled bubble formation at the orifice to be clearly captured with a high-speed camera.

The base flange, with diameter 270 mm and height 12 mm, had a central opening with diameter 81 mm onto which the orifice plug with specific orifice was inserted. After the orifice plug was inserted, the base flange was bolted between the upper bubble column and the lower gas chamber.

In order to achieve an airtight seal, all gaps, such as between the column and the plate insert, and between the plate insert and the gas chamber, were sealed tightly by using O-rings.

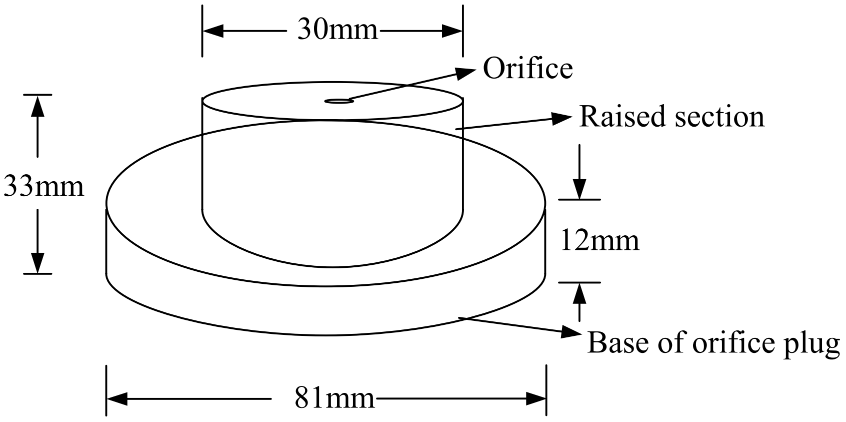

Fig. 4.2 Orifice plug

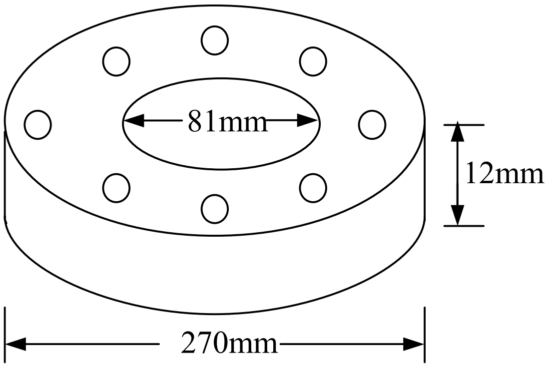

Fig. 4.3 Base flange

4.1.3 Gas supply system

The gas supply system consisted of a high-pressure gas cylinder, pressure regulator, rotameters and other ancillary apparatus. Purified air from the compressed gas cylinder was introduced into the gas chamber. Three rotameters (Tokyo Keiso, Japan), covering the range of flow rates 0.08-0.83 cm^3/s, 0.5-5.0 cm^3/s and 3.3-33 cm^3/s respectively, were connected in parallel to control the air flowrate into the gas chamber. In order to ensure a smooth flow, the upstream pressure maintained at a value was higher than the chamber pressure. Therefore, the gas flow rates indicated by the rotameters should be converted to standard conditions as shown in Appendix B. The gas temperature was between 20 and $25^o C$.

4.2 Measurement techniques

4.2.1 Dynamic pressure transducer

Pressure fluctuations during bubble formation in the gas chamber were recorded by Microphone ICP® Pressure Sensor (Model 106B50, PCB PIEZOTRONICS). The series 106B microphones feature high-sensitivity (output: 72.9 mv/KPa), acceleration-compensated quartz pressure elements coupled to built-in integrated circuit impedance converting amplifiers. It was designed to measure pressure perturbations in air or in fluids in severe conditions.

The sketch of the pressure transducer is shown in Fig. 4.4. The pressure transducer was mounted flush to the chamber wall, and was powered by a signal conditioner (model 482A06, single channel, PIEZOTRONICS). The analog output from the signal conditioner was fed into the computer through a 12-bit ADC (analog digital converter, PICO). The ADC-12 converter was connected to the printer port of computer. Its measurement range was between 0 and 5 Volt. Collected data was analyzed by a driving software installed in the computer. Bubbling frequencies were determined by Fast Fourier Transform (FFT) analysis of the pressure-time series data. Assuming that the size of the bubble is uniform, a single bubble volume was calculated by dividing gas flow rate by the obtained bubbling frequency.

An important consideration in positioning the pressure tapping in the chamber was its placement relative to the gas injection port. In order to minimize the effects of the supply air blowing directly into the transducer, the pressure tapping was placed at 90 degrees to the injection port.

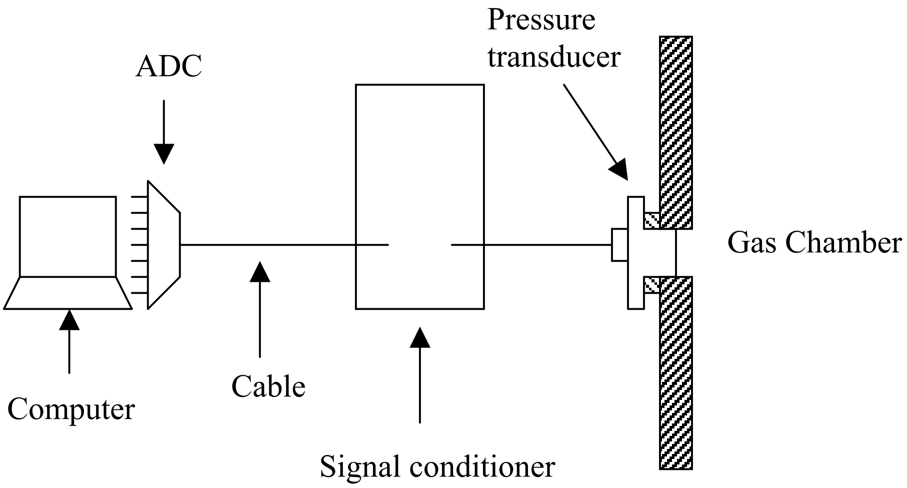

Fig. 4.4 Pressure Transducer System

4.2.2 High-speed video camera

High-speed images were recorded during the experiments in order to verify the link between pressure transducer fluctuations and actual physical dynamics of the system. The FASTCAM-PCI High-Speed Video Camera System (PHOTRON$_{\mathrm{TM}}$) was employed for this purpose (Fig. 4.5). It comprised of a FASTCAM-PCI camera head, a zoom lens and a control PCI board connecting with the computer. The key features of the system are 500 full frames recorded at 512×480 resolutions and with a maximum recording rate of 10,000 frames per second. Motion analysis software, named MotionPlus, was installed in the computer to create image files.

The camera was placed at the same vertical level as the injection orifice and with 1.0 m distances from the bubble column. Two 1000W fan-cooled halogen lamps angled 45 degrees to the front side of the bubble column illuminated the experimental rig, with a white board reflector placed behind the bubble column to get balanced lighting during picture recording.

The shutter speed was used to freeze the motion so as to reduce motion blur. By controlling the camera shutter speed and exposure time, get a sharp image was obtained. The operation of the high speed camera equipment was straightforward and film loading, lens focusing and other adjustments of the equipment was verified prior to each run according to the manufacturer's instructions.

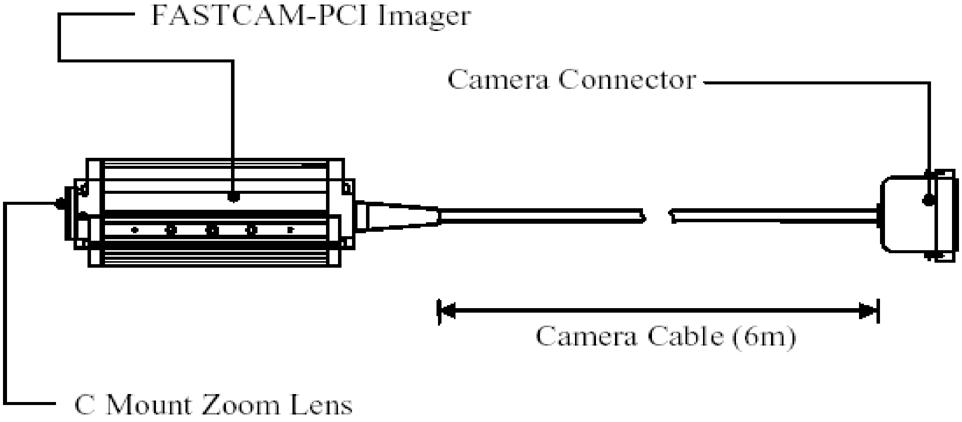

Fig. 4.5 High-speed Video Camera

4.3 Experimental conditions and procedures

4.3.1 Experimental conditions

The physical properties of air and water are shown in Table 4.1. Table 4.2 lists the important parameters for bubble formation, including gas flow rate, orifice diameter, column size, liquid height and gas chamber volume, etc. The operating conditions were selected to ensure that the independent influence of parameters was being investigated as opposed to their combined influence. The primary objectives for the experimental work were obtaining the bubbling frequency and bubble volumes under a specified range of operating conditions. The physical experimental results were utilized to compare with the predictions of numerical model for validation purposes.

Table 4.1 Physical properties of air and water at standard conditions (20°C, 1 atm)

	Filtered Tap Water	Purified Air
Density (ρ)	998.9 kg/m^3	1.3 kg/m^3
Viscosity (μ)	1.0×10^{-3} Pa · S	1.8×10^{-5} Pa · S
Surface Tension (σ)	7.2×10^{-2} N/m	

Table 4.2 Experimental conditions

System	Air-Water
Orifice Diameter	1.6 mm, 2.0 mm, 2.4 mm
Column Diameter	30 mm, 50 mm, 100 mm
Gas flow rate into the chamber	0.512 ~ 5.122 cm^3/s
Chamber Volume	430 ~ 1000 cm^3
Liquid Depth	30 cm
Air/Water Temperature	20.0 ~ 25.0 ℃
Atmosphere Pressure	742.0 mmHg
Over Pressure of Air Source Over Chamber Pressure (Gauge)	0.05 bar

4.3.2 Experimental procedures

For each run of experiment, the procedures was as follows:

1. Insert the orifice plug with specified diameter into the base flange. Choose one specific bubble column and attach the bubble column, plate insert and gas chamber together by tightening the bolts. Before locating the pressure transducer on the port and connecting the gas pipe with the gas chamber, introduce water into the gas chamber to achieve a specified gas chamber volume.

2. Determine if there is leakage of air after tightening the bolts. Open the gas valve of the compressed air cylinder and regulate the outlet pressure (i.e. rotameter inlet pressure, 0.05 bar overpressure (gauge)). Then the air is fed into the gas chamber and fed into the bubble column through the orifice plate.

3. Introduce the tap water into the bubble column through a rubber hose with a predominant gas flow rate. When the water liquid level in the bubble column is about to approach to the value to be set, change gas flow rate into a lower value so that the liquid surface fluctuation is reduced to get an accurate reading of the liquid. If the gas flow rate is too small, weeping is significant and results in an unstable liquid level.

4. Adjust the gas flow rate after the desired liquid level is obtained and the experimental data is collected for the specified operating conditions. Care should be taken to ensure that the air pressure and gas flow rate are stable during the experimental run.

5. Activate the high-speed video recorder to record bubble behavior. Pressure

fluctuation in the gas chamber is also recorded at the same time and bubble frequency and fluctuation amplitude are obtained.

4.3.3 Reproducibility of experimental data

In order to confirm the reliability of experimental data, most of the experiments were done in triplicate and three runs of experimental data were compared for each condition. The experiments were repeated after several days rather than immediately. Fig. 4.6 shows the bubble frequency reproducibility of experimental data at $d_c = 100\,\text{mm}$ and $d_o = 2.4\,\text{mm}$ for gas chamber volume $V_c = 430\,\text{cm}^3$. The variability was less than 10%, and generally within the expected experimental uncertainty.

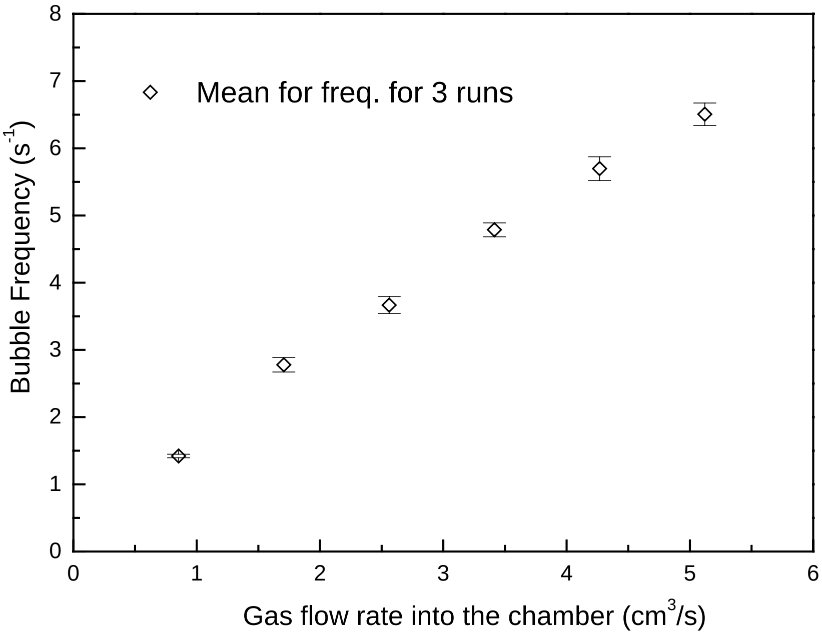

Fig. 4.6 Reproducibility of bubble frequency at d_c =100 mm, d_o = 2.4 mm, V_c = 430 cm^3

Chapter 5 Results and discussion

In this chapter, first the boundary integral model is validated for single bubbling in Section 5.1. Section 5.2 describes the wall effect on bubbling regimes and bubbling frequency, experimentally and theoretically. Finally, the discussion for this study is presented in Section 5.3.

5.1 Validation of boundary integral model for single bubbling

The boundary integral model is verified through the comparison of experimental data with theoretical predictions for single bubbling.

For the air-water system of Kupferberg and Jameson (1969) with the following experimental conditions:

Gas flow rate Q = 16.7 cm^3/s

Radius of the orifice r_o = 0.16 cm

Chamber volume V_c = 2250 cm^3

Height of the liquid H =15.24 cm

The instantaneous shapes and bubble growth curves and chamber pressure fluctuation are shown in Fig. 5.1. The bubble shapes obtained by the present model are shown in Fig. 5.1(a), which agrees approximately with the experimental shapes shown in Fig. 5.1(b) obtained from the original photographs in Kupferberg and Jameson (1969). Fig. 5.1(c) compares the simulated bubble growth curve and chamber pressure fluctuation with the experimental data.

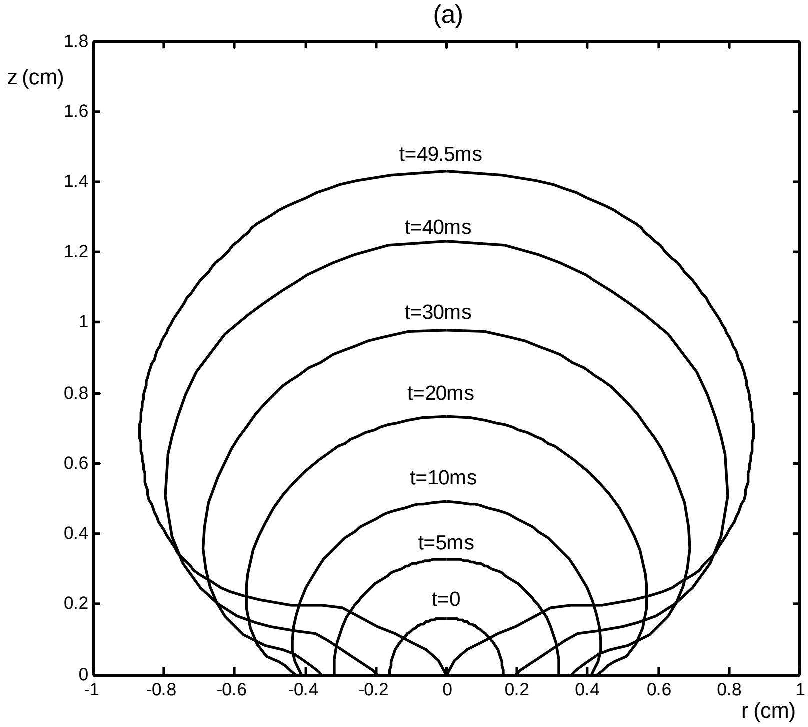
(a)
z (cm)
r (cm)
t=49.5ms
t=40ms
t=30ms
t=20ms
t=10ms
t=5ms
t=0
0
0.2
0.4
0.6
0.8
1
1.2
1.4
1.6
1.8
-1
-0.8
-0.6
-0.4
-0.2
0
0.2
0.4
0.6
0.8
1

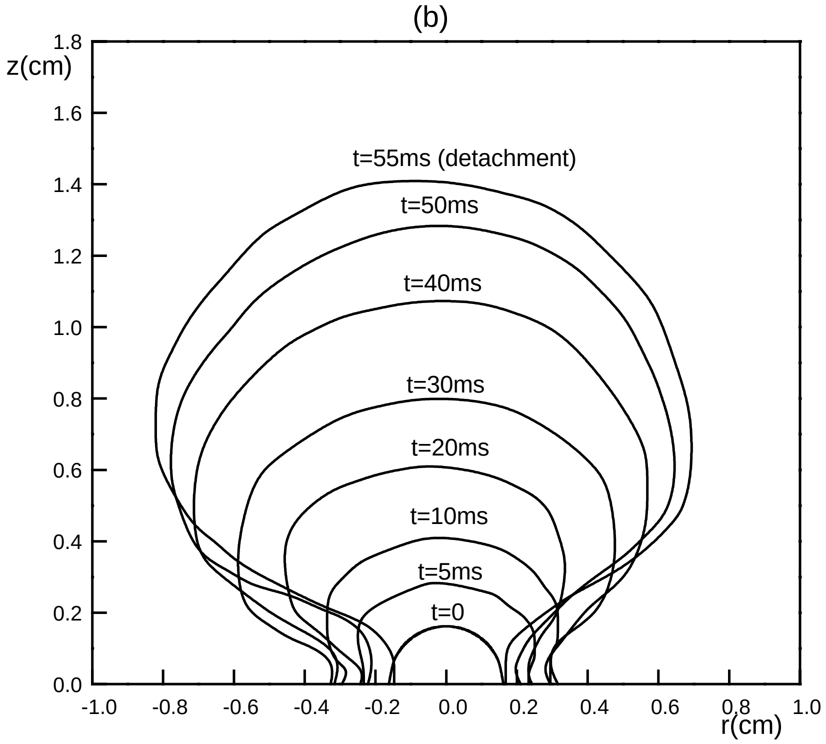
(b)
z(cm)
r(cm)
t=55ms (detachment)
t=50ms
t=40ms
t=30ms
t=20ms
t=10ms
t=5ms
t=0
0.0
0.2
0.4
0.6
0.8
1.0
1.2
1.4
1.6
1.8
-1.0
-0.8
-0.6
-0.4
-0.2
0.0
0.2
0.4
0.6
0.8
1.0

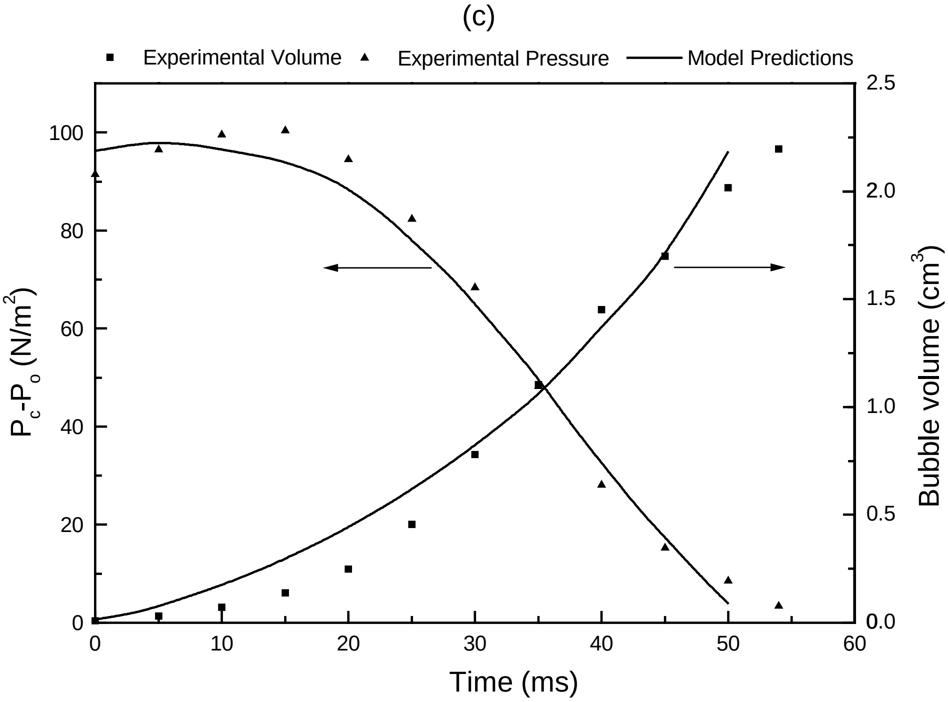

Fig. 5.1 Bubble shapes, growth curve and chamber pressure fluctuation for experimental conditions: Air/Water, Q = 16.7 cm^3/s, r_o= 0.16 cm, V_c= 2250 cm^3, H = 15.24 cm, from Kupferberg and Jameson (1969). (a) computed bubble shapes by present model; (b) approximate experimental shapes; (c) bubble growth curve and chamber pressure fluctuation.

For the CO$_2$-water system of LaNauze and Harris (1974) at elevated pressure with following experimental conditions:

Gas flow rate Q = 10 cm^3/s

Radius of the orifice r_o = 0.16 cm

Chamber volume V_c = 375 cm^3

Height of the liquid H = 10 cm;

System pressure P_∞ = 0.69 MN/m^2

the instantaneous shapes and bubble volume are shown in Fig. 5.2. The bubble shapes obtained by the present model are shown in Fig. 5.2(a). Fig. 5.2(b) compares the simulated bubble growth curves with the experimental data.

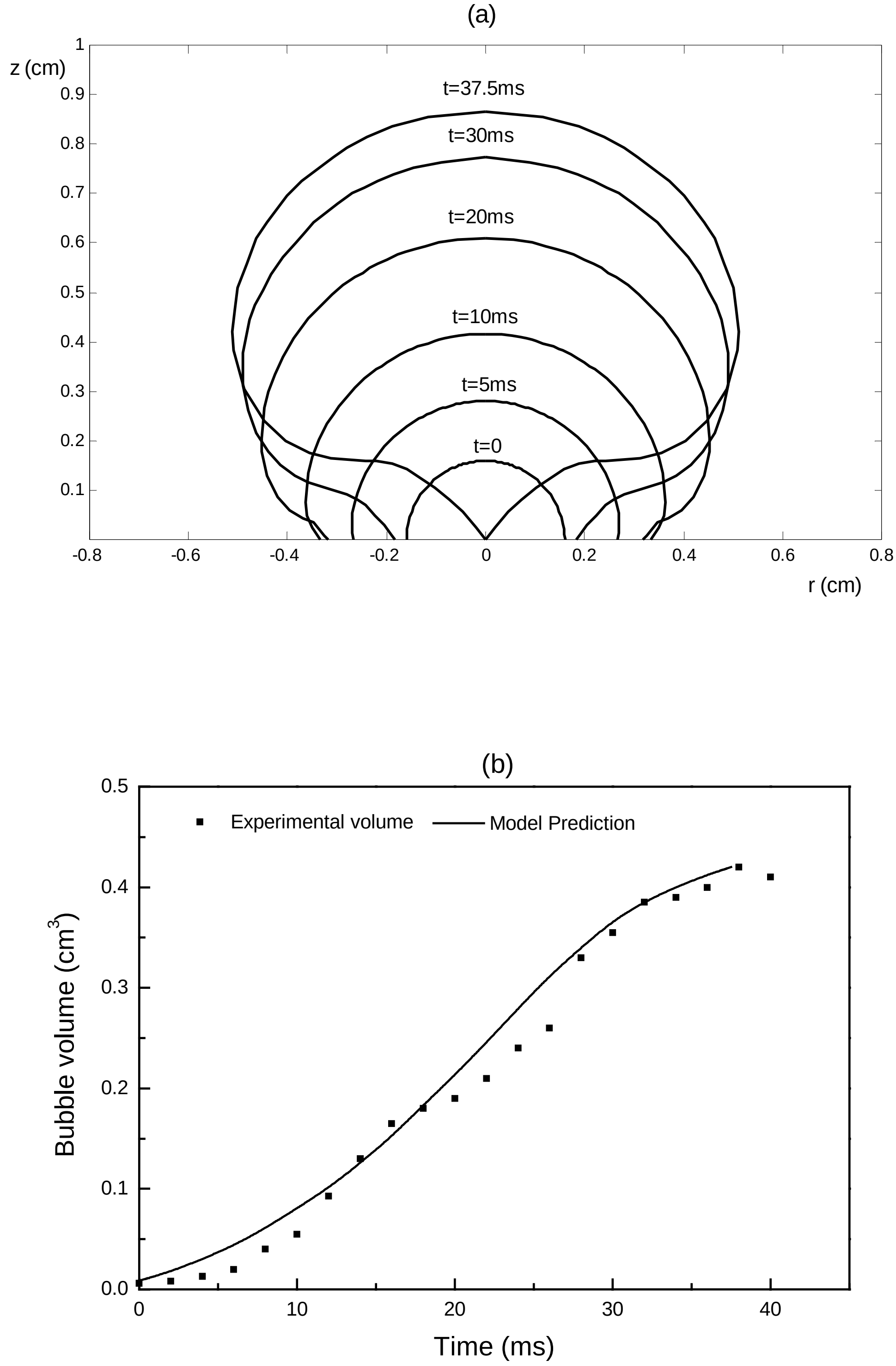

Fig. 5.2 Bubble shapes and growth curve for experimental conditions: CO_2/Water, system pressure 0.69 MN/m^3, Q = 10 cm^3/s, r_o = 0.16 cm, V_c = 375 cm^3, from LaNauze and Harris (1974). (a) computed bubble shapes by present model; (b) bubble growth curve .

Fig. 5.3 shows a comparison of the bubble shape traced experimentally from the high-speed video images with that calculated by the present model with the following experimental conditions:

Gas flow rate $Q = 0.854$ cm^3/s

Radius of the orifice $r_o = 0.12$ cm

Column diameter $d_c = 10$ cm

Chamber volume $V_c = 430$ cm^3

Height of the liquid $H = 30$ cm.

The experimental bubble shapes are not easy to determine precisely because of distortion due to cylindrical column. From visual inspection, it is observed that the experimental bubble shapes agree approximately with the predicted bubble shapes by the present model shown in Fig. 5.3(b).

Fig. 5.4 shows the variation of bubble volume at detachment with gas flow rate with orifice diameter as a parameter under the conditions of $V_c = 430$ cm^3 and $H = 30$ cm. The bubble volumes calculated by the present model are compared with the results obtained experimentally, and a reasonable agreement is observed from the comparison.

Surface tension is one of the contributing factors influencing the bubble volume. To verify the effect of surface tension, data has been collected for liquids of different surface tensions, water (σ = 72.7 dyn/cm) and petroleum ether (σ = 27.1 dyn/cm), using the same orifice ($r_o = 0.2$ cm) by Davidson and Schüler (1960). Fig. 5.5 shows the variation of bubble volume at detachment with gas flow rate for different liquids (Davidson and Schüler, 1960, as reported by Ramakrishnan, et al., 1969) and the calculated results are compared with the experimental data. It can been seen that at lower gas flow rates, surface tension has little effect on the bubble volume, while at higher flow rates, the lowering of surface tension produces smaller bubbles. It can be noted that our model predictions match the experimental trends closely.

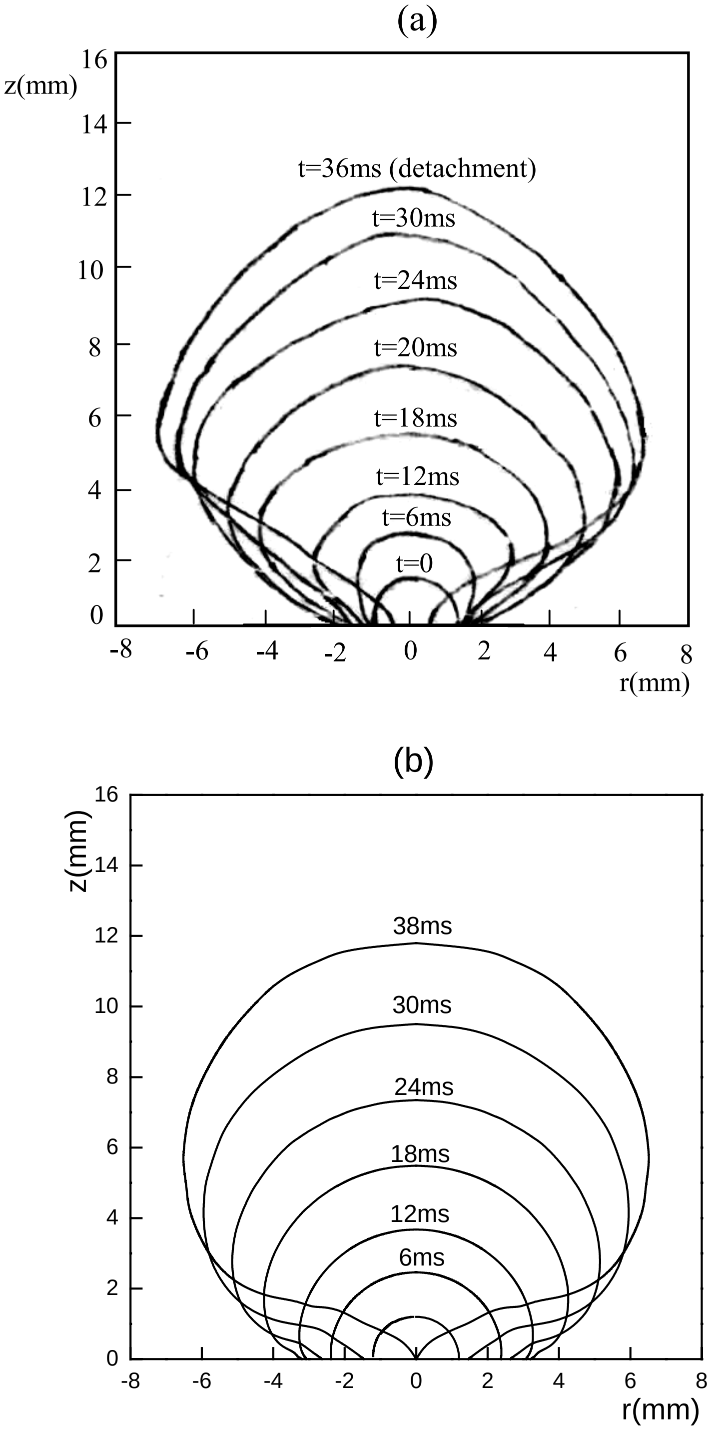

Fig. 5.3 Comparison of bubble shapes obtained experimentally with those calculated by present model for experimental conditions: Q = 0.854 cm^3/s, r_o = 0.12 cm, d_c = 10 cm, V_c = 430 cm^3, H = 30 cm. (a) experimental shapes (b) calculated shapes.

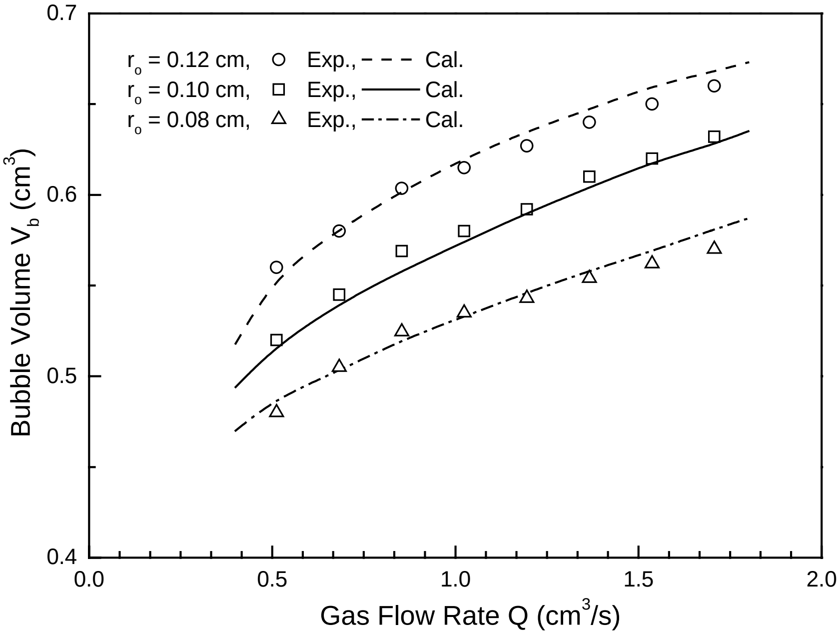

Fig. 5.4 Variation of bubble volume at detachment with gas flow rate.

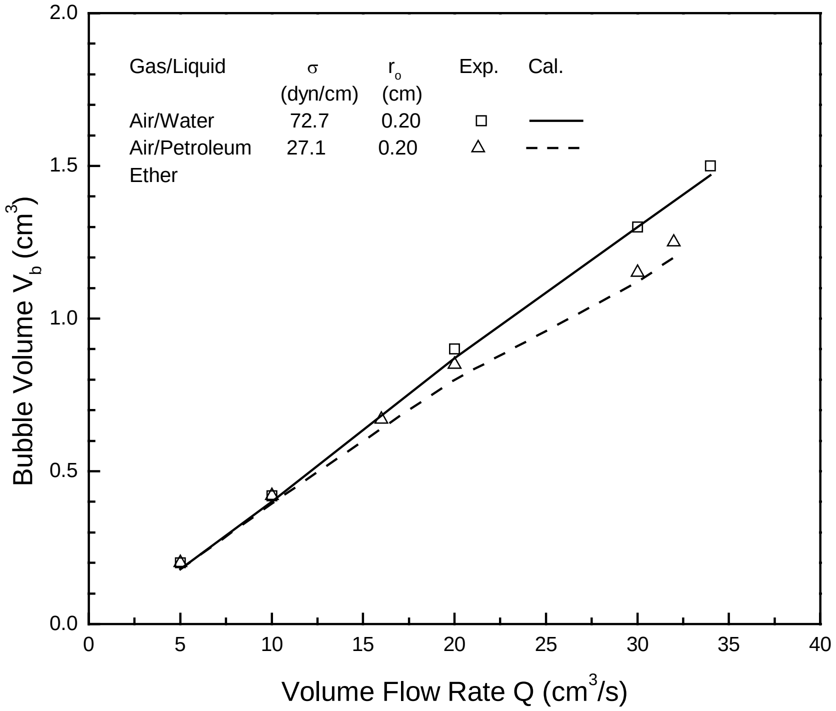

Fig. 5.5 Effect of surface tension on bubble size in inviscid liquid from Davidson and Schüler (1960)

5.2 Wall effect

5.2.1 Wall effect on bubbling regimes

The wall effect on bubble formation was investigated by carrying out experiments with different column sizes. Figure 5.6(a to c) shows the video sequences of bubble formation for various column diameters of 100 mm, 50 mm, and 30 mm respectively. The other parameters have been kept constant for these three sets of experiments as follows: gas flow rate $Q = 0.854\,\text{cm}^3$/s, chamber volume $V_c = 430\,\text{cm}^3$, the orifice diameter $d_o = 2.4\,\text{mm}$ and the liquid height $H = 30\,\text{cm}$.

It was observed that for the largest column with diameter $d_c = 100\,\text{mm}$, only one single bubble was formed for each cycle and when the bubble detached, the process entered into the waiting period till the next cycle starts, i.e. this is clearly a case of single bubbling. When $d_c = 50\,\text{mm}$, it was found that when the first bubble detached, a smaller second bubble was formed immediately and the second bubble caught up to and coalesced with the first one. After the second bubble detached, the process entered into the waiting period till the next cycle started; we can classify this as pairing. When $d_c = 30\,\text{mm}$, it was found that when the first bubble detached, a smaller second bubble was formed immediately and when the second detached, a smaller third bubble was formed immediately and the second and third bubbles caught up to and coalesced with the first one. After the third bubble detached, the process entered into the waiting period till the next cycle started; this was a case of multiple bubbling.

From the above observation, it is clear that the relative dimensions of the column and the orifice has a significant and profound effect on the bubbling regime.

(a)

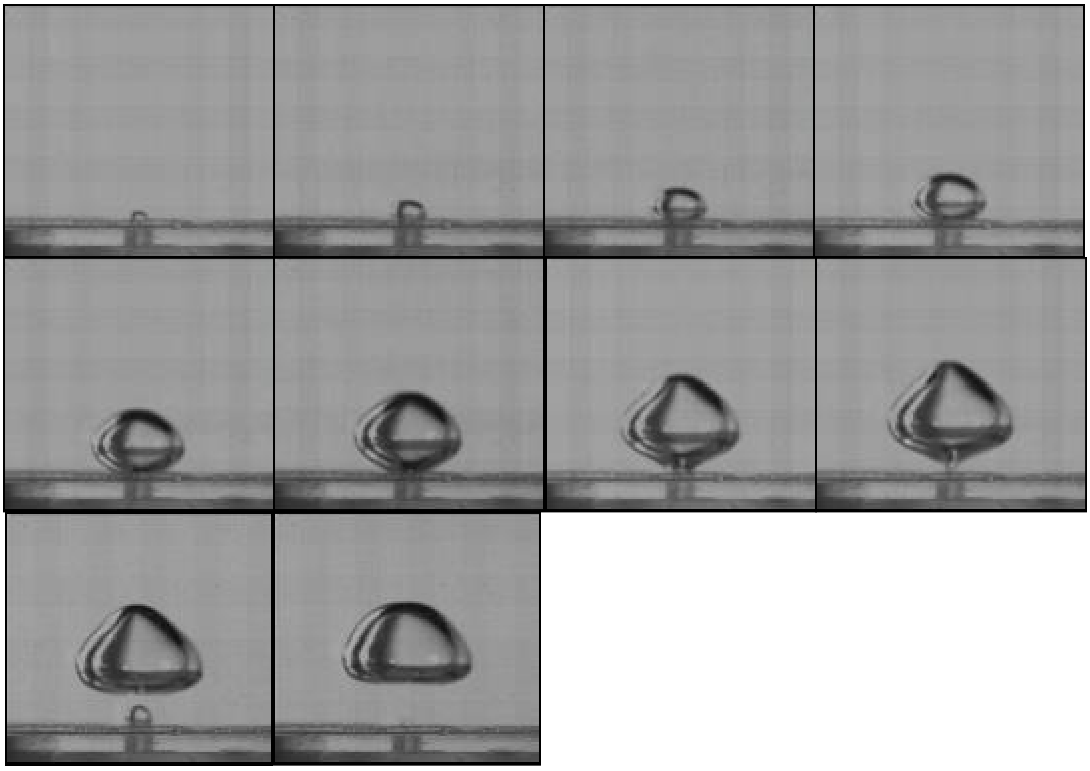

(b)

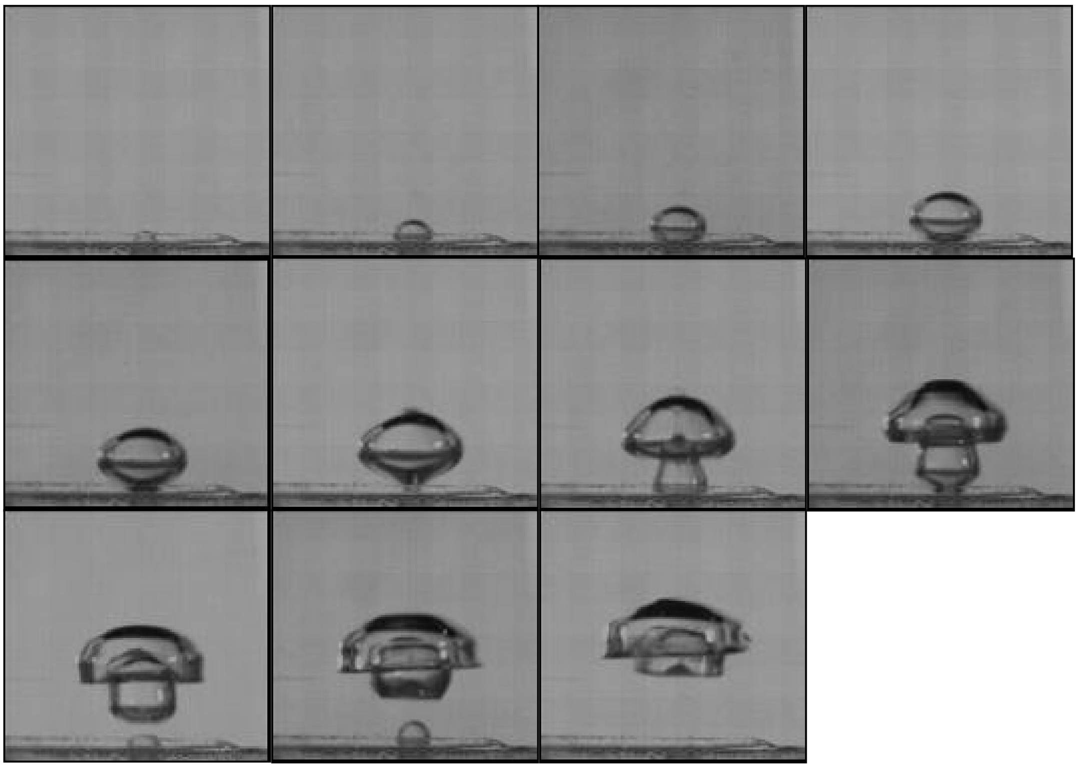

(c)

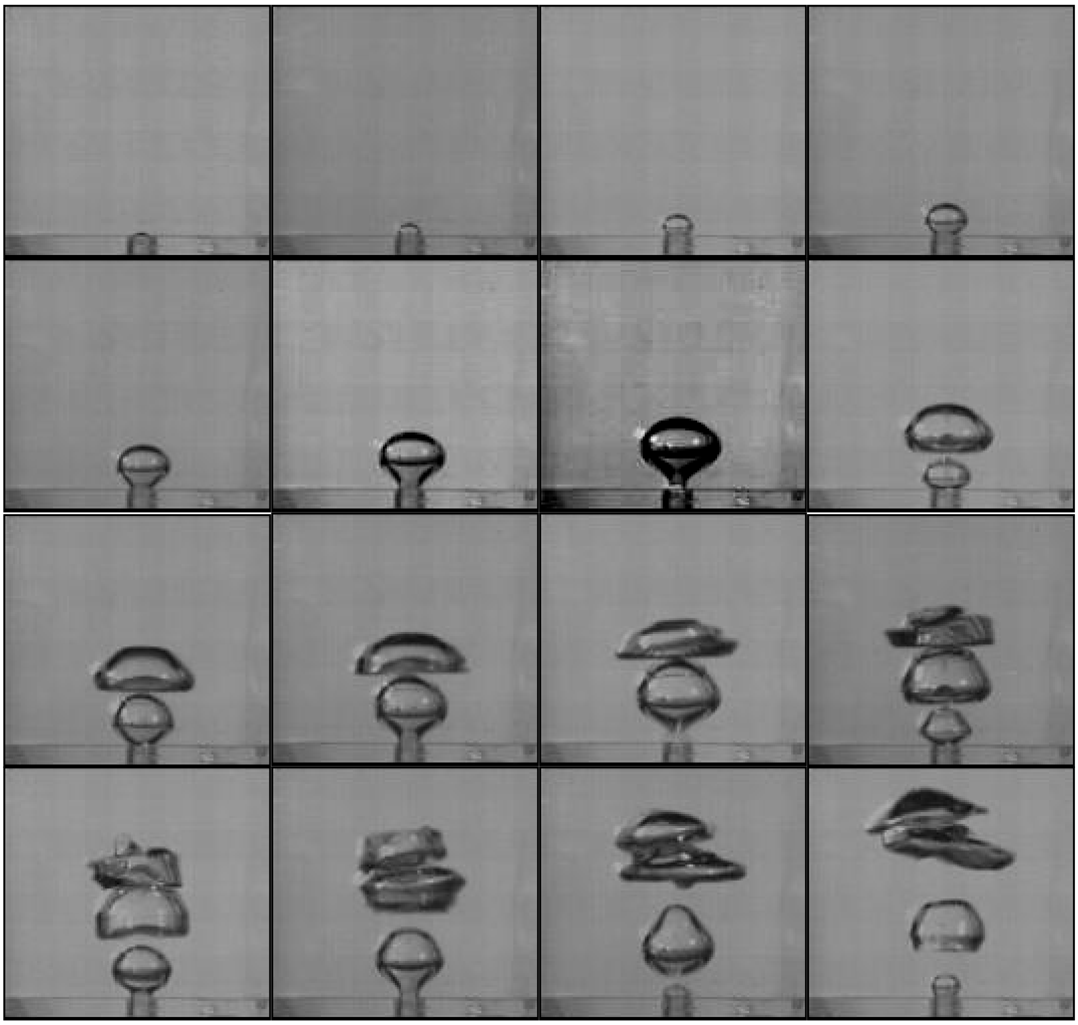

Fig. 5.6 High-speed video pictures at Q = 0.854 cm^3/s, d_o = 2.4 mm, V$_c$ =430 cm^3: (a) d_c = 100 mm, time interval = 6 ms; (b) d_c = 50 mm, time interval = 8 ms; (c) d_c = 30 mm, time interval = 8 ms.

When the chamber volume was changed from 430 cm^3 to 1000 cm^3 while keeping other operation conditions constant, i.e. gas flow rate $Q = 0.854$ cm^3/s, orifice diameter $d_o = 2.4$ mm and liquid height $H = 30$ cm for three sizes of column, the video sequences of bubble formation for column diameters of 100 mm, 50 mm, and 30 mm were shown in Figs. 5.7 (a) to (c) respectively.

(a)

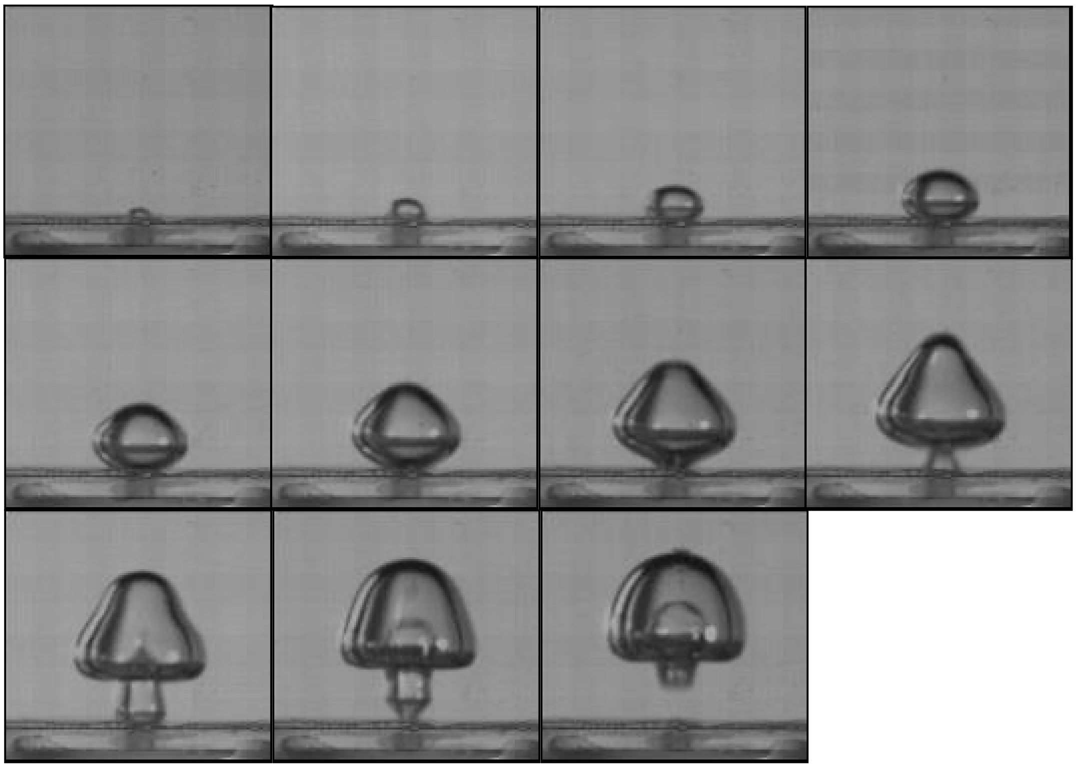

(b)

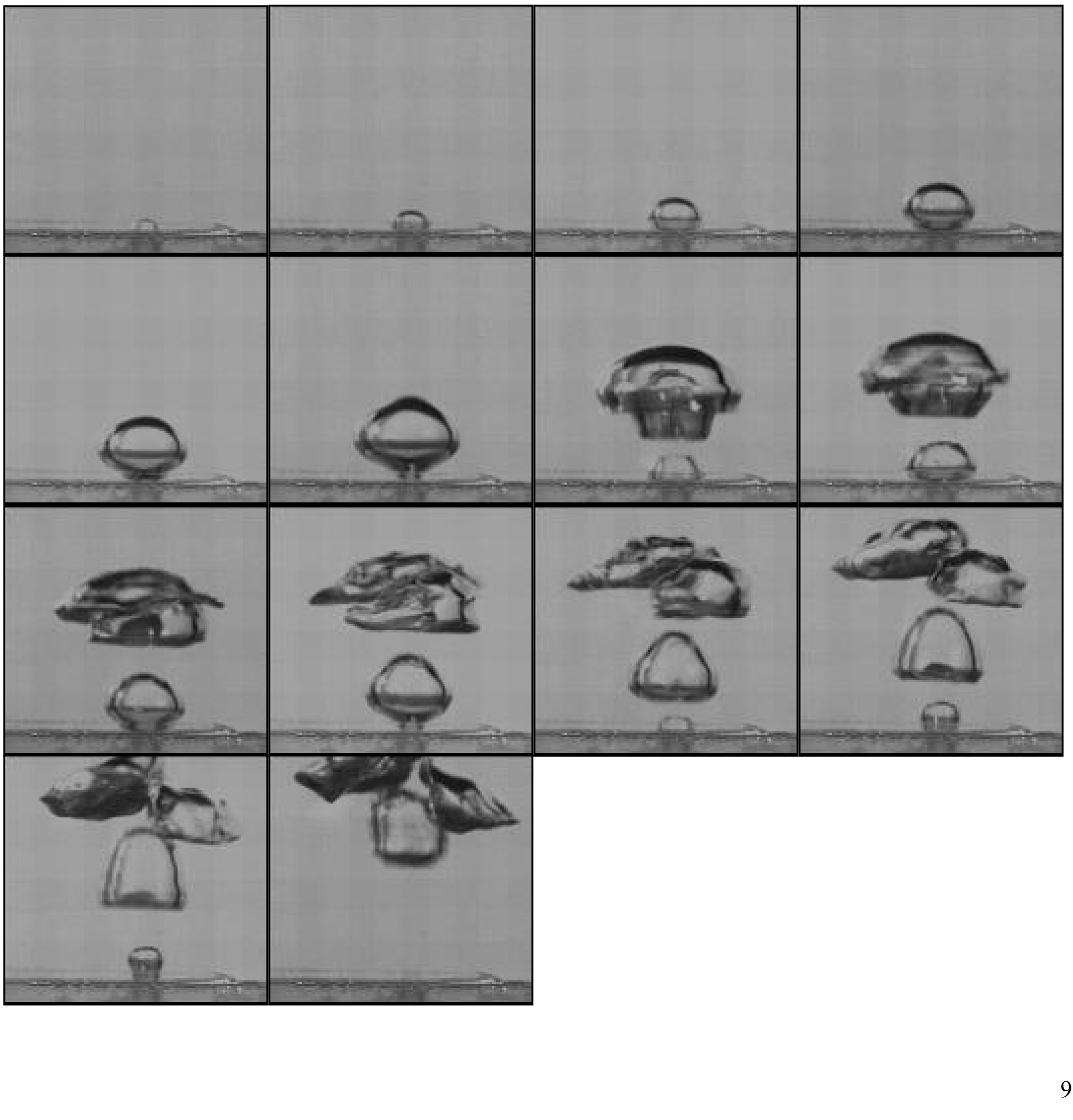

(c)

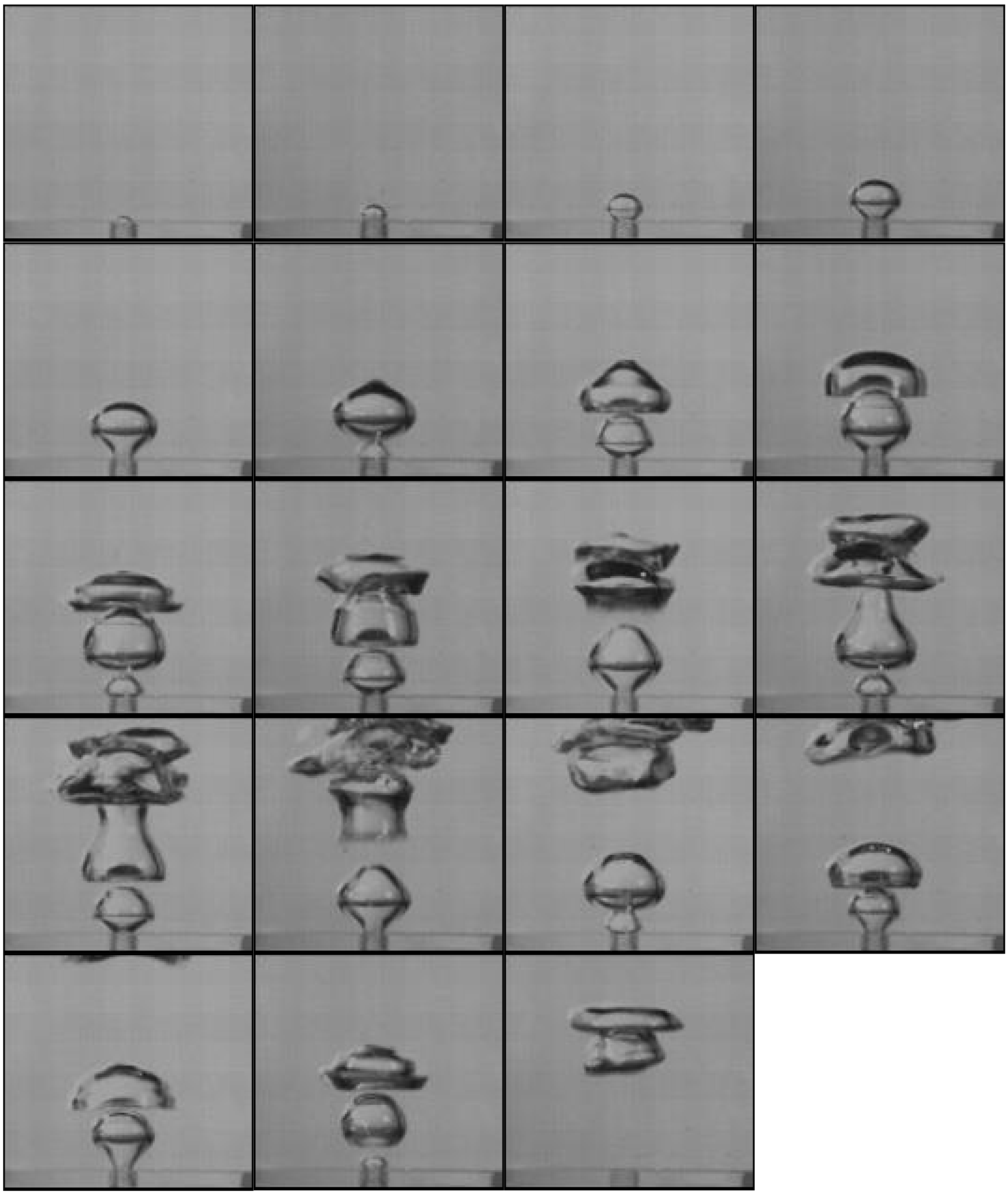

Fig. 5.7 High-speed video pictures at $Q = 0.854$ cm^3/s, $d_o = 2.4$ mm, $V_c = 1000$ cm^3: (a) $d_c = 100$ mm, time interval = 6 ms; (b) $d_c = 50$ mm, time interval = 8 ms; (c) $d_c = 30$ mm, time interval = 10 ms.

It was observed from Fig. 5.7 (a) that for $d_c = 100$ mm, a smaller second bubble was formed immediately after the first detached and the second one caught up to and coalesced with the first one. After the second bubble detached, the process entered into the waiting period till the next cycle started. Compared with the case of single bubbling with chamber volume $V_c = 430\,\text{cm}^3$ (Fig. 5.6(a)), the larger chamber volume has clearly shifted the bubble formation into the pairing regime. For $d_c = 50\,\text{mm}$ and 30 mm, the bubble formation for $V_c = 1000\,\text{cm}^3$ was clearly within the multiple bubbling regime, i.e. three or more bubbles were formed in rapid succession during each bubbling cycle.

The results show that with an increase of the chamber volume, the regime of the bubble formation will shift towards pairing and multiple bubbling. This observation is consistent with McCann and Prince's (1971) conclusion that pairing and multiple bubbling were more likely to occur in the case of large chamber volumes.

5.2.2 Wall effect on bubbling frequency

A typical set of the chamber pressure signals and the Fast Fourier Transform (FFT) analysis of the pressure signals for various column diameters of 100 mm, 50 mm, and 30 mm are shown in Figures 5.8 and 5.9 respectively. The other parameters are kept constant for these three sizes of column as follows: gas flow rate $Q = 3.415\,\text{cm}^3/\text{s}$, chamber volume $V_c = 430$ cm^3, orifice diameter $d_o = 2.4$ mm and liquid height $H = 30\,\text{cm}$. It is observed that by decreasing the column diameter, with all other conditions remaining unchanged, the bubbling frequency decreases.

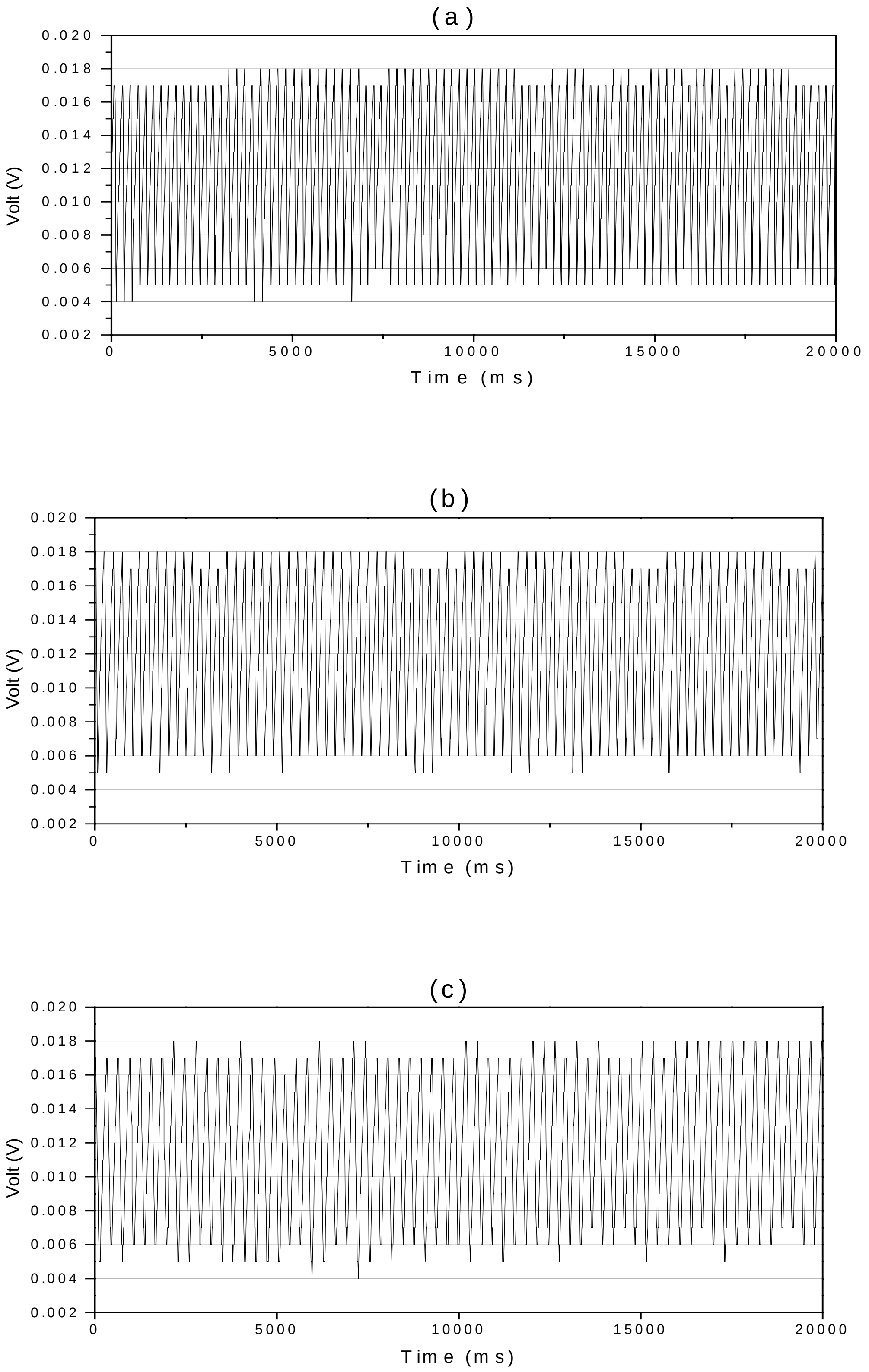

Fig. 5.8 Typical pressure signals with several column diameters (a) d_c = 100 mm (b) d_c = 50 mm (c) d_c = 30 mm at d_o = 2.4 mm, Q= 3.415 cm^3/s, V_c = 430 cm^3

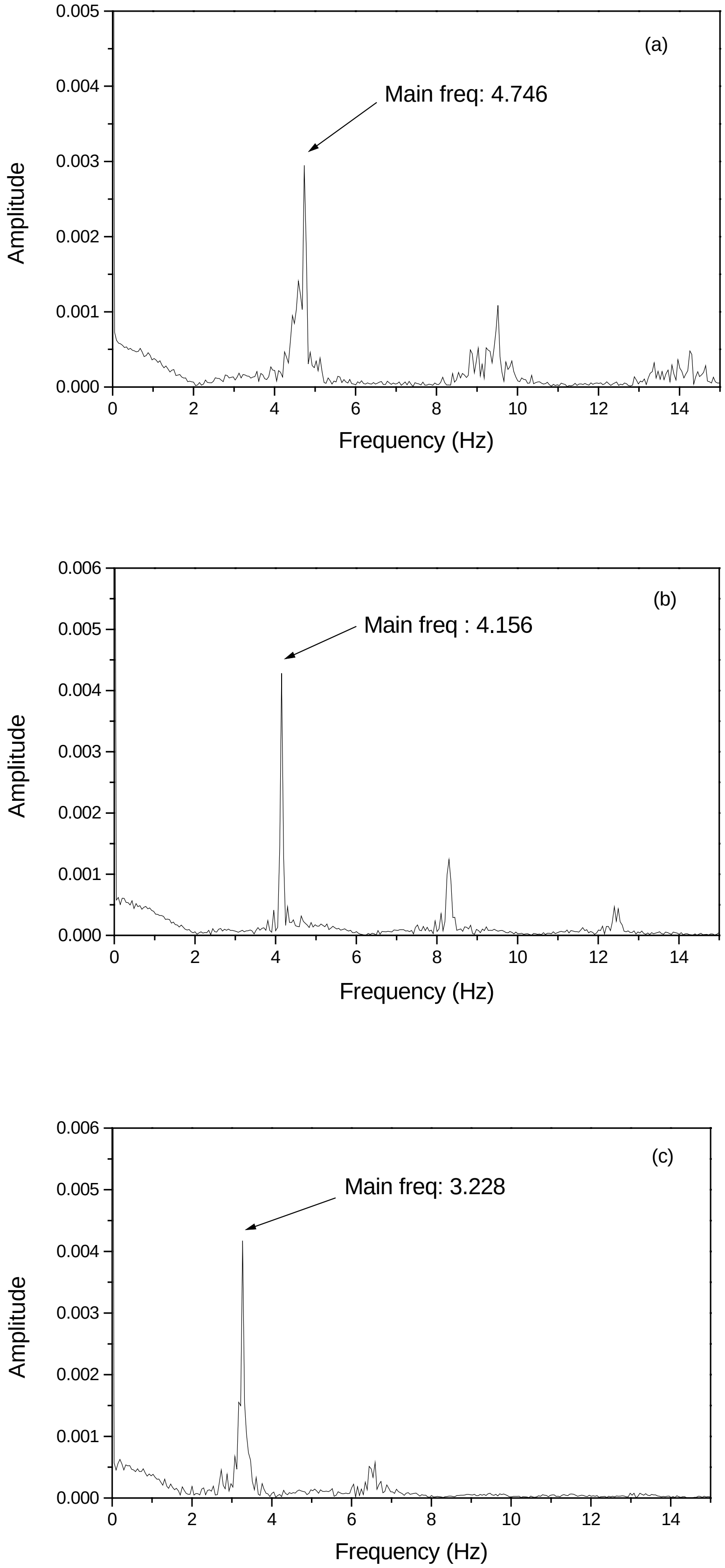

Fig. 5.9 Signal spectrum with several column diameters (a) d_c = 100mm (b) d_c = 50mm (c) d_c = 30 mm at d_o = 2.4 mm, Q= 3.415 cm^3/s, V_c = 430 cm^3

There are other factors affecting bubbling frequency, such as chamber volume and gas flow rate. To obtain a comprehensive understanding of the wall effect on bubbling frequency with the consideration of those factors, a series of experiments were carried out by changing the experimental conditions of chamber volume and gas flow rate.

The validity of our theoretical model was investigated by comparing simulated results of bubbling frequency with a wide range of experimental data for various column and orifice diameters, chamber volumes and gas flow rates.

Fig. 5.10(a) shows the relationship between bubbling frequency and gas flow rate for three sizes of column with orifice diameter $d_o = 1.6\,\mathrm{mm}$ and chamber volume $V_c = 430\,\mathrm{cm}^3$. The comparisons of experimental results with theoretical predictions are also shown in this figure. When orifice diameters are changed to 2.0 mm and 2.4 mm, the corresponding relationships are shown in Figs. 5.10(b) and 5.10(c) respectively. It is observed that bubbling frequency increases with an increase of the gas flow rate and also column diameter, whereas bubbling frequency decreases with increasing orifice diameter. Our theoretical model predicts these trends very well, and the agreement between simulated and experimental frequencies is good.

The corresponding bubbling frequencies for $V_c = 1000\,\mathrm{cm}^3$ are shown in Figs. 5.11(a), (b) and (c) for orifice diameters, 1.6 mm, 2.0 mm and 2.4 mm respectively. The experimental trends are similar to those in Fig. 5.10, and again there is good agreement between theoretical predictions and experimental data.

(a)

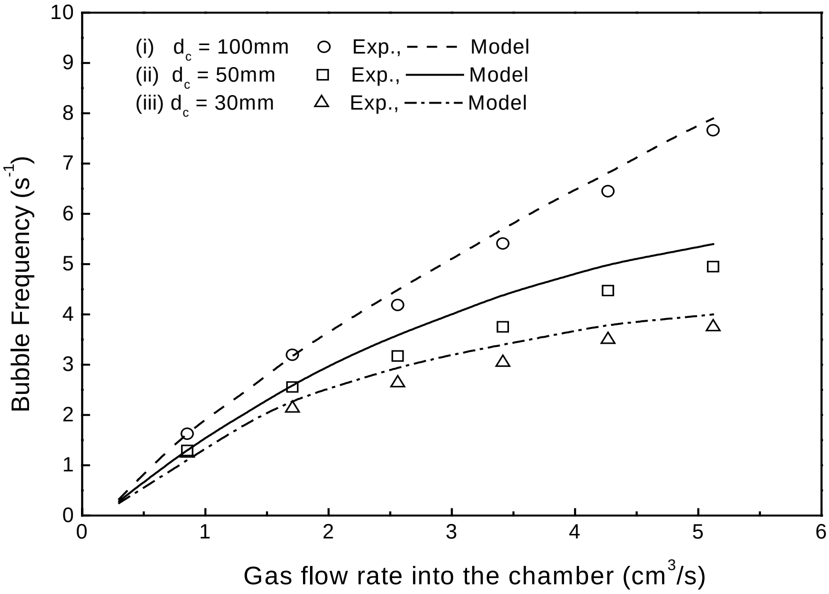
(i) d_c = 100mm ○ Exp., – – – Model
(ii) d_c = 50mm □ Exp., —— Model
(iii) d_c = 30mm △ Exp., –·–·– Model
Bubble Frequency (s^{-1})
Gas flow rate into the chamber (cm^3/s)
0
1
2
3
4
5
6
7
8
9
10
0
1
2
3
4
5
6

(b)

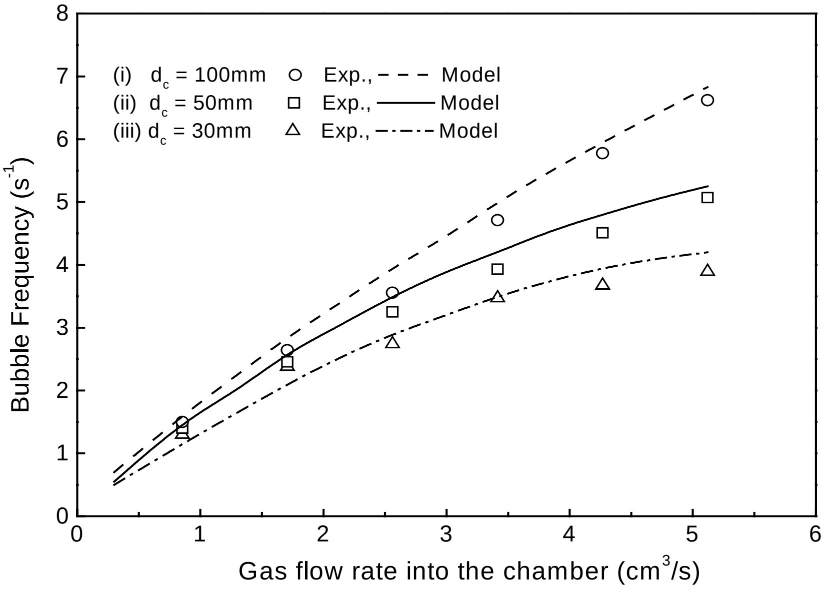
(i) d_c = 100mm ○ Exp., – – – Model
(ii) d_c = 50mm □ Exp., —— Model
(iii) d_c = 30mm △ Exp., –·–·– Model
Bubble Frequency (s^{-1})
Gas flow rate into the chamber (cm^3/s)
0
1
2
3
4
5
6
7
8
0
1
2
3
4
5
6

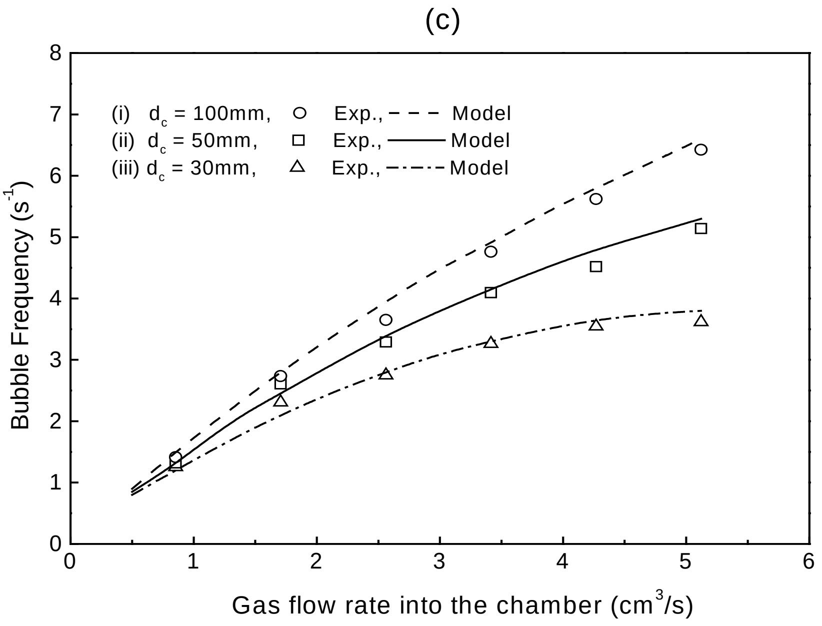

Fig. 5.10 Relationship between bubble frequency and gas flow rate for various column diameters (i) d_c = 100 mm (ii) d_c = 50 mm (iii) d_c = 30 mm at V_c = 430 cm^3: (a) d_o = 1.6 mm; (b) d_o = 2.0 mm; (c) d_o = 2.4 mm

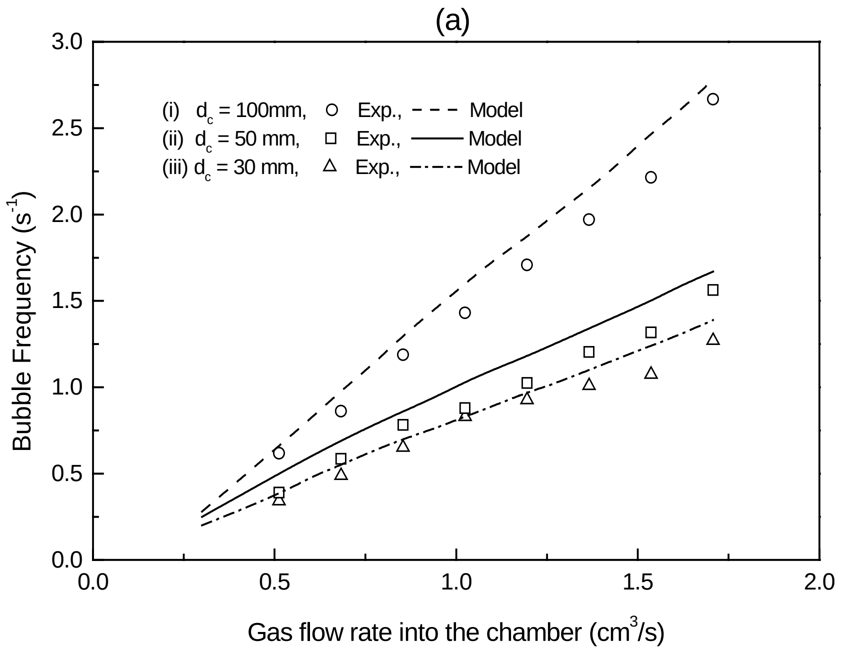

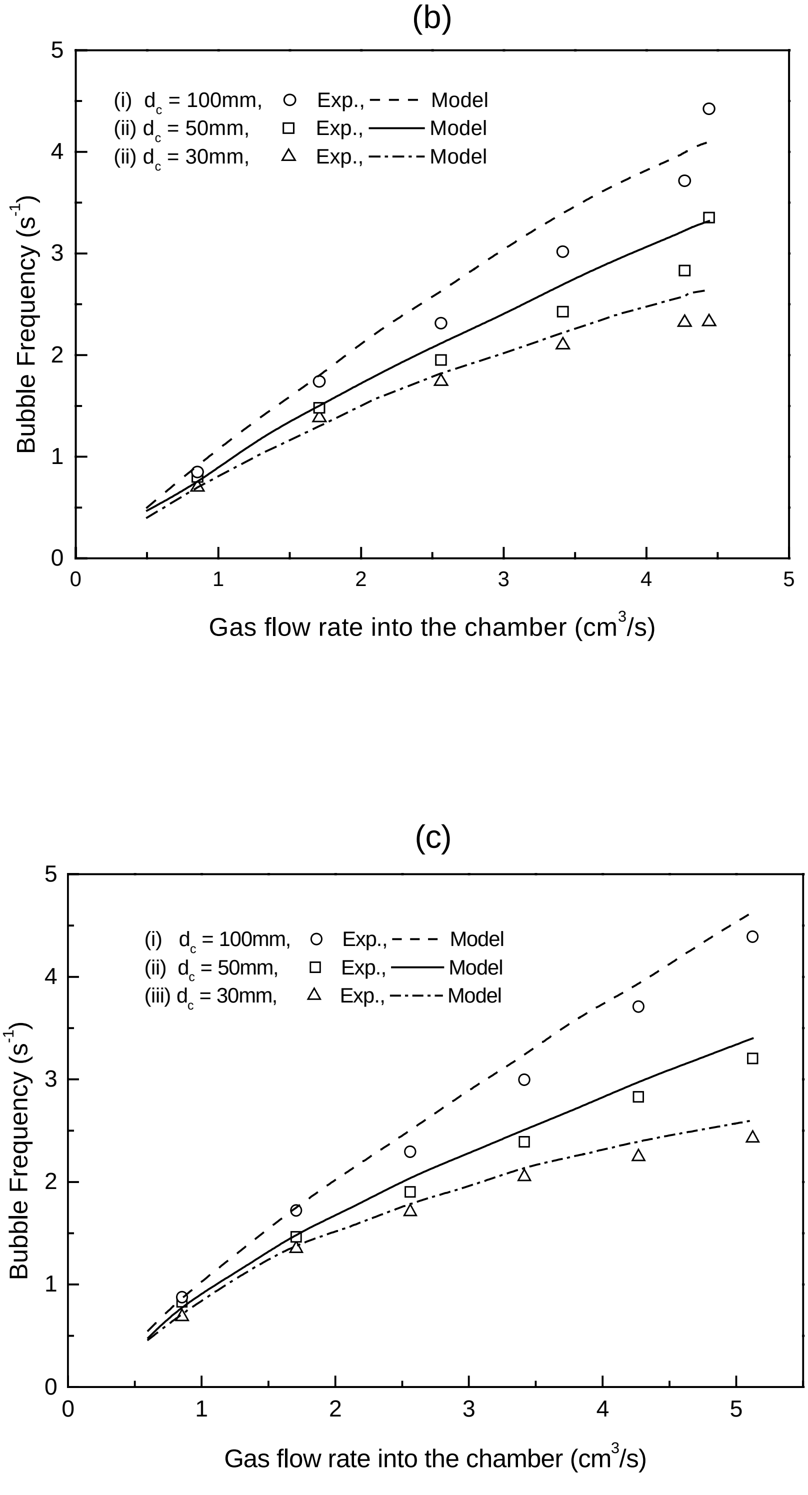

Fig. 5.11 Relationship between bubble frequency and gas flow rate for various column diameters (i) d_c = 100 mm (ii) d_c = 50 mm (iii) d_c = 30 mm at V_c = 1000 cm^3: (a) d_o = 1.6 mm; (b) d_o = 2.0 mm; (c) d_o = 2.4 mm.

5.3 Discussion

The theoretical model developed with the boundary integral method has been validated for single bubbling through the comparison of experimental results with theoretical predictions. The model predicts the instantaneous bubble shape, detachment time as well as the chamber and bubble pressure. In addition, the wall effect on bubble formation was investigated experimentally and theoretically. As the ratio of the column diameter to orifice diameter is decreased, the bubbling regimes generally transition from single bubbling to pairing and multiple bubbling, with a corresponding decrease in bubbling frequency. It is due to the fact that with the decrease of the ratio of column to orifice diameter, the liquid circulation increases which affects bubble formation, and the detachment happens earlier resulting in smaller bubble volume. Comparison of experimental results for bubbling frequency with the theoretical predictions shows that the agreement is good, i.e. the boundary integral model successfully predicts the effect of the column wall on bubbling frequency.

However, this model does not take into account the bubble-bubble interaction caused by preceding detached bubble. Also this model has the limitation of not being able to predict the occurrence of pairing and multiple bubbling. Hence, to understand thoroughly the underlying mechanism and take into consideration of the wake effect caused by the preceding bubble as well as the bubble-wall interaction, a simplified model based on spherical bubble formation and potential flow theory is proposed in Chapter 6.

Chapter 6 Theoretical modeling of bubble-wall and bubble-bubble interactions

In this chapter, the development and the solution strategy for the theoretical modeling of bubble-wall and bubble-bubble interactions are described in Section 6.1 and Section 6.2 respectively. Results and conclusions obtained from this study are presented in Section 6.3 and Section 6.4, respectively.

6.1 Model development

6.1.1 Physical system and basic assumptions

The schematic diagram of the physical system is shown in Fig. 6.1 and the primary assumptions of the model are:

(i). The bubble shape is a spheroidal segment during formation and deforms into a spherical-cap bubble after detachment.

(ii). The depth of liquid above the plate is high enough compared with the bubble diameter so that it has no effect on bubble formation.

(iii). The gas is an ideal and compressible gas following an adiabatic process.

(iv). A detached and rising bubble is assumed to exert a wake pressure on the subsequent bubble forming at the orifice. However, a following bubble has no effect on velocity or shape of the preceding bubble.

(v). There is no energy exchange or mass transfer across the gas-liquid interface.

(vi). At a particular instant, the orifice experiences either upward gas flow (referred to as bubbling) or no flow (referred to as waiting). At any instant, the orifice only shows one of the above phases.

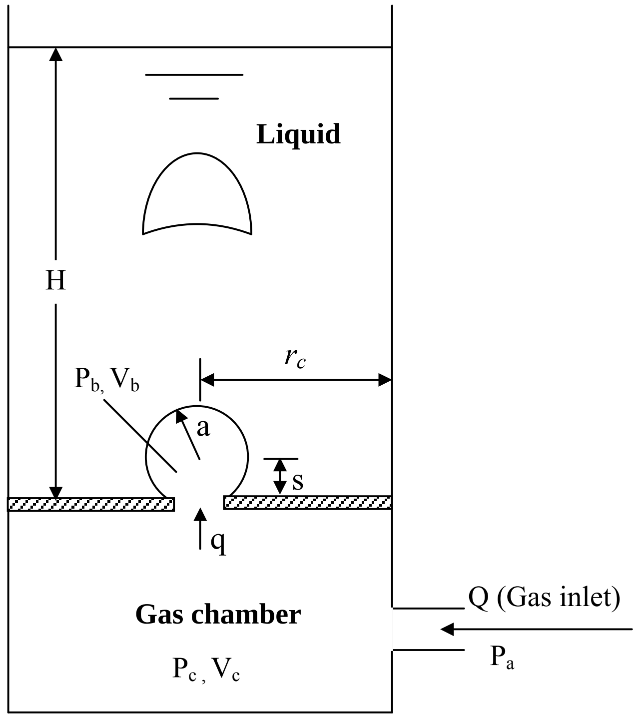

Fig. 6.1 Schematic diagram of physical system

6.1.2 Analysis of the gas chamber pressure

The change of pressure in the gas chamber, P_c, is obtained by assuming an adiabatic ideal gas and applying first law of thermodynamics to the gas chamber (Tan and Harris, 1986):

$$V_c \frac{dP_c}{dt} = \gamma P_c (Q - q) \tag{6.1}$$

where γ is the adiabatic exponent of the gas, V_c is the chamber volume, Q and q are the volumetric flow rates into the chamber and through the orifice, respectively.

6.1.3 Orifice equation

Gas flow through the orifice is determined by its physical dimensions and the pressure difference between the gas chamber and the bubble. As the upward gas momentum has been neglected, the volumetric gas flow rate and the pressure drop across orifice can be related according to the following equation:

$$\frac{dV_b}{dt} = k_o \sqrt{P_c - P_b} \tag{6.2}$$

where $k_o = \pi r_o^{\,2} \sqrt{2/\rho_g C_g}$ is the orifice coefficient, $C_g = 1.5 + 2f' b / r_o$ (Miyahara and Takahashi, 1984) and f' is the fanning friction factor, which is approximated by $f' = 16/\mathrm{Re}_o$ ($\mathrm{Re}_o = \dfrac{2\rho_g r_o u_o}{\mu_g}$, where u_o is instantaneous gas velocity through the orifice), if laminar flow is assumed; b is orifice plate thickness.

6.1.4 Liquid pressure analysis

The viscosity of the liquid is assumed negligible and the flow is assumed to be irrotational. Therefore, the potential flow theory can be used to describe the process.

Since the bubble is assumed to be spherical, a moving spherical coordinate system is used, with the origin located at the centre of the growing and translating bubble as shown in Fig. 6.2.

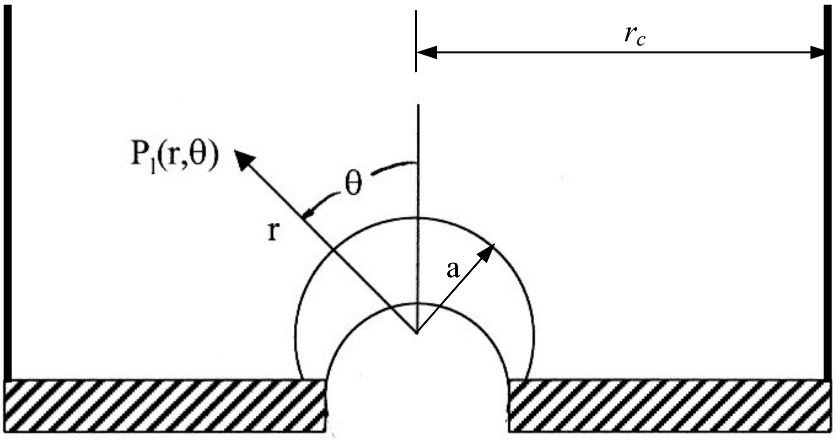

Fig. 6.2 Growth of a bubble.

For translation, the velocity potential and boundary conditions, which take the vertical column wall into account are:

$$\phi_T = \left[\frac{a^3 \sin^3\theta}{r_c^3 - a^3 \sin^3\theta} Ur + \frac{a^3 r_c^3}{2(r_c^3 - a^3 \sin^3\theta)} \frac{U}{r^2} \right] \cos\theta$$

$$-\frac{\partial\phi}{\partial r} = U\cos\theta, \qquad \text{when} \quad r = a$$

$$-\frac{\partial\phi}{\partial r} = 0, \qquad \text{when} \quad r = r_c / \sin\theta \qquad (6.3)$$

and for spherical expansion, the following velocity potential and boundary conditions apply:

$$\phi_P = \left[\frac{a^2 r_c^2}{r(r_c^2 - a^2 \sin^2\theta)} + \frac{a^2 r \sin^2\theta}{r_c^2 - a^2 \sin^2\theta} \right] \dot{a}$$

$$-\frac{\partial\phi}{\partial r} = \dot{a}, \quad \text{when} \quad r = a$$

$$-\frac{\partial\phi}{\partial r} = 0, \quad \text{when} \quad r = r_c / \sin\theta \qquad (6.4)$$

where *a* is an instantaneous bubble radius, r_c is radius of the bubble column, *U* is the bubble rising velocity, r and θ are the coordinates from the bubble center and the overdot denotes a time derivative.

The velocity potential, ϕ, around a spherical bubble which is expanding and rising can be expressed as the sum of the potential ϕ_T due to the rising motion and the potential ϕ_p associated with the expansion (Lamb, 1945; Tsuge et al., 1981), as follows:

$$\phi = \phi_T + \phi_P = \left[\frac{a^3 \sin^3\theta}{r_c^{\,3} - a^3 \sin^3\theta} Ur + \frac{a^3 r_c^{\,3}}{2(r_c^{\,3} - a^3 \sin^3\theta)} \frac{U}{r^2} \right] \cos\theta$$

$$+ \left[\frac{a^2 r_c^{\,2}}{r(r_c^{\,2} - a^2 \sin^2\theta)} + \frac{a^2 r \sin^2\theta}{r_c^{\,2} - a^2 \sin^2\theta} \right] \dot{a} \tag{6.5}$$

During bubble formation, the liquid pressure, $P_l(r,\theta)$, can be expressed as the sum of hydrostatic pressure, P_{st}, at that point, the pressure due to bubble expansion and translation, and the wake pressure arising from the preceding rising bubble. For a given liquid velocity distribution, Bernoulli's expression is

$$\frac{P_l(r,\theta) - P_{st} - P_w}{\rho_l} = \frac{\partial\phi}{\partial t} - \frac{1}{2}|u|^2 \tag{6.6}$$

where P_{st} and P_w are static pressure and wake pressure, respectively at the coordinate (r,θ), and the absolute liquid velocity is

$$|u| = \sqrt{\left(\frac{\partial\phi}{r\partial\theta}\right)^2 + \left(\frac{\partial\phi}{\partial r}\right)^2} \tag{6.7}$$

Translation of the (r,θ) coordinate system at velocity, U, may be accounted for by using the two expressions:

$$\dot{r} = -U\cos\theta\,,\ \ \dot{\theta} = U\frac{\sin\theta}{r} \tag{6.8}$$

Substituting Eqs. (6.5) and (6.7) into (6.6) and with some simplification, we obtain:

$$\begin{aligned}
\frac{P_l(r,\theta) - P_{st} - P_w}{\rho_L} = {} & \frac{2a\dot{a}^2 + a^2\ddot{a}}{r} + \frac{5a^2\dot{a}U\cos\theta}{2r^2} + \frac{a^3\dot{U}\cos\theta}{2r^2} - \frac{a^3U^2\sin^2\theta}{2r^3} + \frac{a^3U^2\cos^2\theta}{r^3} \\
& - \frac{a^4\dot{a}^2}{2r^4} - \frac{a^5\dot{a}U}{r^5}\cos\theta - \frac{a^6U^2}{8r^6}\sin^2\theta - \frac{a^6U^2}{2r^6}\cos^2\theta \\
& + \frac{2a\dot{a}^2 r\sin^2\theta + a^2\ddot{a}r\sin^2\theta + a^2\dot{a}U\sin^2\theta\cos\theta}{r_c^{\,2}} \\
& + \frac{3a^2\dot{a}Ur\sin^3\theta\cos\theta + a^3\dot{U}r\sin^3\theta\cos\theta + 2a^3U^2\sin^3\theta\cos^2\theta - a^3U^2\sin^5\theta}{r_c^{\,3}} \\
& + (\frac{a^2\dot{a}}{r^2} + \frac{a^3U\cos\theta}{r^3})(\frac{a^2\dot{a}\sin^2\theta}{r_c^{\,2}} + \frac{a^3U\sin^3\theta\cos\theta}{r_c^{\,3}}) \\
& + \frac{a^3U\sin\theta}{2r^2}(\frac{a^2\dot{a}\sin^2\theta}{r_c^{\,2}} + \frac{a^3U\sin^3\theta\cos\theta}{r_c^{\,3}})
\end{aligned} \tag{6.9}$$

P_{or} can be found by substituting $\theta = \pi, r = s$:

$$P_{or} = \frac{\rho_l a^2\ddot{a}}{s} + \frac{\rho_l a\dot{a}^2}{s}(2 - \frac{a^3}{2s^3}) - \frac{\rho_l a^2\dot{a}\dot{s}}{s^2}(1 - \frac{a^3}{s^3}) + \frac{\rho_l a^3\dot{s}^2}{s^3}(1 - \frac{a^3}{2s^3}) - \frac{\rho_l g a^3}{s^2} + P_{so} + P_{wo} \tag{6.10}$$

where P_{so} is the static pressure at the orifice and P_{wo} is wake pressure at the orifice.

6.1.5 Bubble pressure analysis

The pressure within the bubble, P_b, is assumed to be uniform and equal to the average pressure in the liquid at the bubble boundary, $\overline{P}_l$, plus the pressure due to surface tension.

The average liquid pressure at the bubble boundary, $\overline{P}_l$, can be calculated by integrating the liquid pressure over the bubble surface as follows:

$$\overline{P}_l \int_{-s}^{a} 2\pi a dx = \int_0^{\theta'} (2\pi a \sin\theta P_l(r,\theta) a)_{r=a} d\theta \tag{6.11}$$

Substituting into Equation (6.9), and using the results

$$\int_0^{\theta'} \sin\theta \cos\theta d\theta = \frac{a^2 - s^2}{2a^2}$$

$$\int_0^{\theta'} \sin\theta d\theta = \frac{a+s}{a}$$

$$\int_0^{\theta'} \sin^3\theta d\theta = \frac{2}{3} + \frac{s}{a} + \frac{s^3}{3a^3}$$

$$\int_0^{\theta'} \sin\theta \cos^2\theta d\theta = \frac{s^3}{2a^3} + \frac{1}{3}$$

$$\int_0^{\theta'} \sin^3\theta \cos\theta d\theta = \frac{1}{4} - \frac{s^2}{2a^2} + \frac{s^4}{4a^4}$$

$$\int_0^{\theta'} \sin^4\theta \cos\theta d\theta = \frac{(a^2 - s^2)^{5/2}}{5a^5}$$

where $\theta' = \cos^{-1}(-s/a)$

With some manipulation, we obtain

$$P_b = \rho_l(\frac{3}{2}\dot{a}^2 + a\ddot{a} - gs) - \frac{\rho_l U^2 a}{4(s+a)} \times (1 + \frac{5}{2}\frac{s}{a} - \frac{3s^3}{2a^3})$$

$$+\frac{\rho_l a}{a+s} \times \left[\frac{a^3\ddot{a}}{r_c^{\,2}}(\frac{2}{3} + \frac{s}{a} + \frac{s^3}{3a^3}) + \frac{a^2\dot{a}U + a^3\dot{a}U}{r_c^{\,2}}(\frac{1}{4} - \frac{s^2}{2a^2} + \frac{s^4}{4a^4}) \right.$$

$$\left. + \frac{4a^3\dot{a}U + a^4\dot{U}}{5r_c^{\,3}a^5}(a^2 - s^2)^{5/2} + \frac{3a^2\dot{a}}{r_c^{\,2}}(\frac{2}{3} + \frac{s}{a} + \frac{s^3}{3a^3}) \right] + P_{so} + P_{wb} + \frac{2\sigma}{a} \qquad (6.12)$$

where P_{wb} is the wake pressure imposed by the preceding bubble, which is discussed below.

6.1.6 Wake pressure analysis

The pressure field in the wake of a detached rising bubble will affect the growth of the next bubble. When the bubble detaches, a tongue of liquid moves upward into the rear of the bubble, so that the bubble immediately begins to deform towards a spherical-cap bubble and attains its terminal velocity (Clift et al., 1978). With Oseen's modification to potential flow, the wake pressure, caused by the detached rising bubble with steady velocity at the orifice, can be written as follows (Mittoni, 1997; Zhang and Tan, 2000):

$$P_{wo} = \frac{-6}{N_{\mathrm{Re}}}(\frac{\rho_l U_T^2}{2})\frac{a_{sc}^{\;2}}{s_{bo}^{\;2}} - \frac{\rho_l U_T^2 a_{sc}^3}{2s_{bo}^3} \qquad (6.13)$$

where a_{sc} is the cap radius of the rising spherical-cap bubble, U_T is the terminal rising velocity of the spherical-cap bubble, given by the expression of Davies-Taylor equation (Clift et al., 1978):

$$U_T = \frac{2}{3}\sqrt{\frac{g a_{sc}(\rho_l - \rho_g)}{\rho_l}} \qquad (6.14)$$

s_{bo} is the distance between the rising bubble and the orifice, $N_{\mathrm{Re}}\ (=2a_{sc}U_T\rho_l/\mu_l)$ is the Reynold number of the detached rising bubble.

Similarly, the wake pressure at the bubble surface is expressed as follows:

$$P_{wb} = \frac{-6}{N_{\mathrm{Re}}}(\frac{\rho_l U_T^2}{2})\frac{a_{sc}{}^2}{s_{bb}{}^2} - \frac{\rho_l U_T^2 a_{sc}^3}{2s_{bb}^3} \qquad (6.15)$$

where s_{bb} is the mean distance between the detached rising bubble and the growing bubble.

6.1.7 Force balance for the bubble

A force balance between the acceleration of added mass and buoyancy can be written as (LaNauze and Harris, 1974):

$$\frac{d}{dt}(\frac{11}{16}\rho_l V_b U) = (\rho_l - \rho_g)V_b g \qquad (6.16)$$

The value 11/16 is the added mass coefficient of a sphere in the vicinity of a plane wall (Milne-Thomson, 1968).

6.1.8 Bubble detachment criteria

With the growth and translation of the bubble, detachment will be possible if the liquid pressure at the orifice, P_{or}, becomes greater than the bubble pressure, P_b, at the instant in time when $s = a$ (i.e. the earliest time for detachment is when the bubble base is tangential to the orifice plate). If the orifice pressure, P_{or}, is also greater than the chamber pressure, P_c, weeping is possible after bubble detachment. This situation is known as "true single bubbling".

However, the phenomenon of "pairing" or “multiple bubbling” will be possible if $P_{or} < P_c$ when $s = a$. Immediately after the bubble has detached at the point of $s = a$, there is an instantaneous upward pressure drop across the orifice since $P_c > P_{or}$. This pressure difference, $P_c - P_{or}$, will cause a smaller second bubble to grow very quickly. When $s = a$, the second detaches and it catches up to and coalesces with the preceding bubble due to the upward wake pressure. The process repeats till P_c is not larger than P_{or} again. It is necessary at this stage to distinguish between “pairing” and “multiple bubbling”, although the two are very similar in appearance. One simple definition could be used to distinguish them as follows: only two bubbles are formed during one cycle of bubble formation for “pairing”, while more than two bubbles are formed during one cycle of bubble formation for “multiple bubbling”.

The criteria for detachment can now be expressed as: the bubble detaches at $s = a$; “pairing” or “multiple bubbling” happens if $P_{or} < P_c$ when the bubble has detached, a smaller second or third bubble is formed immediately after the preceding detachment; the bubble formation period is ended when P_c is not larger than P_{or} and it enters into the waiting period of one cycle.

6.1.9 Chamber pressure during waiting period

After bubble detachment, the pressure in the chamber will accumulate due to the continuous input of gas but no outflow of gas from chamber. The chamber pressure expression during waiting time is derived from Equation (6.1) under the condition $q = 0$:

$$\ln P_c = \frac{\gamma}{V_c} QT + \ln P_{cDET} \tag{6.17}$$

where T is the time from the instant of bubble detachment.

6.1.10 Bubble frequency *f*

One cycle of bubble formation consists of formation time and waiting time. The period between the starting point and the detachment point is defined as formation time, t_f, which can be obtained from the model. The time between the detachment of the one cycle of bubble and the growing of the next cycle bubble is defined as the waiting time, t_w, which can be obtained from Equation (6.17). Thus the bubble formation period equals to the sum of t_f and t_w. The frequency of bubble formation, f, which corresponds to the number of bubble formed per unit time, is the inverse number of the period as follows

$$f = \frac{1}{t_f + t_w} \tag{6.18}$$

6.2 Numerical solution strategy

The expression for gas flow rate into a growing spherical bubble,

$$q = \frac{dV_b}{dt} \tag{6.19}$$

and the definition of bubble rising velocity during formation,

$$U = \frac{ds}{dt} \tag{6.20}$$

ensure closure of the system of equations describing bubble formation. Equations (6.1), (6.2), (6.12), (6.13), (6.15), (6.16), (6.19) and (6.20) can be solved simultaneously for the variables P_c, P_b, P_{wb}, P_{wo}, q, a, s and U using a standard Runge-Kutta-Verner fifth and sixth order method.

The initial conditions were $P_c(0) = P_b(0) = P_\infty + \frac{2\sigma}{r_o} + P_{wo}(0)$, $q(0) = U(0) = s(0) = 0$, and $a = r_o$, corresponding to a hemisphere with radius equal to the orifice radius.

The simulations were carried out for a chain of bubbles. The initial bubble was allowed to form in a quiescent liquid, i.e., it experienced no wake effect. Each subsequent bubble was then simulated as forming, detaching and rising under the influence of the wake pressure of its immediate predecessor. In most cases, straightforward convergence was attained at the third cycle of bubble formation, i.e., the second and the third cycle of bubble formation were virtually identical. The converged values of waiting time, and formation time then constitute one bubbling cycle.

6.3 Results and discussion

6.3.1 Theoretical simulation of bubbling regimes

The chamber pressure fluctuations during one cycle of bubble formation, which were predicted by the present model, are shown in Figs. 6.3 (a) to 6.3 (c) for various column diameters of 100 mm, 50 mm and 30 mm respectively with the following conditions:

Gas flow rate $Q = 0.854$ cm^3/s

Radius of the orifice $r_o = 0.12$ cm

Chamber volume $V_c = 430$ cm^3

Height of the liquid $H = 30$ cm.

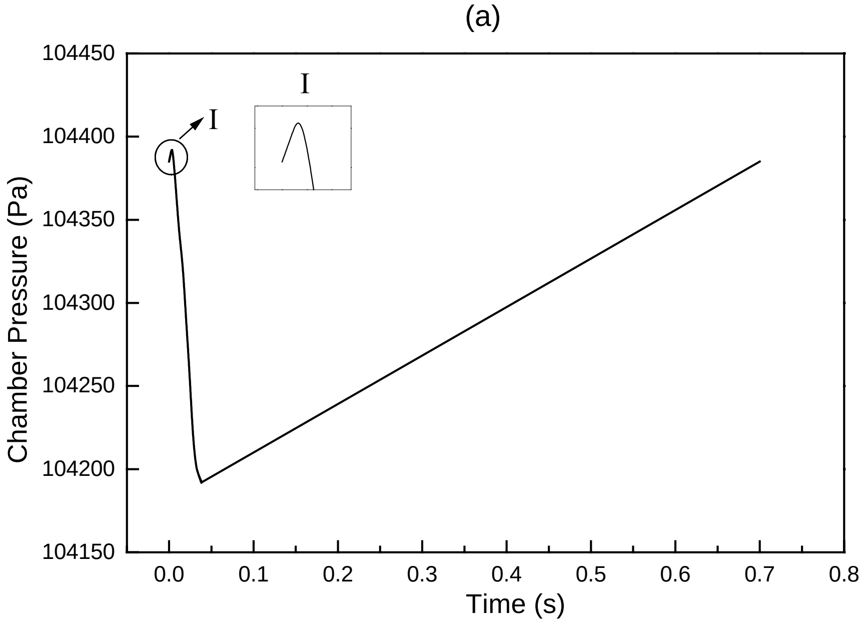

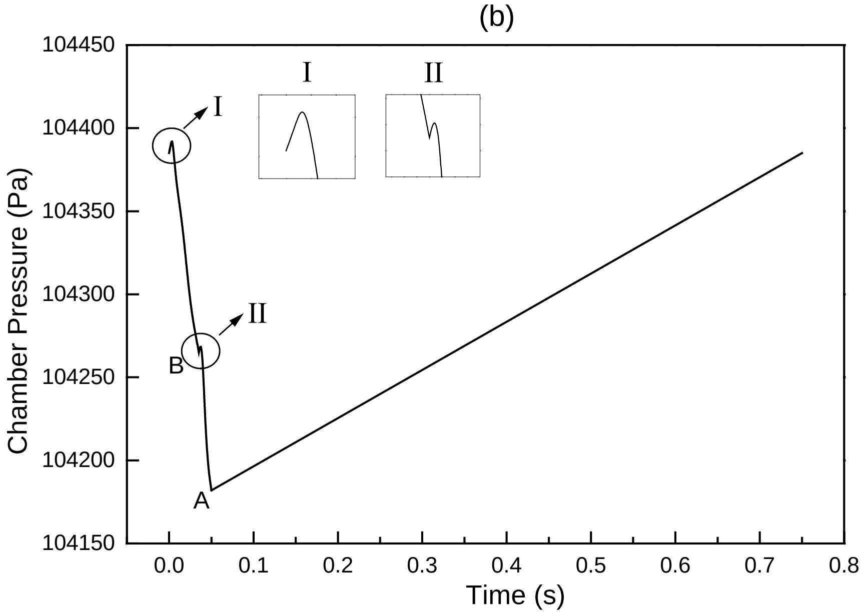

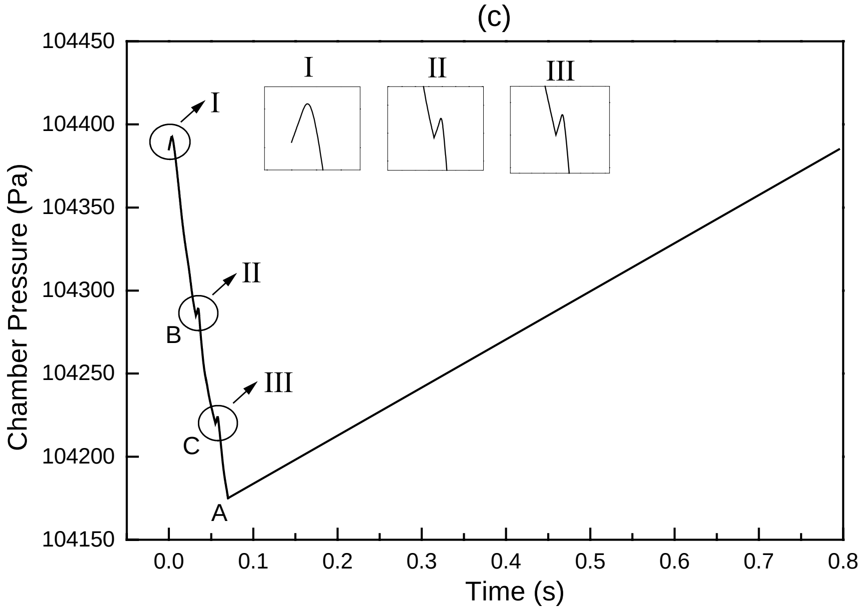

Fig. 6.3 Simulated chamber pressure fluctuation during one bubbling cycle for various column diameters (a) d_c = 100 mm (b) d_c = 50 mm (c) d_c = 30 mm at Q = 0.854 cm^3/s, r_o = 0.12 cm, V_c = 430 cm^3 and H = 30 cm.

It was observed that for each bubbling cycle, the chamber pressures increased briefly at the beginning of bubble formation, as a result of gas flow rate entering the chamber being higher than the gas flow rate through the orifice, shown as the inset I in each figure. Fig. 6.3(a) shows that after the short duration of pressure increase, the gas chamber pressure decreased until the lowest point A, at which the bubble detached from the orifice. After the bubble detachment, the chamber pressure increased linearly until the chamber pressure was high enough to initiate the next cycle of bubbling, which belongs to the waiting period. This is clearly a single bubbling regime.

Fig. 6.3(b) shows that with the bubble formation, the chamber decreased until point B, at which $s = a$ and the bubble detached at this point. Because of the higher chamber pressure than the orifice pressure at point A, a second bubble was formed immediately. After the first bubble detachment, there was also a short-term pressure increase as shown in inset II, after which the chamber pressure decreased again until the lowest point A, and the second bubble detached from the orifice at this point. After that, it enters into the waiting period until the next bubbling cycle happens, and this is a regime of pairing.

Fig. 6.3(c) shows that with the bubble formation, the chamber decreased until point B, at which $s = a$ and the bubble detached at this point. Because of the higher chamber pressure than the orifice pressure at point A, a second bubble was formed immediately. After the first bubble detachment, there was also a short-term pressure increase shown as the inset II, after which the chamber pressure decreased again until the point C where $s = a$, and the second bubble detached from the orifice at this point. Because the chamber pressure was still higher than the orifice pressure at point A, a third bubble was formed immediately. After the second bubble detachment, there was also a short-term pressure increase shown as the inset III, after which the chamber pressure decreased again until the point A, and the third bubble detached at this point. After that, it entered into the waiting period until the next bubbling cycle happens, and this is classified as multiple bubbling.

Wake pressure induced by detached rising was taken into account in this model. Wake pressure behind the rising bubble plays a significant role in determining bubble-bubble interaction, and the rotational motion in the liquid induced by the wake tends to detach the forming bubble earlier resulting in the transition of the bubbling regimes. It can be noted from the observation that our model can simulate the occurrence of the different bubbling regimes.

6.3.2 Comparison of experimental results with theoretical predictions

The validity of our theoretical model was investigated by comparing simulated results of bubbling frequency with a wide range of experimental data for various column and orifice diameters, chamber volumes and gas flow rates.

Fig. 6.4(a) shows the relationship between bubbling frequency and gas flow rate for three sizes of column with orifice diameter, $d_o = 1.6$ mm, and chamber volume, $V_c = 430\,\text{cm}^3$. It is observed that with the increase of the gas flow rate, the bubbling frequency increases, which is consistent with the observation in Snabre and Magnifotcham (1998). The comparisons between experimental results with theoretical predictions are also shown in this figure. When orifice diameters were changed to 2.0 mm and 2.4 mm, the corresponding relationships are shown in Figs. 6.4(b) and 6.4(c) respectively. The experimental trends are very clear: bubbling frequency increased with increasing column diameter and also with increasing gas flow rate, whereas bubbling frequency decreased with increasing orifice diameter. The simplified spherical growth model predicts these trends as well as the boundary integral model, and the agreement between simulated and experimental frequencies is very good.

The corresponding bubbling frequencies for $V_c = 1000\,\text{cm}^3$ are shown in Figs. 6.5(a), (b) and (c) for orifice diameters, 1.6 mm, 2.0 mm and 2.4 mm, respectively. The experimental trends are similar to those in Fig. 6.4, and again there is good agreement between theoretical predictions and experimental data.

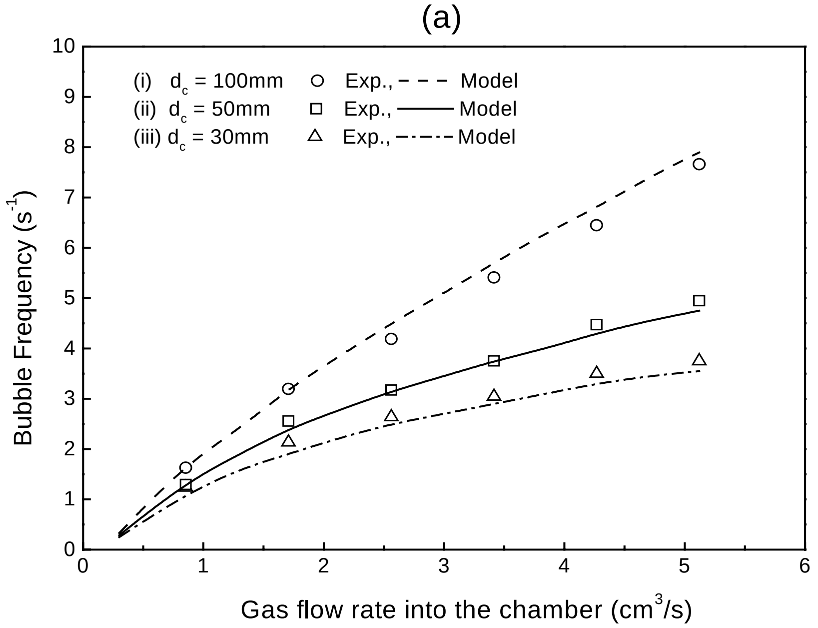
(a)
(i) d_c = 100mm ○ Exp., – – – Model
(ii) d_c = 50mm □ Exp., —— Model
(iii) d_c = 30mm △ Exp., –·–·– Model
Bubble Frequency (s^-1)
Gas flow rate into the chamber (cm^3/s)
0
1
2
3
4
5
6
7
8
9
10
0
1
2
3
4
5
6

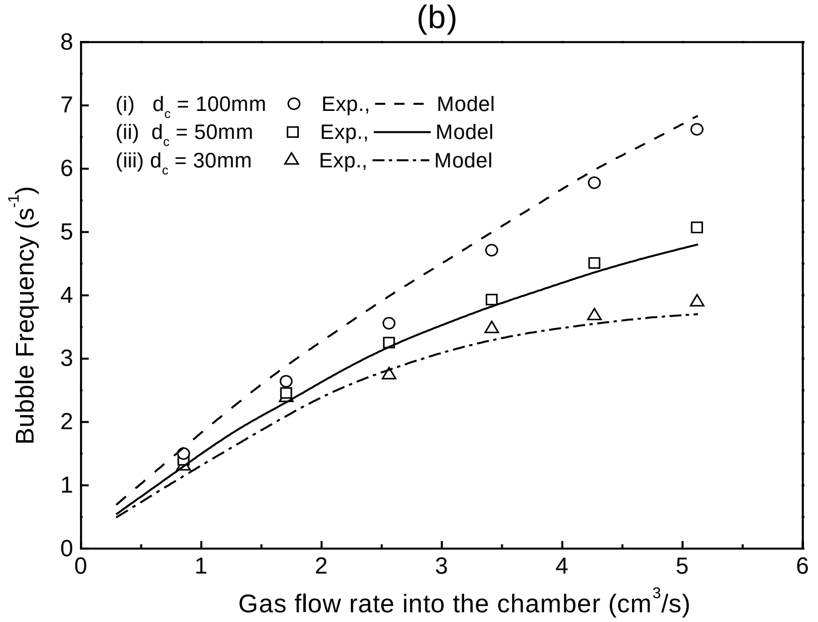
(b)
(i) d_c = 100mm ○ Exp., – – – Model
(ii) d_c = 50mm □ Exp., —— Model
(iii) d_c = 30mm △ Exp., –·–·– Model
Bubble Frequency (s^-1)
Gas flow rate into the chamber (cm^3/s)
0
1
2
3
4
5
6
7
8
0
1
2
3
4
5
6

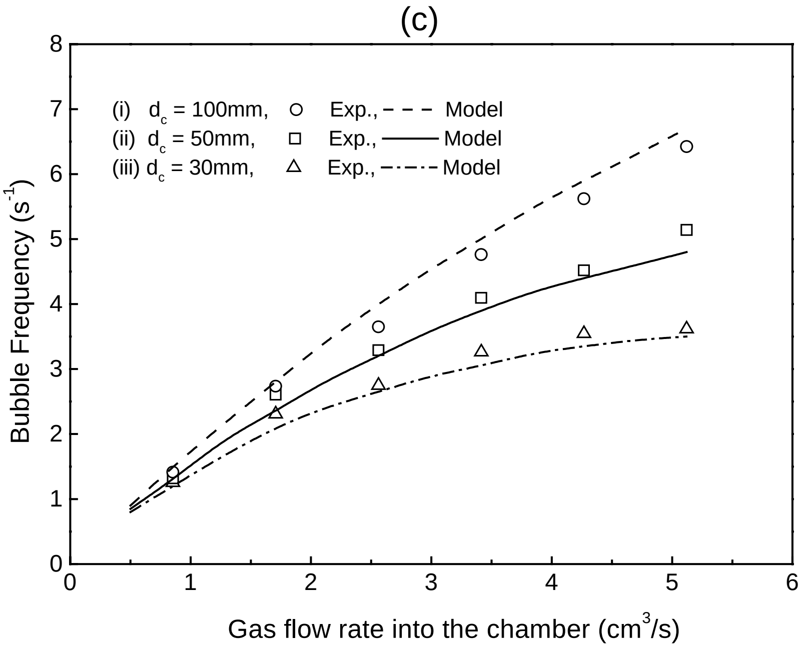

Fig. 6.4 Relationship between bubble frequency and gas flow rate for various column diameters (i) $d_c = 100$ mm (ii) $d_c = 50$ mm (iii) $d_c = 30$ mm at $V_c = 430$ cm^3: (a) $d_o = 1.6$ mm; (b) $d_o = 2.0$ mm; (c) $d_o = 2.4$ mm.

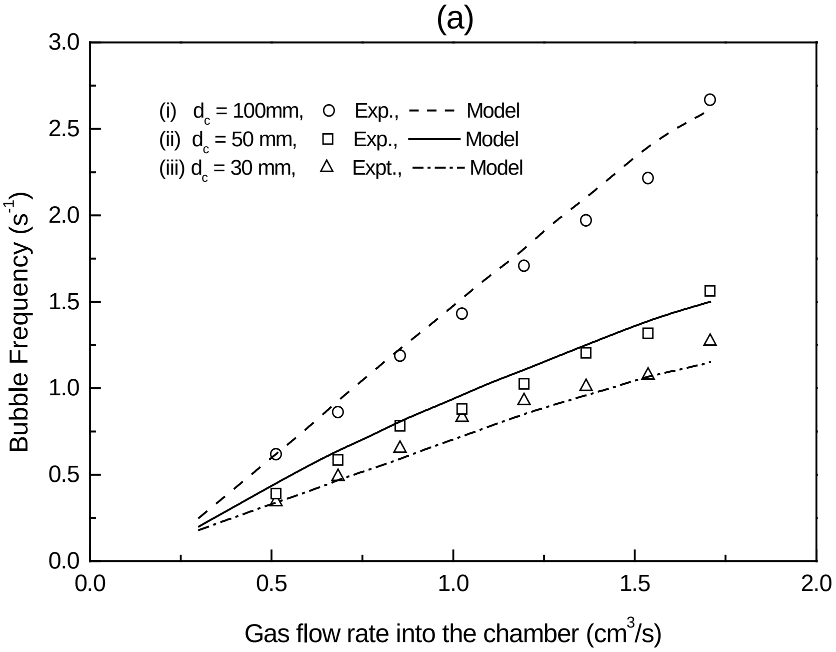

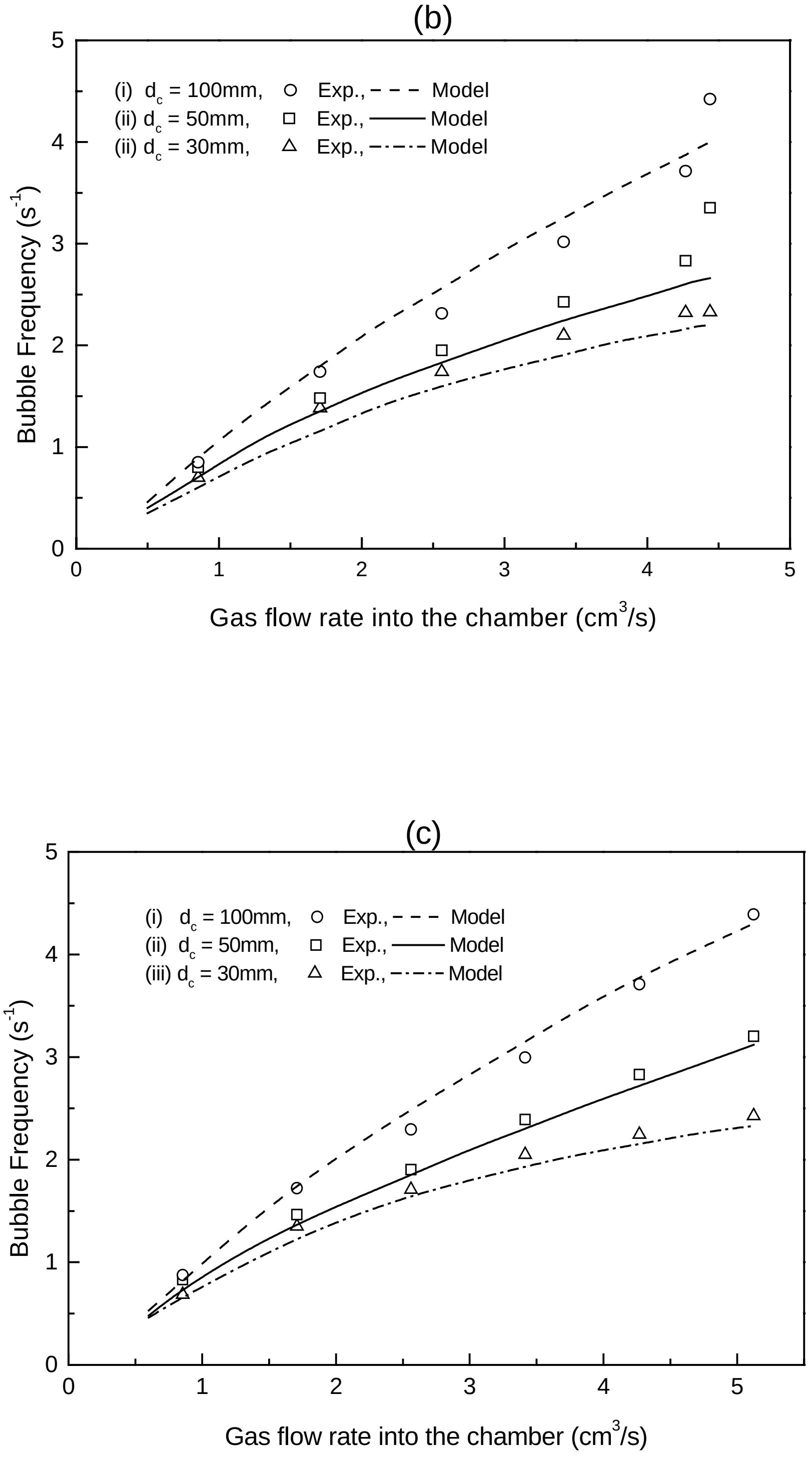

Fig. 6.5 Relationship between bubble frequency and gas flow rate for various column diameters (i) d_c = 100 mm (ii) d_c = 50 mm (iii) d_c = 30 mm at V_c = 1000 cm^3: (a) d_o = 1.6 mm; (b) d_o = 2.0 mm; (c) d_o = 2.4 mm.

6.3.3 Bubbling regime map

There are three bubbling regimes, single bubbling, pairing and multiple bubbling, which are determined by the ratio of the column diameter to the orifice diameter and gas flow rate. The experimental and theoretical regime maps are shown in Figs. 6.6(a) and (b) for chamber volume $V_c = 430\ \text{cm}^3$ and 1000 cm^3 respectively with gas flowrate and diameter ratio (d_c / d_o) as the parameters. Fig. 6.6 shows boundaries between the three bubbling regimes described earlier, viz., single bubbling, pairing and multiple bubbling regimes. It was observed that with the decrease of diameter ratio or increase of the gas flow rate, the bubbling regimes generally transition from single bubbling to pairing and multiple bubbling, and the theoretical regime boundaries were in good agreement with the experimental regime boundaries. For the larger chamber volume, the theoretical boundaries between adjacent regimes are shifted upwards significantly, in accord with our experimental findings. This is consistent with McCann and Prince's (1971) observation that pairing and doubling bubbling are more likely to occur in a large chamber volume.

At very low gas flowrates, below ~0.25 cm^3/s, the wall effect disappears, since single bubbling occurs for all values of d_c / d_o. The bubble frequency (and hence bubble volume) is also independent of d_c / d_o, as can be seen in Figs. 6.4 and 6.5. It appears that bubble-bubble interactions are negligible at low bubbling frequencies (less than ~1 s^{-1}).

6.4 Conclusions

A spherical bubble formation model, which takes into account the wake effect as well as the wall effect, has been developed using potential flow theory. Our investigation demonstrates that the bubble-wall and bubble-bubble interactions can have profound influence on bubbling frequencies and bubbling regimes in bubble formation at a submerged orifice. These effects have been successfully modelled by potential flow and bubble wake pressure analysis. Also, the occurrence of bubbling regimes could be predicted with this model.

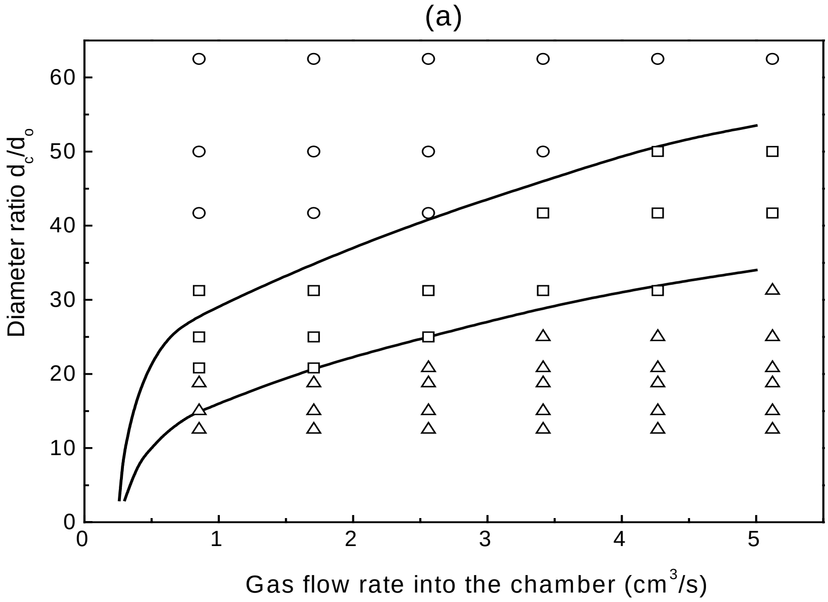

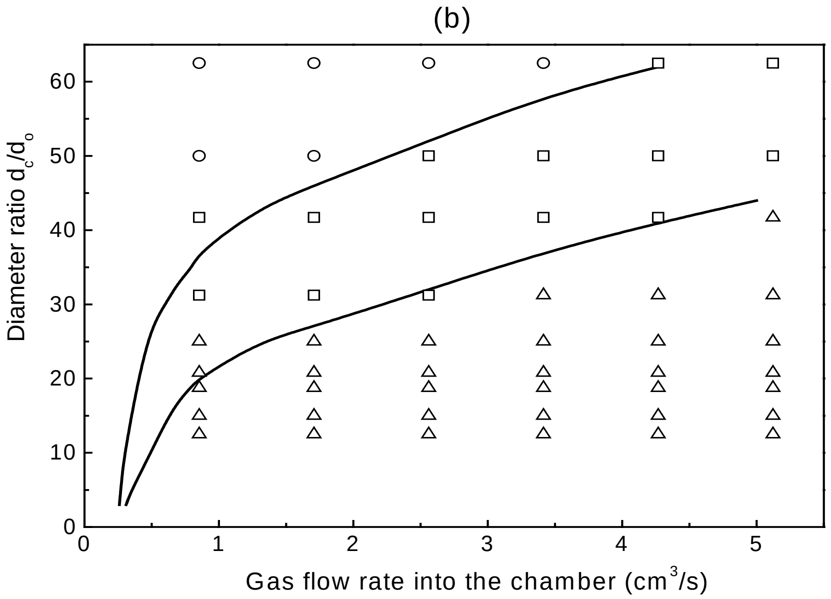

Fig. 6.6 Bubbling regime map at: (a) V_c = 430 cm^3; (b) V_c = 1000 cm^3. (Exp. Regimes: ○ single bubbling, □ pairing, Δ multiple bubbling; —— Predicted Regimes Boundary)

Chapter 7 Conclusions and recommendations

The mechanics of bubble formation has been investigated in the present study. In this chapter, the conclusions obtained from this study and the recommendations for further study are presented.

7.1 Conclusions

7.1.1 Conclusions on bubble formation in a quiescent liquid

This study attempted to study the mechanics of bubble formation in a quiescent liquid theoretically and an improved theoretical model was developed using the boundary integral method. The results, including the instantaneous shapes, detachment time, liquid circulation as well as the bubble and chamber pressure, obtained with this model were in substantial agreement with those data from reported experimental data. This shows that the model can predict the process of bubble formation very well.

Improvements and contributions from this research are summarized as follows:

1. The selection of dimensionless numbers representing the physical and dimensional parameters allows the natural and *a priori* formulation of the dimensionless equation of potential flow, instead of relying on the questionable iterative method to define length and time scales.
2. The effect of the surface tension is included in the model.
3. The use of a realistic boundary condition at the point where the bubble surface

meets the orifice plate allows us to relate the bubble shape to the dynamic three-phase (i.e. gas-liquid-solid) contact angle, instead of the arbitrary shape criterion.

7.1.2 Conclusions on bubble formation with wall effect

This research attempted to assess the wall effect on bubble formation both experimentally and theoretically.

In the experiment, three different bubbling regimes were observed and analyzed by means of high-speed video camera and dynamic pressure transducer. The effects of the chamber volume, gas flow rate and orifice diameter were also studied.

The following summarizes the conclusions obtained from the experimental results:

1. There are three bubbling regimes, single bubbling, pairing and multiple bubbling, for bubble formation which are affected by the column diameter.
2. With the decrease of the diameter ratio or increase of the gas flow rate, the bubbling regimes generally transition from single bubbling to pairing and multiple bubbling, with a corresponding decrease in bubbling frequency.
3. Pairing and multiple bubbling are more likely to occur with large chamber volume and gas flow rate. For the larger chamber volume, the boundaries between adjacent regimes are shifted upwards significantly.
4. Orifice diameter has an effect on bubble formation. With an increase of the orifice diameter, the bubble volume is increased with a corresponding decrease in bubbling frequency.

To investigate the wall effect theoretically, a model was developed using the boundary integral method with the introduction of a specific system of images. Comparison of experimental results for bubbling frequency with the theoretical predictions shows that the agreement is very good, i.e. the model successfully predicts the effect of the column wall on bubbling frequency.

In addition, to take into consideration the interaction between the column wall and the growing bubble at the orifice, as well as the interaction between subsequent bubbles formed and detached from the orifice, a theoretical spherical model for bubble formation was developed using potential flow theory. Our investigation demonstrates that the bubble-wall and bubble-bubble interactions can have profound influence on bubbling frequencies and bubbling regimes in bubble formation at a submerged orifice. These effects have been successfully modelled by potential flow and bubble wake pressure analysis, and the occurrence of the bubbling regime can be predicted with the spherical model. Simulated results using the theoretical model agreed very well with experimental data.

7.1.3 Contributions

The contributions of this research are summarized as follows:

1. The boundary integral method model initially developed by Hooper (1986) was improved significantly.
2. The wall effect on bubbling frequency and bubbling regime was investigated extensively.
3. For the non-spherical modeling, the boundary integral method and system of images were used to predict the bubbling frequency. The spherical model developed by Zhang and Tan (2000) was developed with the consideration of wall

effect on bubble formation, and the bubbling frequency and bubbling regime can be predicted with this improved model.

7.2 Recommendations for further study

In this section, recommendations for further study are given as follows:

1. In the problems discussed so far, the gas is not soluble in liquid or it does not react with the liquid. However, bubble formation with chemical reaction has many applications in physical and chemical processes and it is such a case that we should address, especially in the environmental field in which pollution is a serious problem. Thus, it is essential to study bubble formation with mass transfer and chemical reaction both experimentally and theoretically. Several workers have studied mass transfer from the surface of a growing bubble at a gas distribution. Burman and Jameson (1976) proposed mass transfer equations during bubble formation. Stangle and Mahaling (1989) developed a spherical model to estimate the gas absorption rate during bubble formation. Terasaka et al. (1999) conducted experiments to measure the absorption rate from pure SO_2 gas bubbles to water. A pseudo-spherical model for the SO_2-water system was proposed. In their model, mass transfer from the gas-liquid interface during bubble growth was described by the penetration theory. They applied spherical equations of motion and spherical gas stream function to describe the bubble growth. Therefore, further study of bubble formation should be extended to these cases.
2. What has been discussed so far is the mechanics of bubble formation under single orifice. However, bubble formation with multiple orifices is widely used and encountered in practice. Xie and Tan (2003) investigated the bubble formation at

multiple orifice and regimes of synchronous, alternative and unsteady bubbling were clearly identified in their work. A theoretical model for predicting synchronous bubbling frequency was also developed in Xie and Tan (2003). Therefore, extending the present model to describe the process of multiple-orifice bubble formation is recommended for future research.

3. Liquid viscosity is one of the factors affecting bubble formation. Zhang and Tan (2005) developed a model for the prediction of bubble formation in viscous liquid. In Zhang and Tan (2005), the interfacial element method was applied to calculate to bubble shape and detachment, and drag force due to the viscous drag was incorporated in force balance to take into account of the viscosity effect. To investigate the bubble formation more thoroughly, further experimental and theoretical study of bubble formation should been carried out with the consideration of the effect of the liquid viscosity.

REFERENCES

Abramowitz, M. and I.A. Stegun. Handbook of mathematical functions. Dover Publications, New York. 1965.

Al-Hayes, R.A.M. and R.H.S. Winterton. Bubble growth in flowing liquids, Int. J. Heat Mass Transfer, 24, pp.213-221, 1981.

Bhaga, D. and M.E. Weber. Bubbles in viscous liquids: shape, wakes and velocities. J. Fluid Mech. 105, pp61-85. 1981.

Burman, J.E. and G.J. Jameson. Diffusional mass transfer to a growing bubble. Chem. Eng. Sci. 31(5), pp. 401-403. 1976.

Blake, J.R., B.B. Taib and G. Doherty. Transient cavities near boundaries. Part I. Rigid boundary. J. Fluid Mech. 170, 479-497. 1986.

Blake, J.R., B.B. Taib and G. Doherty. Transient cavities near boundaries. Part II. Free surface. J. Fluid Mech. 181,197-212. 1987.

Bonnet, M. Boundary integral equation methods for solids and fluids. Editions Eyrolles and CNRS Editions, Paris, France, 1995.

Brebbia, C.A. The boundary element method for engineers, Pentech Press, London. 1978.

Chen, R.C., F.M. Wang and T.J. Lin. Bubble wake dynamics of a single bubble rising in the freeboard of a two-dimensional liquid-solid fluidized bed. Chem. Eng. Sci. 54, pp.4831-4838. 1999.

Chen, W.B. and R.B.H. Tan. Theoretical analysis of bubble formation in a co-flowing liquid. J. Chem. Eng. Jpn. 35(10), pp. 952-962. 2002.

Clift, R., J.R. Grace and M.E. Weber. Bubbles, drops, and particles. Academic Press, New York. 1978.

Colella, D., D. Vinci, R. Bagatin, M. Masi and E.A. Bakr. A study on coalescence and breakage mechanisms in three different bubble columns. Chem. Eng. Sci. 54, pp. 4767-4777. 1999.

Collins, R. A second approximation for the velocity of a large gas bubble rising in an infinite liquid. J. Fluid Mech. 25, pp.469-480. 1966.

Collins, R. The effect of a containing cylindrical boundary on the velocity of a large gas bubble in a liquid. J. Fluid Mech. 28, pp.97-112. 1967.

Coutanceau, M. and P. Thizon. Wall effect on the bubble behaviour in highly viscous liquids. J. Fluid Mech. 107, pp.339-373. 1981.

Davidson, J.F. and B.O.G. Schüler. Bubble formation at an orifice in a viscous liquid. Trans. Instn. Chem. Engrs. 38, pp. 144-154. 1960a.

Davidson, J.F. and B.O.G. Schüler. Bubble formation at an orifice in an inviscid liquid. Trans. Instn. Chem. Engrs. 38, pp. 335-352. 1960b.

Davidson, L. and E.H. Amick. Formation of gas bubbles at horizontal orifices. AICHE Journal 2(3), pp.337-242, 1956.

Davies, R.M. and G.I. Taylor. The mechanics of large bubbles rising through extended liquids and through liquids in tubes. Proc. Roy. Soc. London. A200, 375-390, 1950.

Fan, L.S. and K. Tsuchiya. Bubble wake dynamics in liquids and liquid solid suspensions. Butterworth-Heinemann, Boston. 1990.

Fawkner, R.D., P.P. Kluth and J.S. Dennis. Bubble formation at orifices in pulsed, flowing liquids. Trans. Instn. Chem. Engrs. 68, pp. 69-73. 1990.

Fountain, C.R. The measurement and analysis of gas discharge in metallurgical converters. Ph.D thesis, University of Melbourne. 1988.

Gray, A. Modern Differential Geometry of Curves and Surfaces. Boca Raton, FL: CRC Press. 1998.

Harmathy, T.Z. Velocity of large drops and bubbles in media of infinite or restrict extend. AICHE J. 6, 281. 1960.

Hayes, W.B., B.W. Hardy and C.D. Holland. Formation of gas bubbles at submerged orifices. AICHE J. 5, 319-324. 1959.

Hess, J.L. and A.M.O. Smith. Calculation of potential flow about arbitrary bodies. In Progress in aeronautical science, Ed. By Kuchemann, D. Pergamon, London. 1966.

Hess, J.L. Improved solution for potential flow about arbitrary axisymmetric bodies by the use of higher-order surface source method, Computer Methods Appl. Mech Engng., 5, pp.297-308.1975.

Hooper, A. P. A study of bubble formation at a submerged orifice using the boundary element method. Chem. Eng. Sci. 41, pp.1879-1890. 1986.

Hughes, R.R., A.E. Handlos, H.D. Evans and R.L. Maycock. Formation of bubbles at simple orifices. Chem. Eng. Prog. 51, pp.557-563. 1955.

Iliadis, P., V. Douptsoglou and M. Stamatoudis. Effect of orifice submergence on bubble formation, Chem. Eng. Technol. 23, pp.341-345. 2000.

Jameson, G.J. and A. Kupferberg. Pressure behind a bubble accelerating from rest: single theory and applications. Chem. Eng. Sci. 22, pp.1053-1055. 1967.

Jaswon, M.A. and G.T. Symm. Integral equation methods in potential theory and elastostatics, Academic Press, London. 1977.

Khurana, A.K. and R. Kumar. Studies in bubble formation iii: Chem. Eng. Sci. 24, pp. 1711-1723. 1969.

Kim, I., Y. Kamotani and S. Ostrach. Modeling bubble and drop formation in flowing liquids in microgravity. AIChE J. 40(1), pp. 19-28. 1994.

Krishna, R., M.I. Urseanu, J.M. van Baten and J. Ellenberger. Rise velocity of a swarm of large gas bubbles in liquids. Chem. Eng. Sci. 54, pp.171-183. 1999.

Kumar, R. and N.R. Kuloor. The formation of bubbles and drops. In Advances in Chemical Engineering. 8, Academic Press, New York, pp. 256-368. 1970.

Kupferberg, A. and G. J. Jameson. Bubble formation at a submerged orifice above a gas chamber of finite volume. Trans. Inst. Chem. Engrs 47, pp.241-250. 1969.

Lamb, H. Hydrodynamics. 6th ed., Cambridge University Press. 1945.

LaNauze, R.D. and I.J. Harris. On a model for the formation of gas bubbles at a single submerged orifice under constant pressure conditions. Chem. Eng. Sci. 27, pp. 2102-2105. 1972.

LaNauze, R.D. and I.J. Harris. Gas bubbles formation at elevated system pressures. Trans. Instn. Chem. Engrs. 52, pp. 337-348. 1974.

Lazarek, G.M. and H. Littman. The pressure field due to a large circular capped air bubble rising in water. J. Fluid Mech. 66, pp.673-687. 1974.

Li, H.Z., Y. Mouline and N. Midoux. Modelling the bubble formation dynamics in non-Newtonian fluids. Chem. Eng. Sci. 57(3), pp. 339-346. 2002.

Li, Y., J. Zhang and L.S. Fan. Numerical simulation of gas-liquid-solid fluidization systems using a combined CFD-VOF-DPM method: bubble wake behavior. Chem. Eng. Sci. 54, pp.5101-5107. 1999.

Liow, J. and N.B. Gray. A model of bubble growth in wetting and non-wetting liquids. Chem. Eng. Sci. 43(12), pp.3129-3139. 1988.

Marmur, A. and E. Rubin. A theoretical model for bubble formation at an orifice submerged in an inviscid liquid, Chem. Eng. Sci. Vol. 31, pp.453-463. 1976

Marshall, S.H., M.W. Chudacek and D.F. Bagster. A model for bubble formation from an orifice with liquid cross-flow. Chem. Eng. Sci. 48, pp.2049-2059. 1993.

McCann, D.J. and R.G.H. Prince. Bubble formation and weeping at a submerged orifice. Chem. Eng. Sci. 24, pp. 801-814. 1969.

McCann, D.J. and R.G.H. Prince. Regimes of bubbling at a submerged orifice. Chem. Eng. Sci. 26, pp. 1505-1512. 1971.

McNallan, M. J. and T. B. King. Fluid dynamics of vertical submerged gas jets in liquid metal processing system, Metallurgical Transactions B 13B, pp.165-173. 1982.

Milne-Thomson, L.M. Theoretical hydrodynamics. 5th ed., Macmillan, London. 1968.

Mittoni, L.J. Deterministic Chaos in Metallurgical Gas-Liquid Injection Processes. Ph.D thesis, The University of Melbourne, 1997.

Miyahara, T., Y. Matsuba and T. Takahashi. The size of bubbles generated from perforated plants. International Chemical Engineering, 23(3), pp.517-602. 1983.

Miyahara, T. and T. Takahashi. Bubble volume in single bubbling regime with weeping at a submerged orifice, J. Chem. Engng. Jpn, 17(6), pp.597-601. 1984.

Nilmani, M. Prediction of pressure behind a rising bubble accelerating from rest. Can. J. Chem. Eng. 60, pp.692-694. 1982.

Park, Y., A.L. Tyler and N. de Nevers. The chamber orifice interaction in the formation of bubbles. Chem. Eng. Sci. 32, pp.907-916. 1977.

Pinczewski, W. V. The formation and growth of bubbles at a submerged orifice. Chem. Eng. Sci. 36, pp.405-411. 1981.

Power, H. BE Applications in Fluid Mechanics, Computational Mechanics Publications, Southampton Boston. 1995.

Ramakrishnan, S., R. Kumar and N.R. Kuloor. Studies in bubble formation-I bubble formation under constant flow conditions. Chem. Eng. Sci. 24, pp. 731-748. 1969.

Ruff, K. Formation of gas bubbles at nozzles with constant throughput. Chem. Ing. Techn. 44, pp. 1360-1366. 1972.

Ruzicka, M.C., J. Drahoš, M. Fialová and N.H. Thomas. Effect of bubble column dimensions on flow regime transition. Chem. Eng. Sci. 56, pp.6117-6124. 2001.

Sada, E., A. Yasunishi, S. Katoh and M. Nishioka. Bubble formation in flowing liquid. Can. J. Chem. Eng. 56, pp. 669-672. 1978.

Sadhal, S.S., P.S. Ayyaswamy and J.N. Chung. Transport phenomena with drops and bubbles. pp. 311-403, Springer, New York. 1997.

Satyanarayan, A., R. Kumar and N.R. Kuloor. Studies in bubble formation-II bubble formation under constant pressure conditions. Chem. Eng. Sci. 24, pp. 749-761. 1969.

Snabre, P. and F. Magnifotcham. Formation and rise of a bubble stream in a viscous liquid. Eur. Phys. J. B 4, pp. 369-377. 1998.

Stangle, G.C. and R. Mahaling. Mass transfer with chemical reaction during gas bubble formation in foam column reactors. Chem. Eng. Sci. 44(3), pp. 507-514. 1989.

Stroud, A. H. and D. Secrest. Gaussian quadrature formulas. Prentice-Hall, Englewood Cliffs, NJ. 1966.

Swope, R.D. Single bubble formation at orifices submerged in viscous liquids. Can. J. Chem. Eng. 49, pp. 169-174. 1971.

Tadaki, T. and S. Maeda. Bubble formation at submerged orifices, Kag. Kog. Ron. (Chemical Engineering Japan), 27, pp.147-155. 1963.

Takahashi, T. and T. Miyahara. Bubble volume formed at submerged nozzles: constant flow condition. Kagaku Kogaku Ronbunshu. 2, pp. 138-143. 1976.

Takahashi, T. and T. Miyahara. Bubble volume formed at submerged orifice: chamber orifice interaction. Kagaku Kogaku Ronbunshu. 5, pp. 453-456. 1979.

Takahashi, T., T. Miyahara, S. Senzai and H. Terakado. Bubble formation at submerged nozzle in cocurrent, countercurrent and crosscurrent flow. Kagaku Kogaku Ronbunshu. 6 (6), pp. 563-569. 1980.

Tan, R.B.H. and I.J. Harris. A model for non-spherical bubble growth at a single orifice, Chem. Eng. Sci. 41(12), pp.3175-3128. 1986.

Tan, R.B.H., W.B. Chen and K.H. Tan. Non-spherical model for bubble formation with liquid cross-flow. Chem. Eng. Sci. 55, pp.6259-6267. 2000.

Terasaka, K. and H. Tsuge. Bubble formation at a single orifice in highly viscous liquids. J. Chem. Eng. Jpn. 23, pp. 160-165. 1990.

Terasaka, K., Y. Hieda and H. Tsuge. SO_2 bubble formation at an orifice submerged in water. J. Chem. Eng. Jpn. 32(4), pp. 472-479. 1999.

Tsuchiya, K., K. Ohsaki and K. Taguchi. Large and small bubble interaction patterns in a bubble column. Int. J. Multiphase Flow 22, pp.121-132. 1996.

Tsuge, H. and S. Hibino. Bubble formation from a submerged single orifice accompanied by pressure fluctuations in gas chamber. J. Chem. Eng. Jpn. 11, pp.173-178. 1978.

Tsuge, H., S. Hibino and U. Nojima. Volume of a bubble formed at a single submerged orifice in a flowing liquid. Int. Chem. Eng. 21(4), pp. 630-636. 1981.

Tsuge, H. and S. Hibino. Bubble formation from an orifice submerged in liquids. Chem. Eng. Comm. 22, pp. 63-79. 1983.

Tsuge, H. Encyclopedia of fluid mechanics. Vol.3, pp. 192-232. Gulf Publishing Co. 1986.

Tsuge, H., Y. Nakajima and K. Terasaka. Behavior of bubbles formed from a submerged orifice under high system pressure. Chem. Eng. Sci. 47, pp.3272-3280. 1992.

Van Krevelen, D.W. and P.J. Hoftijzer. Studies of gas-bubble formation: calculation of interfacial area in bubble contactors. Chem. Eng. Prog. 46(1), pp. 29-35. 1950

Wace, P.F., M.S. Morrell and J. Woodrow. Bubble formation in a transverse horizontal liquid flow. Chem. Eng. Commu. 62, pp. 93-106. 1987.

Walters, J.K. and J.F. Davidson. The initial motion of a gas bubble formed in an inviscid liquid part 1: The two-dimensional bubble. J. Fluid Mech. 12, pp.408-416. 1962.

Walters, J.K. and J.F. Davidson. The initial motion of a gas bubble formed in an inviscid liquid part 2: The three-dimensional bubble and the toroidal bubble. J. Fluid Mech. 17, pp.321-336. 1963.

Wilkinson, P.M. and L.L. Van Dierendonck. Pressure and gas density effects on bubble break-up and gas hold-up in bubble columns. Chem. Eng. Sci. 45, pp.2309-2315. 1990.

Wilkinson, P.M. and L.L. Van Dierendonck. A theoretical model for the influence of gas properties and pressure on single-bubble formation at an orifice. Chem. Eng. Sci. 49(9), pp.1429-1438. 1994.

Wraith, A.E. Two-stage bubble growth at a submerged plate orifice. Chem. Eng. Sci. 26, pp. 1659-1671. 1971.

Wraith, A.E. and T. Kakutani. The pressure beneath a growing rising bubble. Chem. Eng. Sci. 29, pp.1-12. 1974.

Xie, S. and R.B.H. Tan. Bubble formation at multiple orifices-bubbling synchronicity and frequency. Chem. Eng. Sci. 58, pp.4639-4647. 2003.

Zhang, W. and R.B.H. Tan. A model for bubble formation and weeping at a submerged orifice. Chem. Eng. Sci. 55, pp.6243-6250. 2000.

Zhang, W. and R.B.H. Tan. A model for bubble formation and weeping at a submerged orifice with liquid cross-flow. Chem. Eng. Sci. 58, pp.287-295. 2003.

Zhang, Y., Z. Xiao and R.B.H. Tan. Interfacial Element Modeling of Bubble Formation with Liquid Viscosity. J. Chem. Engng. Jpn. Accepted. 2005.

Zughbi, H.D., W. V. Pinczewski and C.J. Fell. Bubble growth by the Marker and Cell technique. 8th Aust. Fluid Mech. Conf., 8B.9-8B.12. 1983.

APPENDIX A Integral evaluation

A.1 Standard Gaussian Legendre Quadrature

The approximate value of an integral over the line segment $[-1,+1]$ is given by the formula:

$$\int_{-1}^{1} f(t)dt = \sum_{i=1}^{n} w_i f(t_i) \tag{A.1}$$

where t_i is a designated evaluation point, w_i is the weight of that point in the sum and n is the number of the points at which the function $f(t)$ is evaluated. The values of t_i and w_i are uniquely determined for any given value of n and are tabulated in the literature. When n is chosen as 8, the values of t_i and w_i are listed in the Table A.1.

Table A.1 Evaluation points and corresponding weight for standard integral

t_i	w_i
-0.96028986	0.10122854
-0.79666648	0.22238103
-0.52553241	0.31370665
-0.18343464	0.36268378
0.18343464	0.36268378
0.52553241	0.31370665
0.79666648	0.22238103
0.96028986	0.10122854

In most cases we will want to evaluate the integral on a more general interval, say $[a,b]$. We will use the variable x on this more general interval, and linearly map the $[a,b]$ interval for x onto the $[-1,+1]$ interval for t using the linear transformation:

$$x = c + mt \quad \text{where} \quad c = \frac{1}{2}(b+a) \quad \text{and} \quad m = \frac{1}{2}(b-a)$$

Finally, we can write the Gaussian Legendre estimate of the integral as:

$$\int_a^b f(x)dx = m\sum_{i=1}^{n} w_i f(c + mt_i) \tag{A.2}$$

A.2 Integral with singularity of log type

For an integral containing an explicit singularity of log type over interval $[0,1]$, the evaluation can be obtained as follows:

$$\int_0^1 f(t)\ln(\frac{1}{t})dt = \sum_{i=1}^{n} w_i f(t_i) \tag{A.3}$$

where t_i is a designated evaluation point, w_i is the weight of that point in the sum and n is the number of the points at which the function $f(t)$ is evaluated. The values of t_i and w_i are uniquely determined for any given value of n and are tabulated in the literature. When n is chosen as 8, the values of t_i and w_i are listed in the Table A.2.

Table A.2 Evaluation points and corresponding weight for integral with singularity

t_i	w_i
0.01332024	0.16441660
0.07975043	0.23752561
0.19787103	0.22684198
0.35415399	0.17575408
0.52945858	0.11292403
0.70181453	0.05787221
0.84937932	0.02097907
0.95332645	0.00368641

APPENDIX B Correction of gas volumetric flow rate

The flow meters used had the scale readings calibrated by the manufacturer for a standard condition of air density 1.293 kg/m^3, temperature of 20 ^oC and pressure of 1 atm (absolute). The formula given below for volumetric flow rate correction for different densities, temperature and pressure is:

$$Q = Q^{'} \times \left[\frac{1.293}{\rho_G}\right]^{1/2} \times \left[\frac{293}{273+T}\right]^{1/2} \times \left[\frac{1.013+P}{1.013}\right]^{1/2} \quad \text{(B.1)}$$

where, Q: corrected volumetric gas flow rates (l/min);

$Q^{'}$: actual reading of volumetric gas flow rates (l/min);

ρ_G: gas density tested , pure air: 1.293 kg/m^3;

T: gas temperature, 20 ^oC;

P: gauge pressure in the flow meter;

The unit for volumetric gas flow rates in this project was based on standard conditions. For example, for gas flow reading 2 l/min at inlet pressure 2 bar, the corrected flow rate is:

$$Q = 2 \times \left[\frac{1.293}{1.293}\right]^{1/2} \times \left[\frac{293}{273+20}\right]^{1/2} \times \left[\frac{1.013+2}{1.013}\right]^{1/2} = 3.45 l/\min \quad \text{(B.2)}$$

APPENDIX C List of publications

Xiao, Z.Y. and R.B.H. Tan. An improved model for bubble formation using the boundary integral method. Chem. Eng. Sci. 60(1), pp.179-186. 2005.

Xiao, Z.Y. and R.B.H. Tan. Wall effect on bubble formation at a submerged orifice. In 16th International Conference of Chemical and Process Engineering, 22-26 August, 2004, Praha, Czech Republic.

Xiao, Z.Y. and R.B.H. Tan. A model for bubble-bubble and bubble-wall interaction in bubble formation. AICHE J. Accepted, 2004.

Xiao, Z.Y. and R.B.H. Tan. A model for the wall effect on bubble formation at a submerged orifice. In 7th Conference on Gas-Liquid and Gas-Liquid-Solid Reactor Engineering, 21-24 August, 2005, Strasbourg, France.

Zhang, Y.L., Z.Y. Xiao and R.B.H. Tan. Interfacial Element Modeling of Bubble Formation with Liquid Viscosity. J. Chem. Engng. Jpn. Accepted, 2005.